TECHNISCHE
UNIVERSITÄT
WIEN
Vienna University of Technology

Application Oriented
Coating Development

DISSERTATION

Architecturally-designed Al-Cr-based nitride/oxide and oxynitride coatings for high temperatures applications

carried out for the purpose of obtaining the degree of Dr. techn,

submitted at TU Wien,

Faculty of Mechanical and Industrial Engineering,

by

Dipl.-Ing. Robert Raab

under the supervision of

Univ.Prof. Dipl.-Ing. Dr.mont. Paul Heinz Mayrhofer

Institute of Materials Science and Technology, E308

Vienna, June 2017

TU Bibliothek
Your knowledge hub
WIEN

Affidavit:

I declare in lieu of oath, that I wrote this thesis and performed the associated research myself, using only literature cited in this volume.

_____   _____

Date   Signature

Acknowledgements

I would like to express my sincerest gratitude to **Paul** for giving me not only the chance in life to proof myself and "the world" that I am worthy and capable of achieving such high academic honour, but also for the opportunity to work side by side with such a brilliant scientist, mentor, and good person. I cannot thank you enough for your sympathy and support so that I could find the balance between the scientist and the husband and father in me.

I would like to especially thank **Christian Martin Koller** for his guidance, help, invested time, scientific expertise and constant support during preparation and writing of the papers and this thesis.

I also want to highlight the management skills of **Helmut Riedl** aka "**Herr Direktor**" and his support in creating promising deposition processes.

Further on, I would like to thank **Stefan Glatz** aka "**Glatzi**", who not only helped me with any kind of computational trouble shooting, but also showed me the importance to always carry a multi-tool within your pants.

However, the whole Thin Film Group is acknowledged and special thanks to **Alex, Bernhard, Elias, Fedor, Matthias, Nicola, Phillip, Rainer, Valentin, Vincent,** and **Wolfgang** for their friendship and support in many difficult ways.

Appreciation is also extended to the members of the Institute of Materials Science and Technology and especially the three ladies in the secretariat who gave me the feeling of belonging from the start.

I want to thank my **family** and especially my **parents**, for their support and assurance along this intensive and challenging journey of my life.

Further on, I also want to thank the "**Saunarunde**" and the "**Uni**-**Buben**" for their support and patience in times when family and work had to come first.

Finally, **Johanna**, my love, my wife, you have witnessed the ups and downs of my work and health side by side me. I can hardly express my feelings within a few lines. Not only have you given birth to our three adorable kids within this three years and managed their needs, you also have put your own needs back so that I could focus on my studies and we could reach our goals in time. You are always there for us. We rely on your strength, endurance, patience and your incredible strong immune system. You are truly my rock in the surf, my hero, my Wonder Woman.

"In brightest day, in blackest night, no evil shall escape my sight. Let those who worship evil's might, beware my power — Green Lantern's light!"
(Oath of the Green Lantern Corp, DC Comics)

"Learn from yesterday, live for today, hope for tomorrow. The important thing is not to stop questioning."
(Albert Einstein)

"God made the bulk; the surface was invented by the devil."
(Wolfgang Pauli)

Table of Contents

Abstract

$Al_xCr_{1-x}N$ and $(Al_xCr_{1-x})_2O_3$ hard coatings deposited by physical vapour deposition techniques (i.e. cathodic arc evaporation or sputtering) are commonly used in industrial machining applications such as milling, drilling, turning, and cutting, to increase the performance and lifetime of tools and components by reducing endurance, maintenance, and thus costs in general. Therefore, such Al-Cr-based protective hard coatings exhibit high hardness, high thermal stability, high wear and oxidation resistance which make them suitable for a multitude of applications, which not only require a balanced and tailored property spectrum up to 1000 °C (and beyond), but also the capability to withstand oxidising and chemically invasive environments. It is well known, that deposition parameters such as temperature, bias voltage, (reactive) gas mixture, and partial pressure as well as the cathode/target material itself highly influences the coatings structure and morphology and thus the coating properties. However, a convenient method to improve their properties of particular interest is the formation of architecturally designed coatings (e.g. multilayer or even superlattice arrangements and graded compositions).

Therefore, the impact of coating architecture and interfaces on mechanical properties of arc evaporated $Al_xCr_{1-x}N/(Al_xCr_{1-x})_2O_3$ multilayers has been investigated. Three different interface geometries – blurred, hybrid, and distinct – were designed by adjusting the reactive gas configuration between the individual $Al_xCr_{1-x}N$ and $(Al_xCr_{1-x})_2O_3$ layers. Variations in the overall interface volume (architecture) were realised by varying the deposition time per layer, resulting in 12, 25, and 50 bilayers with (bilayer) thicknesses between 30 and 175 nm.

All multilayers were synthesised in a single-phase cubic structure with lattice parameters in between monolithically grown AlCrN and AlCrO. Thereby, for the three larger bilayer periods, XRD peaks indicative for oxygen and nitrogen-rich layers can be separated, whereas a gradual convergence and grain refinement is observed when decreasing the individual layer thickness. The most favourable mechanical properties were obtained for the distinct interface geometry (H of ~19 GPa) followed by hybrid (16 GPa) or blurred (14 GPa) multilayers. By decreasing the bilayer period and hence increasing the overall interface volume these differences gradually diminish and the behaviour of distinct, hybrid, and blurred interface architectures equalize, leading to maximum H values of around 22.5 GPa.

Furthermore, cathodic arc evaporated homogenously grown $(Al_xCr_{1-x})_2O_3$ as well as $Al_xCr_{1-x}N/(Al_xCr_{1-x})_2O_3$ multilayer coatings were synthesised using powder metallurgically prepared $Al_{0.7}Cr_{0.3}$ targets. These coatings were studied in detail for their thermal stability, as well as their phase evolution during annealing. A combination of differential scanning calorimetry, thermal gravimetric analysis, X-ray powder diffraction, and

hardness investigations after annealing the samples up to 1500 °C in vacuum for one hour were used. The powder annealed $(Al_xCr_{1-x})_2O_3$ demonstrate a phase transformation of the face centred cubic $(Al,Cr)_2O_3$ phase into the corundum-type $(Al,Cr)_2O_3$ solid solution at ~1050 °C. The corundum-type $(Al,Cr)_2O_3$ solid solution deposited on Al_2O_3 substrates dissociates to α-Al_2O_3 and transient chromium oxides after annealing at elevated temperatures for 1 h. Investigations on powder as well as Al_2O_3 substrates, indicate the formation and evaporation of transient chromium-oxides also for $Al_xCr_{1-x}N/(Al_xCr_{1-x})_2O_3$ multilayer coatings. DSC/TGA results point out that in the case of the multilayers, the thermal stability increases, with higher number of bilayers, regardless of their interface types (distinct and blurred). The decomposition of CrN into h-Cr_2N and further to c-Cr, via N_2 release, can be therefore retarded up to ~1200 °C.

However, a cathodic arc evaporated monolithically grown gradient-layer—with a continuous transition from $(Al,Cr)N$ to $(Al,Cr)_2O_3$ and back to $(Al,Cr)N$—was synthesised using powder metallurgically prepared $Al_{0.7}Cr_{0.3}$ targets. The transition zone from nitride to oxide was investigated in detail by TEM-SAED and STEM-EDS, to understand the structural and chemical evolution taking place through continuous transitions or blurred interfaces between individual $(Al,Cr)N$ and $(Al,Cr)_2O_3$ layers. This information was used to deposit the $(Al_xCr_{1-x})(O_{1-y}N_y)$ films with specifically tailored structural and chemical properties and studied in detail for their thermal stability. DSC/TGA results again point out that in the case of $(Al,Cr)(O,N)$, the thermal stability increases, with increasing O fraction. The decomposition of CrN into h-Cr_2N and subsequently to c-Cr, via N_2 release, can be successfully retarded from ~1090 to 1150 °C and thus 50 °C lower than the before mentioned multilayer arrangement of individual $(Al,Cr)N$ and $(Al,Cr)_2O_3$ layers.

At last, monolithically grown as well as multi-layered $(Al_xCr_{1-x})(O_{1-y}N_y)$ coatings were synthesised with different synthetic air flow rates by reactive arc evaporation using powder metallurgical prepared $Al_{0.7}Cr_{0.3}$ targets. Increasing the synthetic air flow rate from 200 to 1100 sccm (absolute) or 50 to 275 sccm (per active source, p.a.s.), results in higher oxygen fraction for the monolithically grown films and thus in a transition from a dense $(Al,Cr)N$-like coating with single phase fcc structure, to a columnar structured $(Al,Cr)_2O_3$-like film with cubic and hexagonal phases, higher defect as well as droplet density. Therefore, the hardness of these coatings decreases from ~33 to 15 GPa with increasing oxygen fraction, while the multilayers exhibit hardness values of ~26 GPa. The latter show single phase fcc structures. The thermal stability of $(Al,Cr)(O,N)$ coatings synthesised with synthetic air increases with increasing O fraction. The onset temperature for the decomposition of fcc-CrN into h-Cr_2N and further to bcc-Cr, via N_2 release, as well as the transition from metastable fcc-$(Al,Cr)_2O_3$ to α-$(Al,Cr)_2O_3$ can be retarded up to 1200–1300 °C for annealing in He or synthetic air atmosphere, respectively.

Zusammenfassung

Aluminium-Chrom basierende Hartstoffbeschichtungen, die durch physikalische Dampfphasenabscheidungstechniken (z.B.: kathodische Lichtbogenverdampfung oder Sputtern) abgeschieden werden, werden üblicherweise in industriellen Bearbeitungsanwendungen wie Fräsen, Bohren, Drehen und Schneiden (allgemein Zerspanung) verwendet, um die Leistung und Lebensdauer der eingesetzten Werkzeuge zu erhöhen. Daher weisen derartige Hartstoffschutzschichten eine hohe Härte, eine hohe thermische Stabilität, eine hohe Verschleiß und Oxidationsbeständigkeit auf, welche sie auch bei oxidierenden sowie chemisch invasiven Umgebungen vielseitig einsetzbar machen und Einsatztemperaturen von 1000 °C (und darüber hinaus) erlauben. Es ist bekannt, dass Beschichtungsparameter wie Temperatur, Vorspannung (elektrische Potentialdifferenz zwischen Quelle (Target) und Substrat), (reaktives) Gasgemisch und Partialdruck sowie das Quellen-Material selbst, die Beschichtungsstruktur und die Morphologie und damit die Beschichtungseigenschaften stark beeinflussen. Eine geeignete Methode ist der Einsatz speziell entworfener Beschichtungs-Geometrien (z. B. mehrschichtige oder sogar Übergitteranordnungen und abgestufte Zusammensetzungen).

Aus diesem Grunde wurde der Einfluss der Beschichtungsarchitektur und der Grenzflächen (Übergänge) von mehrlagigen lichtbogenverdampften $Al_xCr_{1-x}N/(Al_xCr_{1-x})_2O_3$ Schichten auf die mechanischen Eigenschaften untersucht. Drei verschiedene Grenzflächen-Geometrien (Übergangstypen) - verschwommen, hybrid und deutlich - wurden durch Einstellen der reaktiven Gaskonfiguration zwischen den einzelnen $Al_xCr_{1-x}N$ und $(Al_xCr_{1-x})_2O_3$ Lagen entworfen. Die Dicke der einzelnen Lagen und damit die gesamt Anzahl der Lagen innerhalb der Schicht wurden durch unterschiedliche Abscheidungszeiten (pro Lage) realisiert. Dies führte zu Schichten mit insgesamt 24, 50 und 100 Lagen, wobei die Dicken der einzelnen Lagen jeweils ca. 80, 40 und 20 nm betrugen.

Alle Multilagenschichten wurden in einer einphasigen kubischen Struktur mit Gitterparametern zwischen monolithisch gewachsenem AlCrN und AlCrO synthetisiert. Separierte Nitrid- und Oxid-Lagen können mittels Röntgendiffraktometrie nur bei den Schichten mit der größten individuellen Lagendicke aufgelöst werden, während eine allmähliche Konvergenz- und Kornverfeinerung beobachtet wird, sobald die individuelle Lagendicke verringert wird. Der Einfluss der unterschiedlichen Grenzflächen-Geometrien (Übergangstypen) auf die mechanischen Eigenschaften ist am deutlichsten am Beispiel der 24-Lagen-Schichten zu erkennen. Während man bei dieser Schichtarchitektur mittels verschwommenem Übergang (von Nitrid zu Oxid und umgekehrt) bloß eine Härte von ~14 GPa erreicht, weist ein deutlicher (relativ scharfer) Übergang der einzelnen Lagen eine höhere Härte von ~19 GPa auf. Durch die

Verringerung der Lagendicke und damit die Erhöhung der Gesamtlagenzahl verringern sich diese Unterschiede allmählich und die Schichten erreichen unabhängig vom Übergangstyp, Härtewerte von etwa 22 GPa.

Darüber hinaus wurden mittels kathodischen Lichtbogenverdampfens monolithische $(Al_xCr_{1-x})_2O_3$ sowie $Al_xCr_{1-x}N/(Al_xCr_{1-x})_2O_3$ Multilagenschichten unter Verwendung von pulvermetallurgisch hergestellten $Al_{0.7}Cr_{0.3}$-Targets/Kathoden (Quellen) synthetisiert. Diese Beschichtungen wurden detailliert auf ihre thermische Stabilität sowie ihre Phasenentwicklung während des Glühens untersucht. Eine Kombination aus Differentialkalorimetrie (DSC), Thermogravimetrie (TGA), Röntgen-Pulverdiffraktion und Härteuntersuchungen nach dem Glühen der Proben bis zu 1500 ° C in Vakuum für eine Stunde wurden verwendet. Das geglühte $(Al_xCr_{1-x})_2O_3$ Pulver zeigt eine Phasenumwandlung der flächenzentrierten kubischen $(Al_xCr_{1-x})_2O_3$-Phase in die Korund-Typ $(Al_xCr_{1-x})_2O_3$-Phase bei ~1050 ° C. Die auf Al_2O_3-Substraten abgeschiedene Korund-Typ-$(Al_xCr_{1-x})_2O_3$ Mischkristalle dissoziieren bei der 1-h-Glühung bei erhöhter Temperatur zu α-Al_2O_3 und flüchtigen Chromoxiden. Untersuchungen an Pulver- sowie Schichten auf Al_2O_3-Substraten zeigen die Bildung und Verdampfung von flüchtigen Chromoxiden auch für $Al_xCr_{1-x}N/(Al_xCr_{1-x})_2O_3$ Multilagenschichten. DSC/TGA-Ergebnisse weisen darauf hin, dass im Falle der Multilagenschichten die thermische Stabilität mit einer höheren Anzahl von Lagen unabhängig von ihren Grenzflächen-Geometrien (Übergangstypen) zunimmt. Die Zersetzung von CrN in Cr_2N und weiter zu Cr über N_2-Freisetzung kann daher bis zu ~1200 ° C verzögert werden.

Des Weiteren wurde eine monolithisch gewachsene Gradienten-Schicht synthetisiert, mit einem kontinuierlichen Übergang von (Al,Cr)N zu $(Al_xCr_{1-x})_2O_3$ und zurück zu (Al,Cr)N - unter Verwendung von pulvermetallurgisch hergestellten $Al_{0.7}Cr_{0.3}$ Targets. Die Übergangszone von Nitrid zu Oxid wurde im Detail durch TEM-SAED und STEM-EDS untersucht, um die strukturelle und chemische Entwicklung zu verstehen, die durch kontinuierliche Übergänge oder unscharfe Grenzflächen zwischen einzelnen (Al,Cr)N und $(Al_xCr_{1-x})_2O_3$ Lagen stattfindet. Diese Information wurde verwendet, um die $(Al_xCr_{1-x})(O_{1-y}N_y)$ -Dünnschichten mit speziell zugeschnittenen strukturellen und chemischen Eigenschaften abzuscheiden und im Detail auf ihre thermische Stabilität zu untersuchen. Die DSC/TGA-Ergebnisse weisen erneut darauf hin, dass im Falle von (Al,Cr)(O,N) die thermische Stabilität mit zunehmenden Sauerstoffgehalt steigt. Die Zersetzung von CrN in Cr_2N und anschließend zu Cr über N_2-Freisetzung kann erfolgreich von ~1090 auf 1150 °C erhöht werden. Diese ist somit nur um 50 °C niedriger als die zuvor erwähnte mehrschichtige Anordnung von einzelnen (Al,Cr)N und $(Al_xCr_{1-x})_2O_3$ Lagen.

Abschließend wurden monolithisch gewachsene und mehrlagige $(Al_xCr_{1-x})(O_{1-y}N_y)$-Schichten, die durch einfaches regeln der Durchflussrate synthetischer Luft beim reaktiven Lichtbogenverdampfen der pulvermetallurgisch hergestellten $Al_{0.7}Cr_{0.3}$-Targets entwickelt. Die Erhöhung der absoluten Durchflussrate an synthetischer Luft von 200 auf 1100 sccm führt zu einem höheren Sauerstoffgehalt in den monolithisch

gewachsenen Schichten; und damit zu einem Übergang von einer dichten (Al,Cr)N-artigen relativ glatten Hartstoffschicht mit einphasiger fcc-Struktur zu einer säulenartigen $(Al_xCr_{1-x})_2O_3$ Struktur mit kubischen und hexagonalen Phasen. Diese Oxidschichten haben eine deutlich höhere Defektdichte und Oberflächenrauigkeit als die entsprechenden Nitride und deshalb nimmt die Härte dieser Schichten von ~33 auf 15 GPa mit zunehmender Sauerstoffgehalt ab. Im Unterschied dazu zeigen die entsprechenden Multilagenschichten Härtewerte von ~26 GPa, bei einphasigen fcc-Strukturen. Die thermische Stabilität der mehrlagigen (Al,Cr)(O,N) Schichten (mit alternierendem O und N Gehalten), die mittels Regulierung der Durchflussrate der verwendeten synthetischen Luft synthetisiert wurden, nimmt mit zunehmenden Sauerstoffgehalt zu. Die Temperatur ab der die Zersetzung von CrN in Cr_2N und weiter zu Cr über N_2-Freisetzung einsetzt, kann bis zu 1200-1300 °C erhöht werden. Ebenso erhöht sich auch die Temperatur ab der die metastabilen $fcc-(Al_xCr_{1-x})_2O_3$ Phasen zu $\alpha-(Al_xCr_{1-x})_2O_3$ umwandeln.

List of Figures

List of Tables

List of Abbreviations and Symbols

ADF.. Annular Dark Field

AEM ....Analytical Electron Microscopy

BB .... Bragg Brentano

BF .... Bright Field

BSE .... Back Scattered Electrons

CAE.. Cathodic Arc Evaporation

CVD .... Chemical Vapour Deposition

DF.. Dark Field

DDF .... Dirty Dark Field

DSC...Differential Scanning Calorimetry

DTA ....Differential Thermal Analysis

ED(X)S .... Energy Dispersive X-ray Spectrometry

EELS...Electron Energy Loss Spectrometry

FEG ....Field Emission Gun

GID .... Grazing Incidence Diffraction

HAADF...High Angle Annular Dark Field

HR ....High Resolution

PVD .... Physical Vapour Deposition

SAED.. Selected Area Electron Diffraction

SE ....Secondary Electrons

SEM ....Scanning Electron Microscopy

STA ....Simultaneous Thermal Analysis

STEM ....Scanning Transmission Electron Microscopy

SZM ....Structure Zone Model

TEM.. Transmission Electron Microscopy

TG..Thermogravimetry

TGA .... Thermogravimetric Analysis

XRD ....X-ray Diffraction

ZLP...Zero Loss Peak

Symbols

N ....total number of atomic places

N_v ....number of vacancies under equilibrium conditions

Q_v ....energy needed to create a vacancy

k ....Boltzmann-constant

R .... gas constant

T .... absolute temperature [K]

Γ ....jump frequency of an atom jump

Z .... concentration of unoccupied lattice sites

Q_m ....activation energy for migration

v .... vibration frequency of the atoms around their equilibrium position

D...diffusivity or diffusion coefficient

α ....jump distance of an atom jump

D_0 ....total number of atom jumping attempts

H_m.. enthalpy of migration

S_m ....entropy of migration

J...diffusion current density

c .... concentration

$\bar{x}$.. average path

t.. time

T_m .... melting point temperature

D_b .... lattice or bulk diffusivity

D_d .... dislocation diffusivity

D_{gb} ....grain boundary diffusivity

D_{pb} .... phase boundary diffusivity

D_s..surface diffusivity

G..Gibbs free energy

U..internal energy

P .... pressure

V .... volume

S ....entropy

H .... enthalpy

ΔG_{mix} .... intermixing Gibbs free energy

ΔS_{mix} .... intermixing entropy

ΔH_{mix}..intermixing enthalpy

ΔG_N .... overall energy of a nucleus

ΔG_s .... energy cost to form a new surface

ΔG .... energy gain to form a new phase

ΔG^* .... energy barrier

ΔG_V .... volume dependent part of energy of a nucleus

γ .... surface energy of the nucleus

r .... radius of a nucleus

r^* .... critical radius of a nucleus

π .... Pi

T^* .... generalised temperature

E^* .... normalised energy

t^* .... film thickness

n .... integer

λ .... wavelength

θ .... diffraction angle

d_{hkl} .... distance between neighbouring parallel lattice planes

h,k,l .... miller indizes

a .... lattice parameter

K_{α} .... characteristic photon energy

Å .... Angström

K .... scattering vector

CHAPTER **1**

1. Introduction and Motivation

1.1 Historical Aspect

Materials are deeply anchored in our culture. Transport, accommodation, clothing, communication, recreation, entertainment, food production – every area of our daily life is influenced by one or other type of materials. Historically, the development and change of society has always been closely tied to the ability of its members to produce and modify materials in order to meet their needs. Previous civilizations were even named according to the prevailing materials (e.g., Stone Age, Bronze Age, and Iron Age). The early humans only had access to a limited number of naturally occurring materials such as stone, wood, clay, and leather. In the past, they have developed processes for the production of materials which have better properties than the naturally available materials (e.g., ceramics, later different metals). In addition, they discovered that the properties of materials can be modified by thermal treatment or by adding additional substances. At this time the use of materials was a pure selection process. It was decided which of the few materials available was most suitable for the intended application. Only recently did scientists come to the realization that the structural elements of materials are related to their properties. This knowledge, accumulated over the last 100 years, put them in the position to change their features more and more. Thousands of different materials have been developed that meet the requirements of our modern and complex society with special characteristics. These include the material classes, metals, plastics, glasses, ceramics as well as composite materials from two or more afore mentioned classes, but also structures such as fibers, foams, layers, etc.

The development of many technologies that make our lives more comfortable is closely tied to the availability of the corresponding materials. A closer understanding of the structure and characteristics of a machine is often the first step towards improving the manufacturing process. Motor vehicles, e.g. would not exist without the availability of cheap steel, electronic devices such as computers and smartphones are only accessible to the private user because semiconducting materials and components can be produced at low prices [1].

1.2 Why do we investigate materials?

Many scientists and engineers from a wide range of disciplines are faced sooner or later with development tasks involving material questions. Materials scientists and engineers are specialists in materials research and design. It is often a matter of selecting a suitable material from a variety of possibilities. The final decision depends on different criteria. The operating conditions must first be defined, since they determine the required properties. Only rarely does a material have an optimal combination of all desired properties. Therefore it is often necessary to compromise. A classic example is its strength and formability. Normally a very hard material has only a limited ductility. A second selection criterion is the resistance of the material under application conditions. Increased application temperatures or corrosive environment often lead to a considerable loss in efficiency and lifetime of e.g. a tool or component. Economic considerations are often the decisive factor. What will the finished product cost? Perhaps a material is found that shows all the desired properties of a product, but is much too expensive. Again, a compromise is indispensable. The costs of a product also always include all production costs and sometimes also disposal or recycling costs. The more familiar an engineer or scientist is with the various characteristics, structure-property-relation and processing technologies, the more effective and safer he or she will be able to make a material selection based on these criteria [1].

1.3 Scope of this thesis

In the following chapter of this work, a brief summary of basically material science and engineering is given, including general material properties and the important ongoing physical as well as chemical mechanism behind it. A further chapter deal with the deposition of hard coatings, describing different deposition techniques, the principles of plasma discharge as well as the operation of arcs and its suitability, performance, control, capabilities, and limitations for cathodic arc evaporation which are intended to provide the reader with a basic understanding and appreciation of this deposition equipment. Basically mechanism of film growth as well as (for this thesis important) material systems and arrangements are described in detail, before the next chapter about characterization techniques starts. The sections in this chapter have been carefully selected to include primarily characterization techniques used within this thesis, including X-ray diffraction, scanning electron microscopy, transmission electron microscopy, nanointendation, profilometry, and simultaneous thermal analyses.

Finally, the actually heart of this work, the experimental results and their discussions accompanied by a specific introduction to the field can be found within the last chapters.

CHAPTER 2

2. Theoretical Background

2.1 Material properties

Material properties can be divided into acoustical, atomic, chemical, electrical, magnetic, manufacturing, mechanical, optical, thermal, and other properties. Material scientists are often interested in realising a multitude of these properties specifically tailored for individual applications (by intermixing materials at the atomic scale).

For machining and forming tools, for instance, required characteristics (at application temperature) are high hardness and toughness, defined thermal conductivity, controlled adhesion, minimum diffusion, low friction coefficient, high thermal stability, oxidation and corrosion resistance, which are based on the atomic structure and chemical bonding of the combined elements.

2.1.1 Atomic Structure and Chemical Bonding

Solid materials are built up by atoms, which themselves are composed of a positively charged core and a negatively charged electron-shell. Electrons in the outer shell are mainly responsible for the interaction between atoms. As a consequence of energy minimization each atom is anxious to possess a noble gas electron-configuration. Therefore atomic bonds are formed in order to fill their outer shells by shared electrons.

The three major bonding types, fundamental for the structure and properties of matter, are:

Ionic bonding occurs between atoms with a lower ionisation energy as for instance, Alkali- (Li, Na, K, etc.) and Alkaline earth metals (Be, Mg, Ca, etc.) on the one hand, and elements with a high electron affinity, e.g., halogens (F, Cl, Br, etc.) on the other hand. A low ionisation energy implies that it is, from an energetically point of view, more favourable to provide an electron (i.e., turning into a positively charged cation) than accepting it. The latter atom, now with an additional electron, is referred to as anion. In order to produce charge neutrality, this type of bonding is non-directional.

Covalent bonds are defined as sharing of electron pairs between atoms. This interaction leads to the formation of hybrid orbitals in solid materials. Typical examples are Si, Ge, and C (diamond structure). Hybrid orbitals are supposed to be combinations of atomic orbitals, superimposed on each other in various proportions. The crystal structure highly depends on the type of the hybridisation: sp (linear), sp^2 (trigonal), or sp^3 (tetragonal). For example carbon is able to form a two-dimensional graphite structure and a three-dimensional diamond structure, depending on the respective sp^2 and sp^3 hybridisation. Here the binding is highly directional.

Metallic bonding occurs as a result of an electrostatic interaction between the conduction electrons (in the form of a delocalized valence electron gas) and the positively charged atomic cores. It can also be described as the sharing of free electrons among a lattice of positively charged ions (cations). Because the binding is completely non-directional, we expect crystals with the densest packing of spheres.

The above explained primary bond types describe an idealised case of a material. In general however, solid materials consist of a mixture of ionic, covalent, and/or metallic bond contributions. The bond energy of these primary bonds is in the range of 100–1250 kJ/mol. [2].

Ceramics:

According to their prevailing bonding type in metallic, covalent, and ionic, their expected structure and general characteristics, Holleck and Stüber [3–7] have developed a classification scheme, see Fig. 2.1 of hard ceramic materials.

The structure in which a solid material crystallises, can explain (to a certain extent) the macroscopic properties. For example, metallic hard materials, such as CrN and Cr_2N possess a good adhesion to metallic substrates. They also exhibit the highest toughness compared to other hard materials. Due to their strong covalent bonds, covalent hard materials, such as AlN, have a high temperature strength and high hardness. Ionic hard materials, such as Al_2O_3 usually show chemical inertness, as well as a high chemical and thermal stability.

Advantageous properties and characteristics of individual hard materials can be combined in one structure, by forming thermodynamically stable or metastable mixed crystals. For instance, AlN (covalent hard material) can be forced into the lattice of a face centred cubic crystal, e.g., CrN or TiN. The results are a good adhesion to metallic substrates, high hardness, high toughness, and high temperature strength [3].
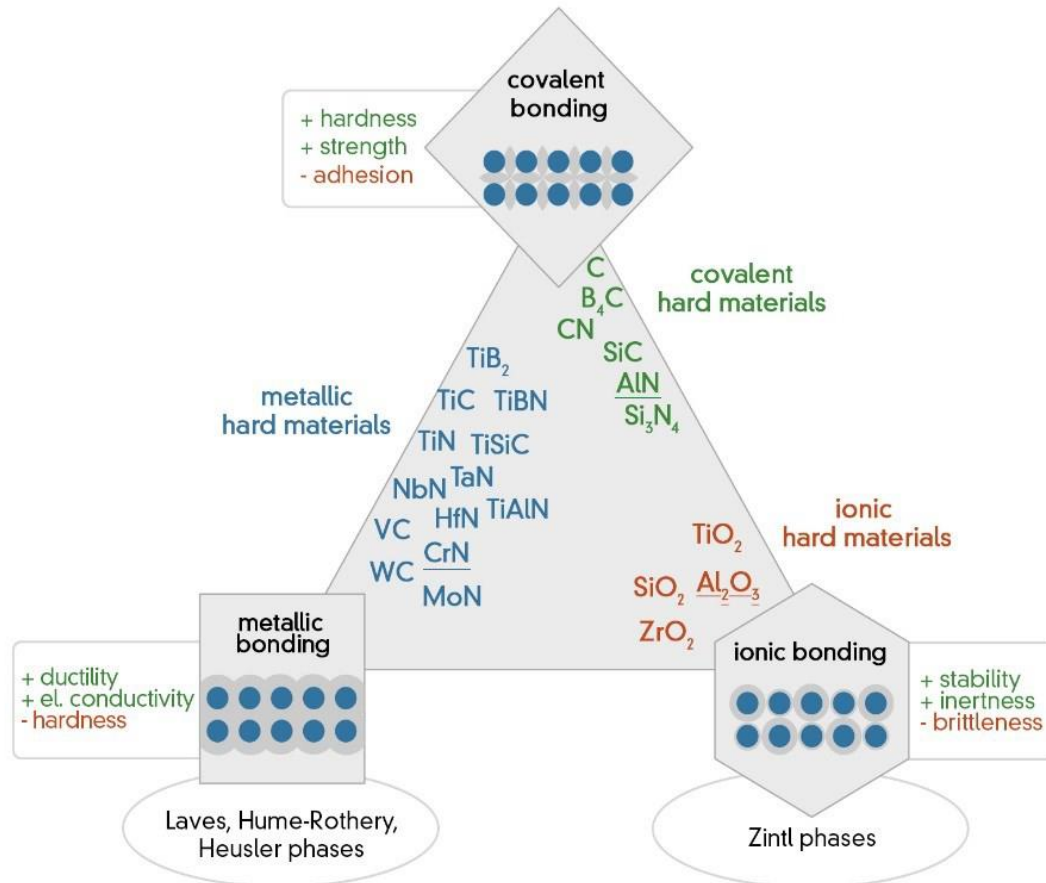
Fig. 2.1: Classification of hard ceramic materials according to their bonding character [8], originally from [4].

So far, it has been assumed that a consistently perfect order prevails at an atomic level in a crystalline structure. However, this is an ideal idea. In real materials and especially in PVD coatings, a large number of defects or lattice imperfections occur in large numbers. In fact, many material properties are significantly influenced by the deviations from the ideal (order) structure—which not necessarily ought to be unfavourable. Often, specific material properties are adjusted by deliberately introducing an appropriate defect concentration. Lattice defects are irregularities of the lattice of the order of one or more atomic diameters. The classification of lattice defects is often based on their geometry or dimensionality [1].

2.1.2 0–dimensional lattice defects (point defects)

The simplest point defect is a vacancy i.e. a lattice site remains unoccupied, see Fig. 2.2. All crystalline solids contain vacancies. In fact, almost no material can be produced without vacancies. This can be explained by thermodynamic laws, the existence of vacancies leads to an increase in the entropy of the crystal, hence an energetically more

favourable state. The number of vacancies under equilibrium conditions N_V increases for a given solid with the temperature according to the following relationship [1]:

$$N_V = N \exp\left(-\frac{Q_V}{kT}\right)$$

(2.1)

N is the total number of atomic places, Q_V is the energy needed to create a vacancy, T is the absolute temperature (in K), and k is the Boltzmann-constant. Hence, the number of vacancies increases exponentially with the temperature. For most materials, the vacancy density below the melting temperature is in the order of 10^{-4} (i.e., one lattice site of 10 000 atomic places remains unoccupied).

A self-interstitial atom is an atom of the crystal that has been forced into an interstitial space. In metals, such an intrinsic interstitial atom causes relatively large lattice distortions since the atom is much larger than the available interstitial space to which it has been forced. As a result, the formation of such a lattice defect is not very likely and the concentration of such lattice defects is very small. In particular, compared to vacancy concentration, the concentration of intrinsic interstitial atoms is significantly lower.
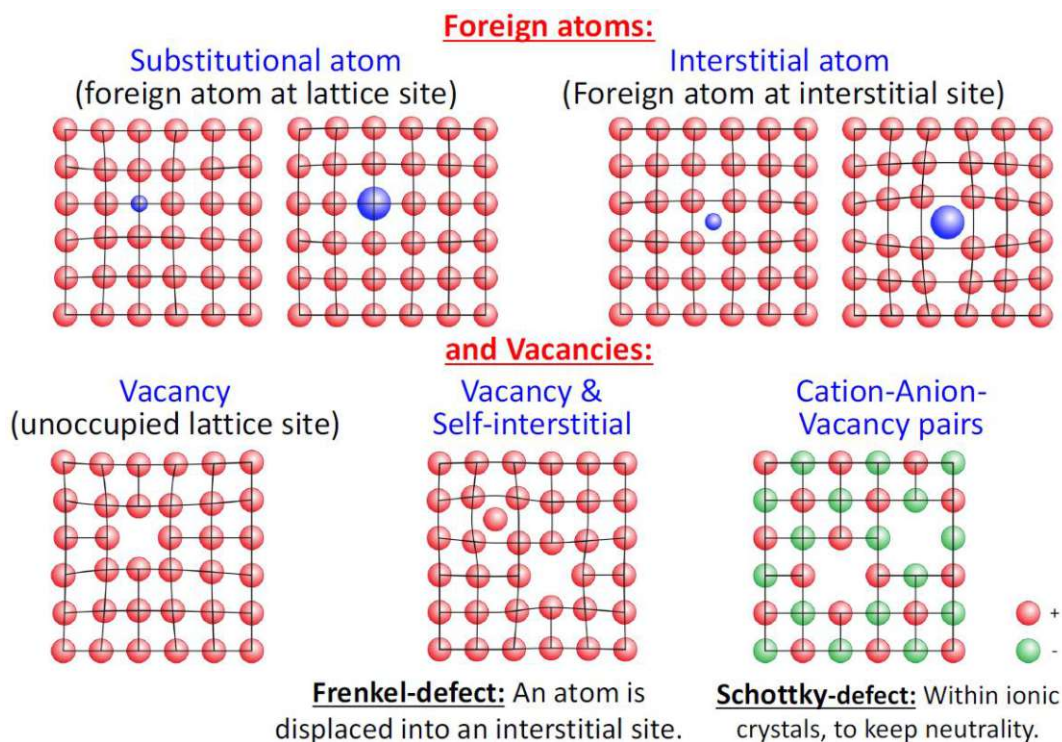
Fig. 2.2: Different types of point defects [2].

Pure metals consisting of only one atomic species practically do not exist. Impurities in the form of foreign atoms are always present and some of them act as crystalline point defects. In practice, it is difficult to produce metals with a purity of more than 99.9999%, even by means of technically mature methods. Most of the known metals are not pure, but rather alloys whose properties are modified by the added addition of foreign atoms. Usually, alloying is used to increase the mechanical strength and the corrosion resistance of materials. The addition of foreign atoms to metals leads to the formation of solid solutions and/or the formation of a second phase (Fig. 2.3) depending of the nature of the foreign atoms, their concentration and the temperature. The latest is called order(ing) phase. At a certain quantity ratio as well as in a certain temperature interval, a uniform and symmetrical atom distribution occurs without changing the type of lattice. The formation of such order phases may lead to sudden changes in the electrical and magnetic properties. In a solid solution the crystal structure of the host material (matrix) does not change by the addition of randomly distributed or ordered foreign atoms. There are two types of foreign atoms: substitution atoms and interstitial atoms (interstitially dissolved atoms). Requirements for the formation of a substitution solid solution are the following. The atoms of both elements occupy the same lattice sites. This phase is formed when the lattice type is the same and the lattice constant as well as the atomic radii differ by less than 15 %. Also the difference in the electronegativity as well as the number of valence electrons should be small.

1.1) Interstitial solid solution

1.2) Substitutional solid solution with irregular distribution

2) Ordered (substitutional) **solid solution**

E.g.: Fe – C
Fe – N
Ta – H

E.g.: Fe – Cr
Ni – Cr
Cu - Zn
Nb – W

E.g.: Cu – Au
Ti – Al
Ni – Al
Ni – Fe
Fe – Co
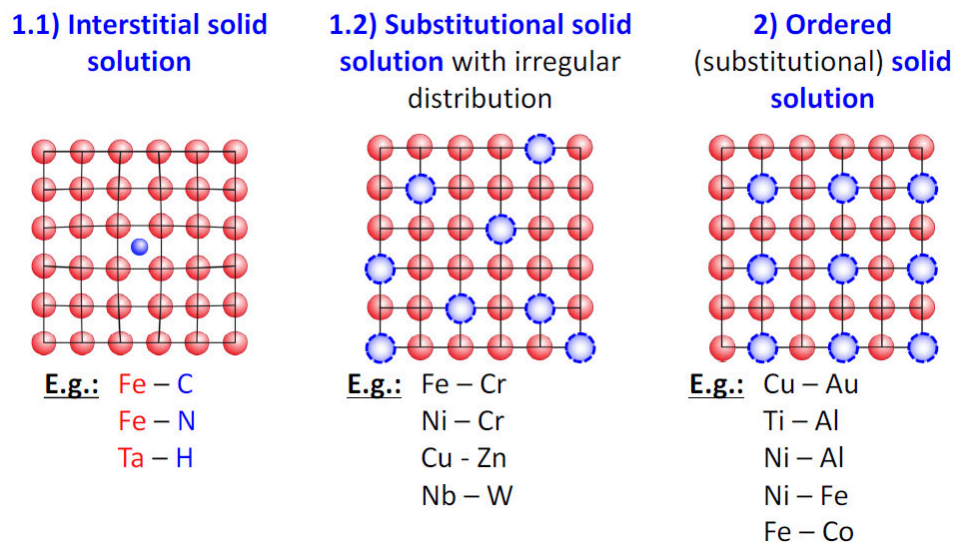
Fig. 2.3: Different variations of solid solutions [2].

Another type of solid solution is the interstitial solid solution. Here, the foreign atoms occupy the cavities or interstitials between the host atoms, see Fig. 2.2. In the case of metallic materials with relatively high packing densities, these interspaces are comparatively small. As a result, the diameter of the interstitial atoms must be substantially smaller than that of their host atoms (<10%). Since even very small intermediate lattice atoms are larger than the available intermediate lattice sites, they cause a lattice strain of the neighbouring host atoms.

In ceramics, vacancies as well as the occupation of interstitials are possible. However, since ceramics consist of at least two types of ions, both defects can occur for each type of ion, see Fig. 2.2. In the NaCl crystal, for example, both Na/Cl-defects and Na^+/Cl^- ions can be found on interstitial sites. The term "defect structure" is often used to describe the type and concentration of atomic building defects in ceramics. Since the atoms appear as charged ions, when defect structures are considered, the conditions of electroneutrality must be observed. Electroneutrality is the state when the number of positive and negative charges of the ions are equal. For this reason, lattice defects in ceramics cannot occur individually. One of these defect types is a combination of cationic defect and interstitial cation called Frenkel defect. It occurs when a cation leaves its lattice site and travels to an interstitial space. Another defect type is a combination of anion and cationic defects known as the Schottky defect. It is formed when a cation and an anion are removed from the lattice. Since cation and anion have the same (opposite) charge and an anion defect exists for each cation defect, the charge neutrality of the crystal is retained. The ratio of cations to anions is not changed in either Frenkel or Schottky defects. As long as there are no other defects, the material is stoichiometric.

2.1.3 1–dimensional lattice defects (line defects)

A dislocation is a linear or one-dimensional defect in which some atoms are displaced in the crystal lattice. There are basically two types of dislocations. The edge dislocation is a linear defect that concentrates on the line along an (additionally) inserted half-plane of atoms. This line is called a dislocation line. For the edge dislocation shown in Fig. 2.4a, the dislocation line is perpendicular to the paper plane. In the vicinity of the dislocation line, the lattice is locally distorted. The atoms above the dislocation line are under compressive and those below the line under tensile stress. The screw dislocation as the second dislocation type can be illustrated by the idea of a shear stress which leads to a distortion of the lattice as sown in Fig. 2.4b. In this case, the upper region of the crystal is shifted an atomic distance to the right relative to the lower one. The resulting distortion of the lattice is also linear and extends along a dislocation line. Most dislocations in crystalline materials are neither pure edge nor pure screw dislocations, but have both components (mixed dislocation, Fig. 2.4c). The lattice distortions caused by the dislocation can be described in terms of their magnitude and direction by the Burgers vector b. In the case of edge dislocation, the dislocation line and the Burgers vector are perpendicular to each other, in the case of screw dislocation they are parallel, and in the case of mixed dislocations they are neither parallel nor perpendicular to each other. For the latter the Burgers vector stays the same but the vector of the dislocation line changes, see Fig. 2.4.
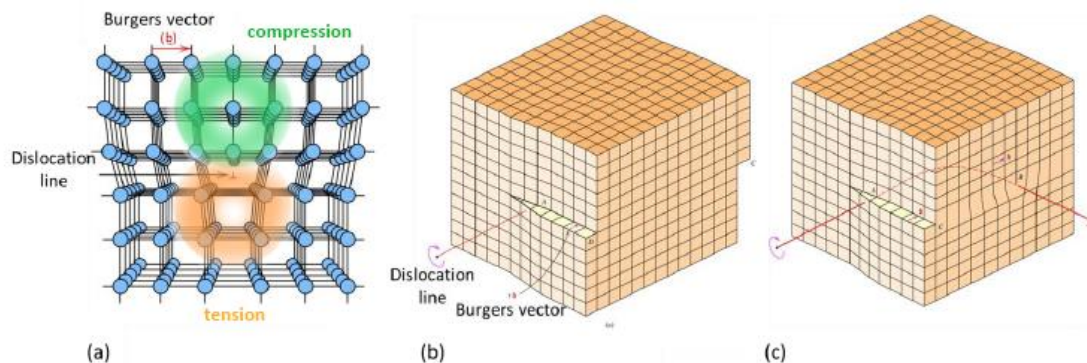
Fig. 2.4: (a) Arrangement of atoms in the vicinity of an edge dislocation; (b) screw dislocation; (c) mixed dislocation in a crystal (adapted from) [1].

2.1.4 2–dimensional lattice defects (area defects)

Area defects include two-dimensional interfaces, which delimit material regions with different crystal structures and/or crystallographic orientation from each other, see Fig. 2.5. This includes the surface of the solid, grain boundaries, phase boundaries, twin boundaries, and stack errors.
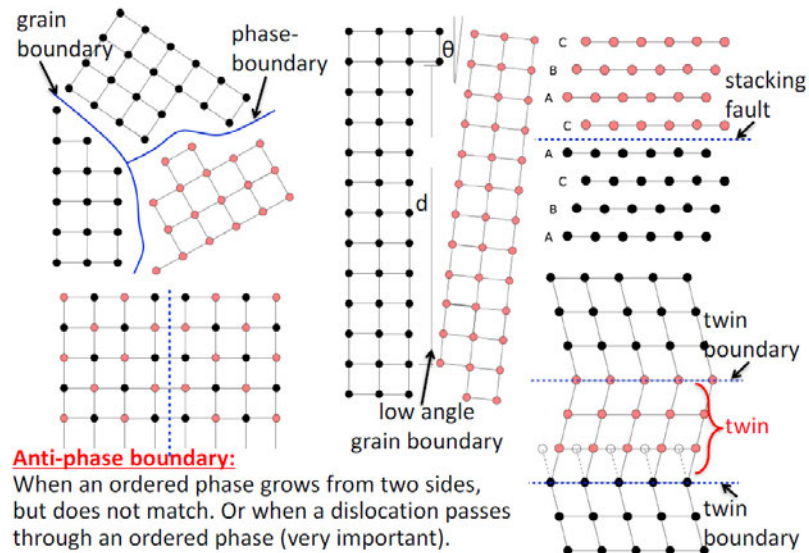
Fig. 2.5: Different t of area defects [2].

2.1.5 3–dimensional lattice defects (volume defects)

In solid materials, there may be additional defects than the defects discussed above, which might have a huge influence on the material properties (i.e. hardness or thermal stability). These include pores, cracks, inclusions, and additional phases that may have been introduced into the material during the manufacturing process and various manufacturing steps.

2.2   Dislocations and strengthening mechanisms

Materials can in general be subjected to two types of deformations: the elastic (reversible) and the plastic (permanent) deformation. Strength and hardness are the resistance of the material to (plastic or elastic or both) deformation. At the microscopic level, the plastic deformation corresponds to the displacement of a large number of atoms, caused by an applied mechanical (or thermal) stress, during which, atomic bonds are broken and re-formed. In crystalline solids, the plastic deformation usually involves the movement of dislocations.

2.2.1 Movement of dislocation

The process of plastic deformation by dislocation movement of is called sliding. The crystallographic plane along which the dislocation line is moved is the sliding plane, Fig. 2.6a. The macroscopic plastic deformation corresponds to the permanent deformation caused by the movement of dislocations (or sliding) due to applied shear stresses τ. When the last leg is pulled in, the caterpillar in Fig. 2.6b forms a hump. The hump pushes itself forward by repeatedly lifting and moving the pairs of legs to the front of the caterpillar. When the hump has reached the front end, the entire caterpillar has moved forward by one leg. The hump of the caterpillar and its movement correspond to the inserted half-plane of atoms in the displacement theory for the explanation of the plastic deformation.
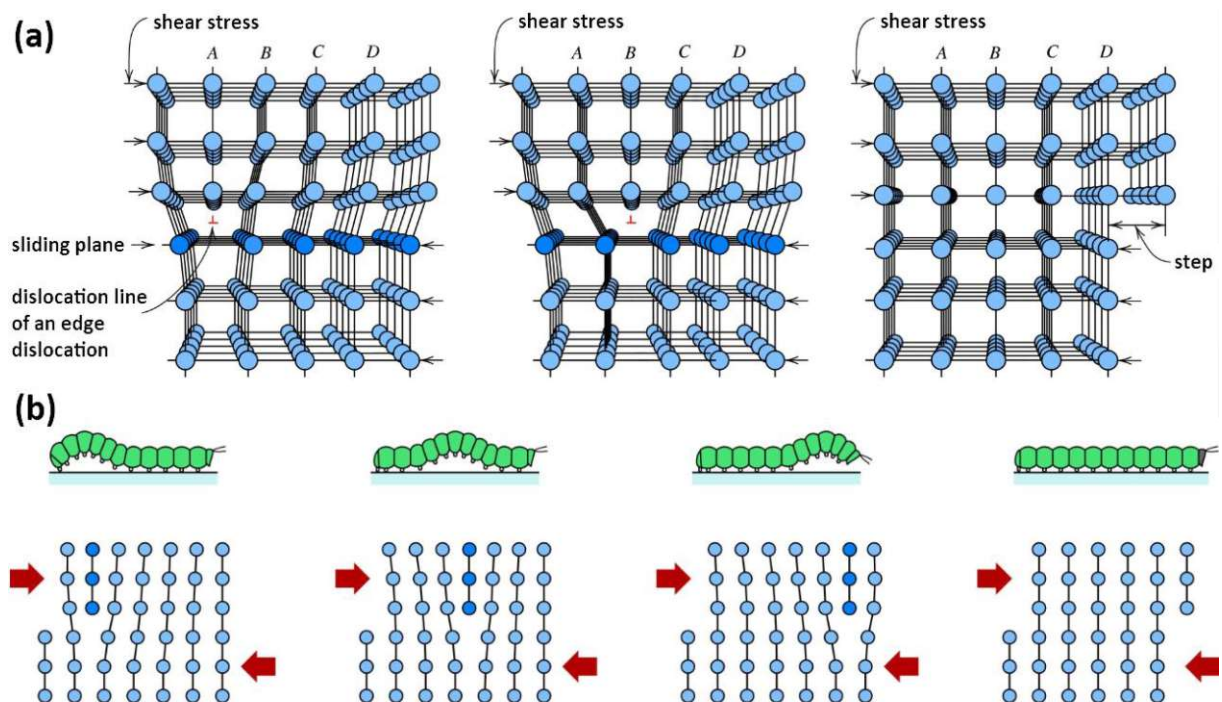
Fig. 2.6: (a) Rearrangement of atoms when an edge dislocation moves by an applied shear stress. (b) Representation of the analogy between the movement of a caterpillar and a dislocation movement [1].

In the case of edge dislocation the lattice of the crystal is distorted across the whole depth, while for a screw dislocation the lattice is distorted along the whole width (by a Burgers-step), see Fig. 2.7. The first dislocation moves in the direction of the applied shear stress (over the depth) through the depth of the crystal, while the latter one moves across the direction of the applied shear stress (over the width) through the width of the crystal. However, the movement of dislocations is always perpendicular to the dislocation line. The dislocation line cannot originate or end within the crystal (except a closed loop), only at grain boundaries or initial surfaces. Dislocations cannot move on all crystallographic planes and directions with the same ease. Generally, there is a preferred plane in which the dislocation movement occurs in certain directions. This plane is called sliding plane and the direction of movement is referred to as the sliding direction. This sliding-system is dependent on the crystal structure. For a given crystal structure, the sliding plane correspond to the densest packed plane, while the sliding direction corresponds to the densest packed direction.

Fig. 2.7: Formation of a stage on the surface of a crystal by the movement of an edge dislocation and a screw dislocation. The dislocation line of an edge dislocation moves in the direction of the applied shear stress τ. In the case of a screw dislocation, the movement is perpendicular to the applied shear stress τ [2].

2.2.2 Cold working

The process of cold working can be explained by the interaction between dislocations and the stress fields around the dislocations. The dislocation density in a metal increases with increasing degree of deformation, multiplying or forming new dislocations. Hence, as the average distance between the dislocations decreases, the dislocations move closer together. The movement of a dislocation is hindered by the presence of other dislocations. Therefore, an increased stress (force) is necessary to deform the metal with increasing grade of cold working.

2.2.3 Solid solution strengthening

A further method of strengthening or hardening materials is alloying with foreign atoms, whereby either a substitutional or an interstitial solid solution is produced. The solution of foreign atoms leads to a lattice shift of the surrounding matrix atoms and thus generate a long-range strain field within a lattice. Interstitials typically have a higher impact than substitutional atoms regardless if they are smaller or larger than the matrix atoms. As a consequence of the interaction between dislocations and the solute atoms, the dislocation movement (sliding) is hindered, see Fig. 2.8.

Fig. 2.8: Solid solution strengthening due to the interaction of dislocations with substitutional or interstitial atoms [2].

For example, a foreign atom which is smaller than the matrix atoms causes an elastic distortion in the surrounding crystal lattice, thus producing a tensile stress field. A larger substitutional atom, on the other hand, produces a stress-strain field in its immediate surroundings. To reduce the total strain energy, the solute atoms tend to diffuse to the dislocations and segregate around them. Hence, a part of the deformation is compensated for the surrounding lattice. The resistance to sliding is higher in the presence of solute atoms, since the overall elongation of the lattice must increase as the dislocations unpin. In addition, interactions between foreign atoms and migrating dislocations occur during plastic deformation. Therefore, a higher stress is required in alloys with solid solutions in comparison to pure metals in order to initiate and sustain the plastic deformation.

2.2.4 Grain refinement strengthening

Grain and phase boundaries strongly influence the dislocation movement in a polycrystalline material. Neighbouring grains usually have different crystallographic orientations resulting in the development of grain boundaries. During the plastic deformation, sliding or movement of dislocations occur across these boundaries. At large-angle grain boundaries, dislocations cannot pass through (during the deformation), but they accumulate at the boundary, resulting in an increased stress concentration far beyond the sliding plane. Consequently new dislocations occur in the neighbouring grains. Hence, the active shear strength on the neighbouring sliding plane is different and thus a higher force is required to initiate dislocation movement in the neighbouring grains. Fine-grained materials exhibit a high fraction of grain boundaries that hinder dislocation movement than coarse-grained materials. Low-angle boundaries are less effective, due to their small misorientation, while twin boundaries and phase boundaries are extremely effective. Therefore, the size and distribution of the grains and individual phases have an immense impact on the material´s mechanical properties. In addition to the hindering of the dislocation mobility, decreased grain sizes lead also to a reduced pile up of dislocations at the grain boundaries, resulting in reduced stresses for neighbouring grain sliding. Furthermore, for extremely small grains no dislocations are formed, as these directly would be built into the grain boundaries, see Fig. 2.9.
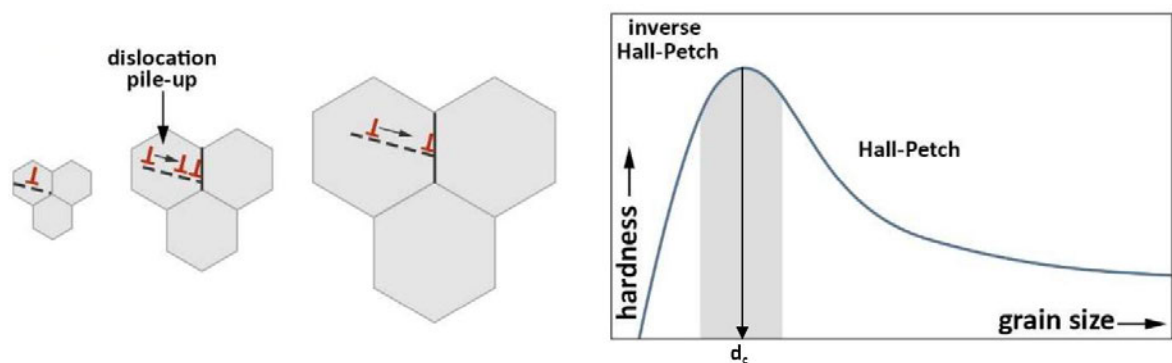
Fig. 2.9: Grain refinement strengthening [9].

It should also be mentioned that the grain refinement results in many alloys not only to an increased strength, but also to an improved toughness. If the volume fraction of the grain boundary area increase with decreasing grain size, grains are able to glide on each other more easily (grain boundary gliding), leading to a softening of the material. The critical grain size d_c for this reverse (softening) effect depends on the binding strengths and the cohesive energy of the grain boundaries.

2.2.5 Particle & precipitation strengthening

The formation of fine, homogeneously distributed particles (precipitates) of a second phase within the matrix leads to a certain strength and hardness increase in some metals. This is achieved by phase transformations caused by suitable heat treatment. This process is referred to as precipitation hardening or age hardening.

Some alloys are precipitation-hardenable, i.e., the strength can be increased by the formation of very small particles of a second phase. The control of the particle size and consequently the strength is controlled by two heat treatment steps. In the first step, solution annealing takes place where all foreign atoms are dissolved, so that a single-phase solid solution is formed. The subsequent quenching to comparatively lower temperatures preserves this condition. During the second heat treatment, the precipitation heat treatment (at a constant temperature) are formed by precipitation particles which increase in size. Strength, hardness and ductility depend on the annealing time and therefore on the particle size. The increase in strength can be explained by an increased resistance to dislocation movement due to lattice distortions arising in the vicinity of these microscopic precipitation particles.

2.3 Diffusion

Diffusion can be described as mass transport by the migration of atoms. Many reactions and processes that are important for the treatment of materials require mass transport either within a solid body or from a gas/plasma, a liquid or another solid substance into the considered solid body.

2.3.1 Diffusion mechanisms

Atoms moving stepwise from one lattice position to the next during diffusion. In fact, atoms are constantly moving in solids, changing their positions. The diffusing atom must provide sufficient energy to break the bonds of neighbouring atoms causing certain disturbances of the lattice structure during the displacement. At a given temperature, a small amount of atoms has sufficient oscillation energy to carry out diffusion movements. The energy for overcoming this barrier is also known as activation energy for migration Q_m, see Fig. 2.10. Together with other parameters such as temperature T, gas constant R, concentration of unoccupied lattice sites z, vibration frequency ν of the atoms around their equilibrium position, these parameters are able to describe the jump frequency Γ of an atom jump [10]:

$$\Gamma = z\nu \exp\left(-\frac{Q_m}{RT}\right) \tag{2.2}$$

Hence, the jump frequency describes the probability of an atom jumping to a neighbouring lattice site.

The diffusivity D can be defined as:

$$D = \frac{1}{6}\alpha^2\Gamma \tag{2.3}$$

With α describing the jump distance. Integrating Eq. 2.2 in 2.3, while considering that $Q_m = H_m - TS_m$, H_m and S_m are the enthalpy and entropy of migration, the diffusion coefficient can be written as:

$$D = \left[\frac{1}{6}\alpha^2 z\nu \exp\left(\frac{S_m}{T}\right)\right] \exp\left(-\frac{H_m}{RT}\right) \tag{2.4}$$

A simplified version is:

$$D = D_0 \exp\left(-\frac{Q_m}{RT}\right) \tag{2.5}$$

The diffusion constant D_0 describes the total number of atom jumping attempts, while Q_m represents the activation or migration energy for diffusion.

Substitutional and interstitial diffusion are two of the most relevant diffusion mechanism in metals (or solids in general).
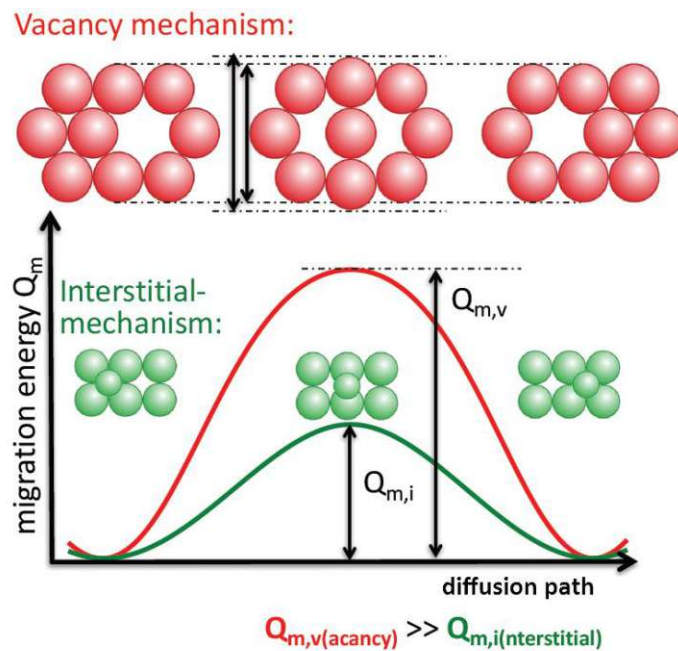
Fig. 2.10: Scheme of a vacancy and interstitial diffusion process and the corresponding variation of the migration energy [2].

2.3.1.1 Substitutional or vacancy diffusion

This process presume the existence of vacancies and describes the change of an atom from its lattice position to an unoccupied neighbouring lattice site, see Fig. 2.11a. It is depended on the present concentration of lattice defects, which can be extensive in metals at elevated temperatures.

2.3.1.2 Interstitial diffusion

This mechanism is related to the diffusion of impurities in metals such as e.g. hydrogen, carbon, nitrogen and oxygen. These atoms are small enough to occupy interstitial positions in metal lattices, Fig. 2.11b. In most metal alloys the interstitial diffusion proceeds at a significantly higher rate than the vacancy diffusion, since interstitial atoms are smaller and thus have a higher mobility. In addition, there are more interstitial positions available than vacant lattice sites, so that the probability of the interstitial atom motion is much higher compared to vacancy diffusion.

17
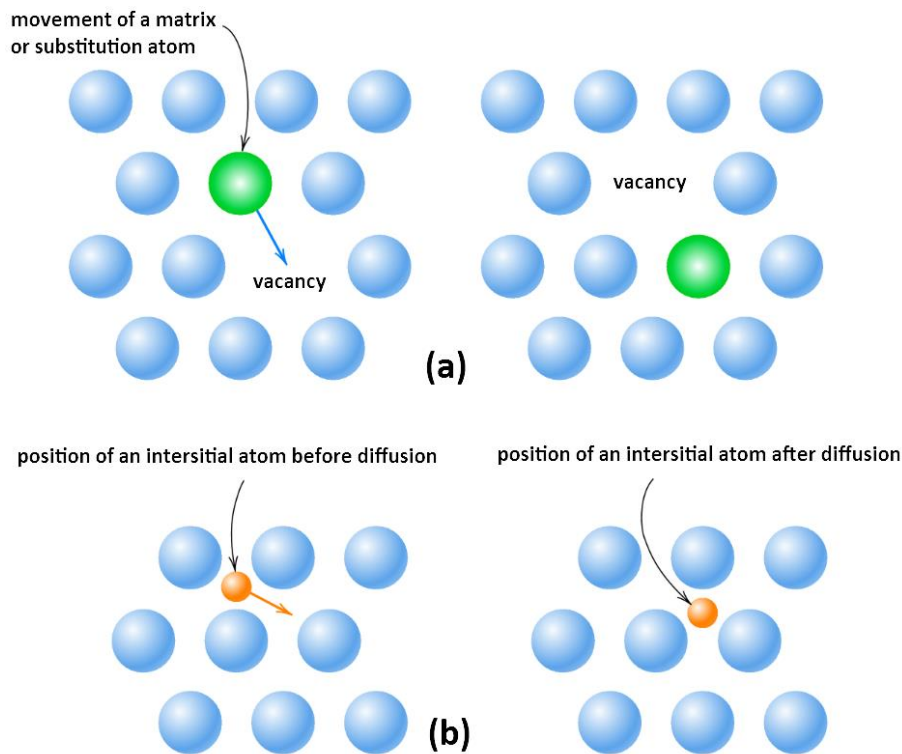
Fig. 2.11: (a) Substitutional or vacancy diffusion, (b) interstitial diffusion [1].

2.3.2 Stationary diffusion

For specific material treatments (e.g., high temperature oxidation) it is often necessary to know how fast diffusion processes take place. The rate of mass transfer is often expressed by the diffusion current density J [m^{-2}s^{-1}]. Fick´s first law, the mathematical description of the stationary diffusion in one dimension (x-direction) is comparatively simple since the diffusion current density is proportional to the gradient of the concentration c [m^{-3}] [1]:

$$J = -D\frac{\partial c}{\partial x}$$

(2.6)

The Proportionality factor D is expressed as diffusion coefficient [m²s^{-1}].The negative sign in this expression indicates that the diffusion is in the direction of falling concentration, meaning the mass of the diffusing components is transported from regions of high concentration to regions of low concentration.

2.3.3 Non-stationary diffusion

In most practical situations diffusion processes are non-stationary. This means that diffusion flow density and concentration gradient at a given point in the solid state are time dependent variables, whereby an enrichment or impoverishment of the diffusing material occurs as a net effect. Therefore, Fick´s second law of diffusion can be written

as [1]:

$$\frac{\partial c}{\partial t} = D\,\frac{\partial^2 c}{\partial x} \tag{2.7}$$

if the diffusion coefficient is independent of the concentration.

It is often sufficient to approximate the average path $\bar{x}$ [m], which an atom has covered with a diffusion coefficient D (T) at a temperature T after a certain time t.

$$\bar{x} = 2\sqrt{Dt} \tag{2.8}$$

2.3.4 High-diffusivity path diffusion

High-diffusivity paths such as grain- and phase boundaries, interfaces, dislocations, and free surfaces are generally existing in real (nano) crystals and especially in PVD synthesised coatings. These paths are associated with lower packing densities as compared to the lattice itself. Hence, the atom or ion movement is much easier along such disordered areas taking place with lower activation energies than within the crystal lattice. Consequently, the diffusion at these high-diffusivity paths is significant higher (typically 1–2 orders of magnitude) as across the bulk material: $D_b < D_d < D_{gb} < D_{pb} < D_s$, while D_b determines the lattice or bulk diffusivity, D_d the dislocation diffusivity, D_{gb} the grain boundary diffusivity, D_{pb} the phase boundary diffusivity, and D_s the surface diffusivity.

However, the low activation energies (at low temperatures) for atoms or ions in high-diffusivity paths enhance their diffusion. At elevated temperatures 0.4–0.5 T_m (T_m, melting point temperature) diffusion along grain boundaries become noticeable. This circumstance is observable in polycrystalline materials with high melting points, like ceramics or intermetallic compounds, in which fractions of dislocations and grain boundaries are reduced due to recovery and relaxation (also described as defect annihilations), as well as grain growth and recrystallization effects, resulting in the promotion of lattice (or bulk) diffusion [11].

2.4 Thermal stability

As a result of the deposition processes, PVD coatings exhibit a high concentration of built-in defects, such as vacancies, interstitial atoms, and/or dislocations, which consequently increase the potential energy of elastic deformation within the material. Especially nanocrystalline coatings, or materials in general, have a certain amount of stored internal energy due to their high interfacial-boundary-fraction. This makes them thermodynamically unstable. Protective hard coatings often have to withstand elevated temperatures in oxidation and corrosive environments—e.g. 700–1000 °C and beyond in order to meet the requirements posed to state of the-art machining applications such

as dry high-speed cutting. These consequently leads to microstructural changes, derived from an increased diffusivity. The magnitude of annealing- and oxidation-induced microstructural (defect density, dislocations and grain size) and chemical (oxide formation) modifications, represent the thermo-mechanical properties of the coating and thus the performance and lifetime of a tool or component.

2.4.1 Recovery

During the recovery process, a part of the stored internal deformation energy is relieved by annealing and rearranging of forming-induced defects (e.g., vacancies and dislocations) due to the increased diffusion rate of the atoms at higher temperatures. This results in a reduced concentration of vacancies and dislocations leading to stress reduction within the material. For PVD coatings recovery will occur on subsequent annealing treatments, which changes their microstructure and thus their properties.

2.4.2 Recrystallization

The recovered lattice still contains relatively high residual stresses (e.g. due to high defect densities in the sub grain boundaries). Minimizing this stored energy acts as driving force for continuous reactions. In contrast to recovery—which has no incubation time, meaning as soon as the activation energy is reached recovery occurs—recrystallization takes place for sufficient thermal activation ($T_R \sim 0.4$–$0.5 \, T_m$) and its incubation time is due to necessary nucleation. Nucleation of recrystallization takes place by coalescence of preferred sub-grains, leading to a reduction of the orientation-difference of neighbouring sub-grains by climbing of dislocations. Therefore, sub-grains of critical sizes are formed, which can migrate into deformed and strained regions. In other words, during (primary) recrystallization a completely new, strain- and stress-reduced microstructure is formed, due to migration of sub- and/or high angle- grain boundaries towards highly-strained regions. The primary recrystallization is often followed by normal grain growth and eventually secondary recrystallization (abnormal grain growth). Grain growth can occur within all polycrystalline materials (e.g., alloys and ceramics). The driving forces for grain growth are much smaller than for recrystallization, thus grain growth only starts at much higher temperatures. With increasing grain size the concentration of the grain boundaries decreases, causing a reduction in the total (interfacial) energy. This is the driving force for grain growth. The migration of grain boundaries leads to grain growth. Not all grains can grow. On the contrary, the larger grains grow at the expense of the smaller ones, which shrink at the same time. Thus the average grain size increases with time.

CHAPTER **3**

3. Hard Coating Deposition

3.1   Deposition techniques

Physical vapour deposition (PVD) and chemical vapour deposition (CVD) are the most common techniques for depositing thin hard protective (ceramic) coatings [12–14]. A major difference of these two techniques originates from the formation and transport mechanisms of atoms or ions (vapour) from a source to the substrate. The transition from a condensed phase (solid or liquid) to the vapour phase is based on either physical or chemical processes. In the case of CVD, the vapour is prepared by chemical reactions of halogens (e.g., F, Cl) with metal precursors (e.g., Ti, Al) which lead to the formation of a gaseous metal-halides (e.g., $TiCl_4$, $AlCl_3$). A solid reaction product nucleates and grows on a substrate surface, while volatile by-products exhaust as waste. These reactions require high driving forces (activation energy), which may be obtained by heat, plasma or ultraviolet light. Therefore, CVD calls for elevated temperatures, which cannot be tolerated by heat sensitive substrates (e.g., steels). Further limitations are e.g., available chemical reactions. In contrast to CVD, PVD enables the deposition of a large variety of inorganic materials, e.g. metals (Al, Cr, Ti, etc.), alloys, compounds (powder metallurgically produced $Cr_{1-x}Al_x$, $Ti_{1-x}Al_x$, etc.), their mixtures as well as some organic materials, which makes this technology extremely versatile in industry. Another big advantage compared to CVD arise from the relatively low deposition temperatures, enabling the deposition of heat sensitive substrates or components.

Generally, all PVD processes can be classified in three steps of thin film formation. First of all is the transformation of the source material from its solid or liquid state to the gas/plasma phase (vapour). If the source atoms (target) are ejected by a momentum transfer due to collisional impacts of an inert working gas (e.g. Ar^+-ions), this technique is called sputtering. Another PVD technique is cathodic arc evaporation (CAE), which will be described in section 3.1.3 in more detail. In CAE the transition of the solid cathode material into the plasma state directly results from a high-current low voltage arc operating on the cathode surface. The second step is the transport of the vapour from the source (target or cathode) to the substrate. The third and final step is the condensation of the arrived plasma on the substrate surface followed by film nucleation and growth [15,16]. These three steps can be controlled independently in a PVD process,

in contrast to CVD. Typically there is vacuum within the deposition chamber, which ensure minimal collisions as well as reduce involuntary reactions during the transport of the vaporized coating material.

3.2 Plasma discharges

Plasma is often described as the fourth state of matter, besides the other known states of gas, liquid, and solid. Generally a plasma is a collective quasineutral medium (gas) containing positively and negatively charged particles (e.g., cations and anions or electrons, respectively), and neutral particles (e.g., atoms). In contrast to a neutral gas, the collective behaviour of a plasma occurs from the coulomb interaction of the moving charged particles. Local moving concentrations of positive or negative charge (electrical current) result in the formation of dynamic electrical and magnetic fields, which for their part influence the motion of other charged particles far away.

The transition from a solid or liquid source into the plasma state can be achieved with several (evaporation) methods using e.g. heat, laser, electron or molecular beam, as well as ignition of a plasma [15,17]. The latest uses a high voltage at the source material to ignite the plasma discharge. The voltage-current characteristic of typical plasma discharges is shown in Fig. 3.1.
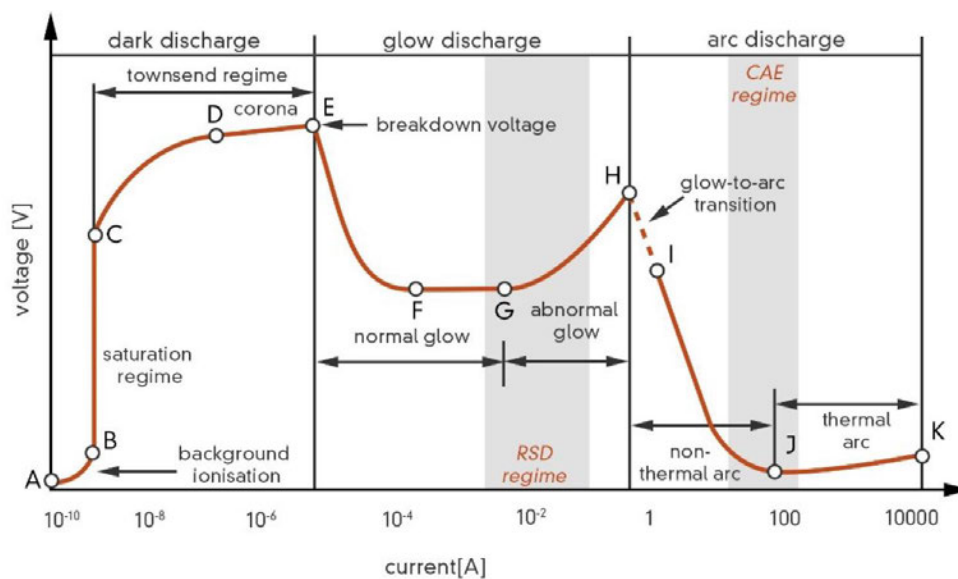
Fig. 3.1: Schematic voltage-current characteristics for plasma discharge adapted from [8], originally from [18].

A necessary condition for evaporation methods is a high vacuum deposition chamber ($P < 10^{-5}$ mbar), in which the source material is heated. In the case that the cathode material has no applied voltage (point A), only charge particles (i.e., ions and electrons) are present due to ubiquitous radiation. An applied voltage between cathode and anode lead to a current increase – which originates from the attraction of the background ions and electrons – until point B is reached. At this stage, all available charged species are

attracted, resulting in a saturation of the current. Further voltage increase up to point C is required to transfer sufficient kinetic energy to the electrons in the vicinity of the anode which than are able to ionize surrounding gas particles by cascade-like collision processes. The hereby produced ions are accelerated to the cathode and lead to a significant increase of the current. The first section (from point A to E) is called "dark discharge", which implies that no visible light is emitted here. It should be mentioned, that a dark discharge needs an external electron source to maintain a stable plasma. At point E (breakdown voltage: the beginning of the glow discharge section), a significant voltage drop as well as a simultaneous current increase can be observed. This phenomenon can be explained by the emission of secondary electrons of the cathode material, due to ion and photon impact. Consequently, electrons stabilizing the plasma are now autonomously produced by the discharge itself. The current increase with constant voltage values (from point F to G), is characterized by the entire expansion of the plasma over the cathode surface. Thermal induced electron emission occurs at point H at the cathode. A detailed description of the arc discharge is given in the following section.

3.3   Cathodic arc evaporation

Cathodic arc evaporation (CAE) features several remarkable advantages over competitive physical vapour deposition techniques (e.g., sputtering and hollow cathode evaporation), giving rise for its importance and popularity in industrially-scaled synthesis of protective coatings [19–21]. Apart from high evaporation rates and degree of ionization of source particles, its flexibility in terms of accessible material systems including metallic coatings, nitrides, oxides, and borides, represents an important key factor for its popularity and success. Deposition temperatures of 500 °C and below, also allow for the use of steels (like high speed steels) to be coated, which are significantly less thermally resistant than cemented carbides. Within this deposition method arcs are generated leading to a vaporising of the cathode, which is made out desired materials (e.g., metals, compounds, ceramics or intermetallics) to be deposited on substrates (e.g., tools or components), see Fig. 3.2. This vapour or plasma mainly consists of ions, electrons, atoms, and macroparticles.
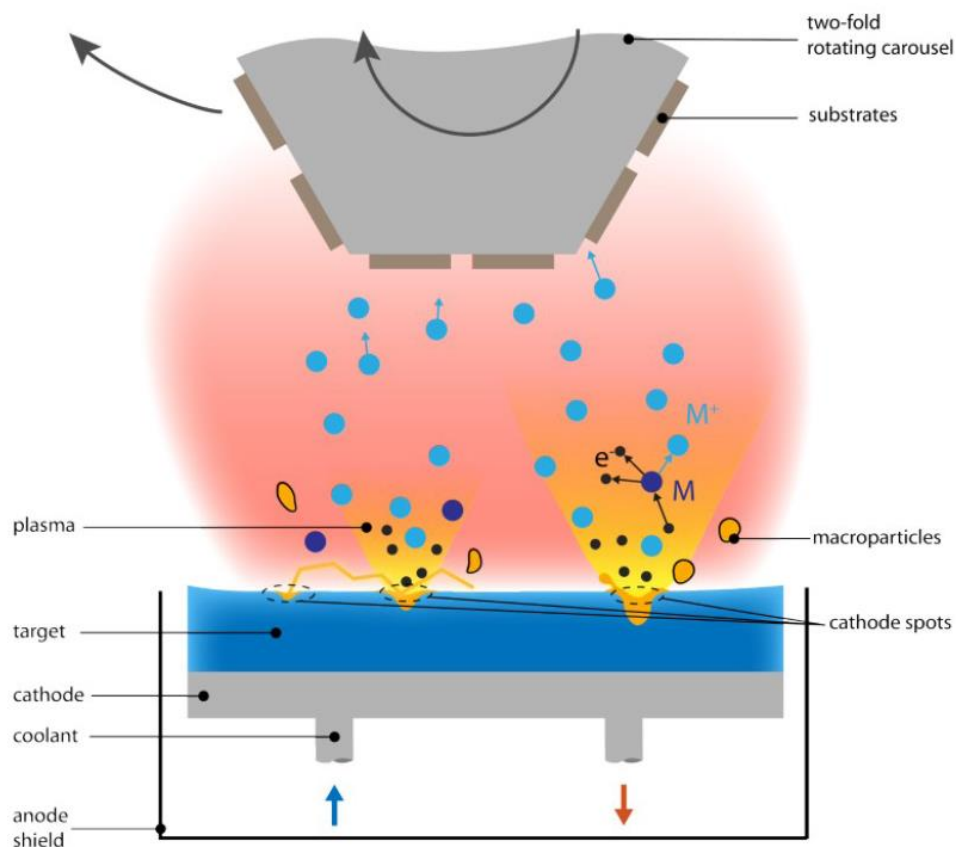
Fig. 3.2: Schematic illustration of an arc evaporation process including essential components: Target material acting as the cathode, anode, plasma (consisting of ions, neutrals and electrons), and cooling unit [22].

The evaporation process is initiated by a contact (short circuit) between a mechanical trigger and the cathode surface, resulting in a high current low voltage plasma discharge, also known as arc, at the cathode surface, that gives rise to a small, usually a few micrometres wide, highly energetic emitting area, the so called "cathodic spot". This cathode spot is active only for a couple of nanoseconds and reaches localized temperatures of about 15 000 °C, which results in a high velocity (~10 km/s) jet of vaporized cathode material, leaving a crater behind on the cathode surface [19]. Afterwards it self-extinguish and re-ignites in a new area close to the previous crater. The therefore achieved high ionisation rates mentioned above typically exceed 95 %, and are distinctively higher than competitive PVD techniques (e.g., sputtering, with ionization rates of less than 5 %). During the arc process there are several mechanism taking places (e.g., thermionic emission, thermionic-field emission, etc.), leading to favourable conditions for arc ignition in the vicinity of the active cathode spot. Moreover, the cathode spots are separated into type 1 and type 2 [19]. The latter are observed on clean metallic surfaces, leading to the above mentioned continuous path of craters of a slow moving arc and an increased generation of macroparticles, while the first one occur on surfaces covered with non-metallic layers as it is the case for reactive cathodic arc evaporation. The contamination (poisoning) of the cathode surface forming non-metallic layers (e.g., oxide or nitride layers) with the corresponding reactive gas, results in smaller separated spots moving much faster with a lower cathode erosion rate. However, the usually randomly moving cathode spots can be controlled (steered) by the presence of an external magnetic (Fig. 3.3) or electric field, resulting in decreased residence time at a certain area and hence in the formation of less and smaller macroparticles (droplets).
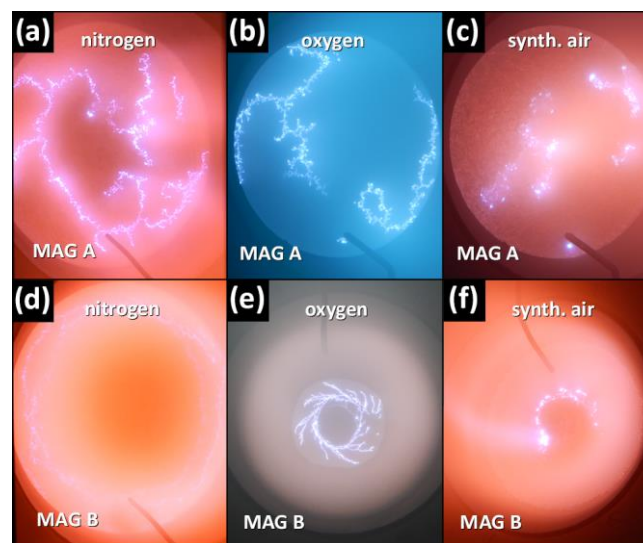
Fig. 3.3: Steered arc mode using 2 different magnetic systems and three different reactive gases.

3.3.1 Cathode & macroparticles

Besides the ionization and evaporation of the cathode material, the thermally-induced impact of arcing spots occurring on the cathode surface, results in locally melting pools of the material. The creation of these molten pools are depended by several factors such as arc spot type, arc rest time, melting point, microstructure, and grain size of the cathode material. The latter are especially relevant for compound targets. Considering an Al-Cr compound cathode material consisting of 70 at.% Al (matrix) and 30 at.% Cr, mainly used within this work, intermixing of molten distinct Al and Cr grains will take place, leading to the formation of intermetallic Al-Cr-phases [23]. The finer the grains in the cathode material, the better intermixing occurs and thus the surface is evaporated more homogenously.
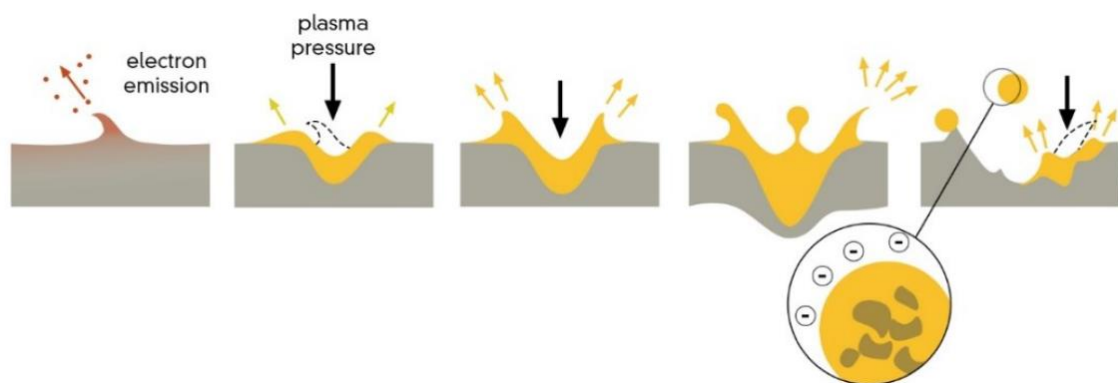
Fig. 3.4: Droplet generation due to increased plasma density above the liquid melting pool of the cathode material [8].

As a result of this localized melting process caused by an adjacent arc, the present plasma pressure pushes the melting pool radially outwards leading to the formation of molten macroparticles (droplets) emitting into the plasma in an angle usually below 45 deg., see Fig. 3.4. These droplets will also arrive at the substrate and are incorporated into the growing film. There, they will interrupt the (columnar) crystal growth, causing local shadowing effects leading to a highly puros films, see Fig. 3.5a.

This can be seen as the major disadvantage of cathodic arc evaporation, as a high amount droplets incorporated into the film might have a negative influence on mechanical (e.g., low hardness and high roughness, Fig. 3.5b) and thermal (high diffusion path ways) properties. The size (typically between couple of nanometres and some micrometres) and distribution of macroparticles is mainly affected by the cathode´s material.
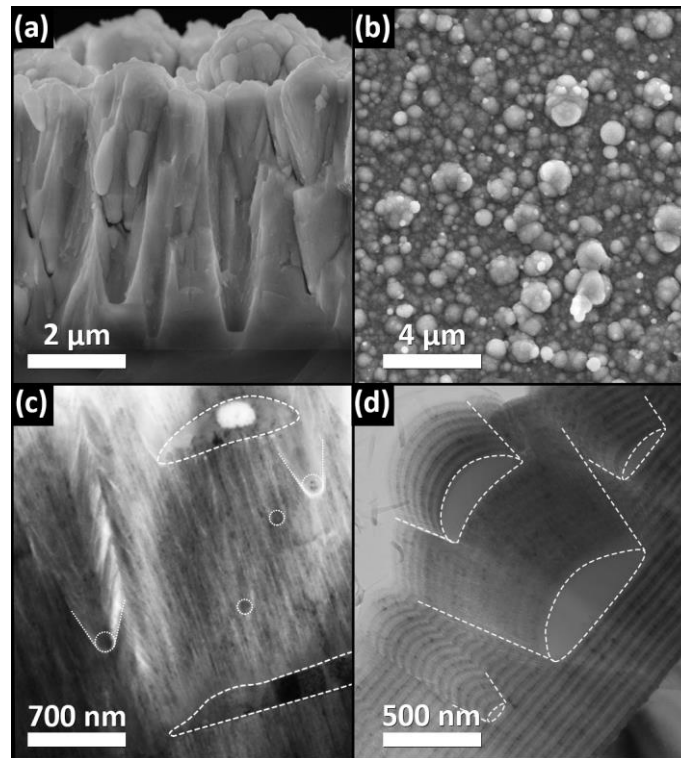
Fig. 3.5: Influence of droplet formation on (a) morphology and (b) surface (roughness) of a growing film, investigated by SEM. Different shapes of droplets, e.g. (c) spherical and (d) flat or pancake-like, observed via TEM.

However, not only the size but also the shape of the droplets can be different, see Fig. 3.5c and d, depending on the melting point of the used target material. Low melting elements such as Al are still mostly in the liquid phase when they hit the substrate leading to flat shaped (pan-cake like) droplets, while high-melting elements, such as Cr solidify during the transport between cathode and substrate leading to the incorporation of spherical macroparticles [24] and the previously mentioned growth defects.

3.4 Basics of film growth

The microstructure and morphology of a growing film are major factors in determining the properties of hard protective coatings. Therefore, a fundamental understanding of the correlation between deposition conditions and resulting film growth is necessary. Coatings with comparable chemical composition may still differ in mechanical and/or thermal properties due to variations in the crystallographic constitution, microstructure [25–28] and/or porosity (defect density) of the films. Before going into more detail of the film growing mechanism, a short excurse into the thermodynamic regarding phase stability is given.

3.4.1 Phase stability

The Gibbs free energy G is described as the thermodynamic potential of a system, which determines the stability regime of a certain phase at given conditions (i.e., temperature, pressure, and chemical composition) and is characterised by:

$$G = U + pV - TS = H - TS \tag{3.9}$$

U is the internal energy, p is the pressure, and V is the volume. They can be summarised as enthalpy H, while T describes the absolute temperature and S the entropy [10]. The equilibrium (thermodynamically stable) state which a system always strives to take exhibit the lowest Gibbs free energy (i.e., dG = 0). However, there is also the possibility for a system to reach a metastable state, where the Gibbs free energy exhibits a local minimum and thus also fulfils the condition dG=0, see Fig. 3.6. This is commonly the case for PVD synthesized coatings, where extreme cooling rates enable the growth of metastable structures [5]. Due to a thermally-induced input atoms are able to overcome the energy barrier to reach an energetically more favourable arrangement and thus a thermodynamically more stable state. This can be achieved on purpose (e.g., post deposition annealing treatments), or during the application of the coating.
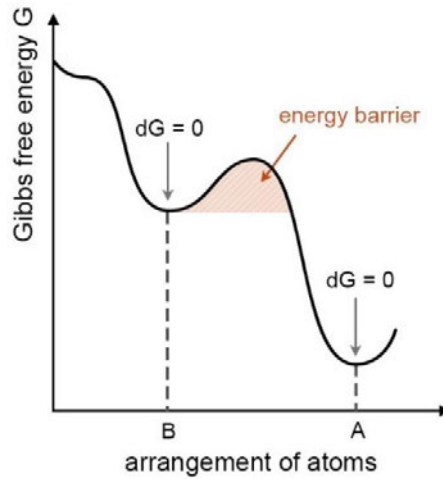
Fig. 3.6: Illustration of the Gibbs free energy G of a system with different atomic arrangements. Even though the system appears to be stable at B, it may just be a local minimum in energy with the global minimum at a different atomic arrangement A.

Hence, heat treatments of e.g. face centred cubic structured fcc-$(Al_xCr_{1-x})_2O_3$, fcc-$Al_xCr_{1-x}N$, and fcc-$Ti_{1-x}Al_xN$ coatings lead to their decomposition into their stable constituents via nucleation and growth [29–33] and spinodal decomposition [34,35], respectively.

Generally the difference in the Gibbs free energy of initial (G_1) and final (G_2) state determines if a phase transformation lead to an energetically more favourable condition ($\Delta G < 0$) [2]:

$$\Delta G = G_2 - G_1 < 0 \tag{3.10}$$

Of higher practical importance are multiple component systems, as it is the case for solid solutions consisting of different atomic species. Here, we can again define the difference between the initial and final state, described by the mixing enthalpy ΔG_{mix}:

$$\Delta G_{mix} = G_2 - G_1 < 0 \tag{3.11}$$

Whereas the corresponding enthalpy H and entropy S values can be written as

$$\Delta H_{mix} = H_2 - H_1 \tag{3.12}$$

$$\Delta S_{mix} = S_2 - S_1 \tag{3.13}$$

resulting in

$$\Delta G_{mix} = \Delta H_{mix} - T\Delta S_{mix} \tag{3.14}$$

The internal energy difference before and after the mixing can be described by the mixing enthalpy ΔH_{mix} (heat) of the solution. If energy is released during intermixing the

reactions are exothermic, whereas if energy has to be provided the reactions are endothermic.

For a binary system A-B the mixing enthalpy ΔH_{mix} defines, whether it is energetically more favourable to form chemical bonds between different atomic species A and B (H_{AB}) or between atoms of the same type (H_{AA} or H_{BB}).

$$\Delta H_{mix} = \Delta H_{AB} - \frac{1}{2}(H_{AA} + H_{BB})$$

(3.15)

However, the contribution of the intermixing entropy ΔS_{mix} is always negative and thus leading to a stabilisation of the system with increasing temperature. Accordingly, ΔH_{mix} determines whether the configuration reaches a stable or unstable regime. A summary of possible scenarios of the intermixing Gibbs free energy ΔG_{mix}, including individual ΔH_{mix} and ΔS_{mix} contributions, is shown in Fig. 3.7. A stable configuration of the compound is enabled for negative ΔH_{mix} values independent of the temperature, see Fig. 3.7a and b. For positive values, the temperature and therefore the -$T\Delta S_{mix}$ contribution determines the stability regime of the compound. At high temperatures the overall ΔG_{mix} curve can still be negative, Fig. 3.7c, whereas at low temperatures and dominating positive ΔH_{mix} values a miscibility gap can develop, Fig. 3.7d, in which a compound AB is energetically unstable. Hence, decomposition will take place in order to minimize the overall free energy of the system either by nucleation and growth or by spinodal decomposition.
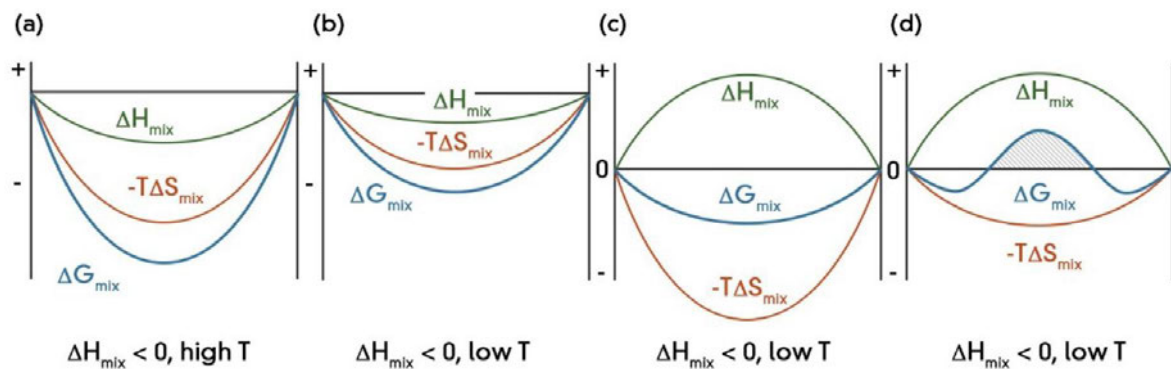
Fig. 3.7: Behaviour of ΔG_{mix} schematically illustrated for various ΔH_{mix} and $-T\Delta S_{mix}$ values. (a) and (b) negative ΔH_{mix} with high and low temperature. (c) and (d) positive ΔH_{mix} with high and low temperature, whereas a miscibility gap is present for the latter one [10].

3.4.2 Nucleation and growth

Many phase transformation in thin films and solid materials in general proceed via nucleation and subsequent growth of a nuclei. If we consider a homogeneous solid phase α then its transformation into β starts with the generation of a nuclei. Thereby, the system will follow the energetically more favourable state, where the free energy is the lowest. The formation of a nucleus can be associated with the creation of phase boundaries between α and β phases. A spherical shape of the β nucleus is considered with a surface energy γ to the surrounding α-phase. Consequently, two energy contributions to the overall energy are present [2]:

$$\Delta G_N = \Delta G_S - \Delta G = 4r^2\pi \cdot \gamma - \frac{4}{3}r^3\pi \cdot \Delta G_V \qquad (3.16)$$

Whereas ΔG_S attributes the energy cost to form a new surface, while ΔG describes the energy gain due to the formation of new, energetically favourable β phase, see Fig. 3.8. Consequentially, a newly formed β nucleus has to overcome a certain energy barrier ΔG^* (for the formation of a stable precipitation) and size quantifies by r*, the critical radius:

$$r^* = \frac{2\gamma}{\Delta G_V} \qquad (3.16)$$

Thus, as long as the nuclei are smaller than r* they are unstable and dissolve under energy gain. Only if they are larger than r* energy is gained by growth. Formation of nuclei with sizes $r > r^0$ is always energetically favoured [2].
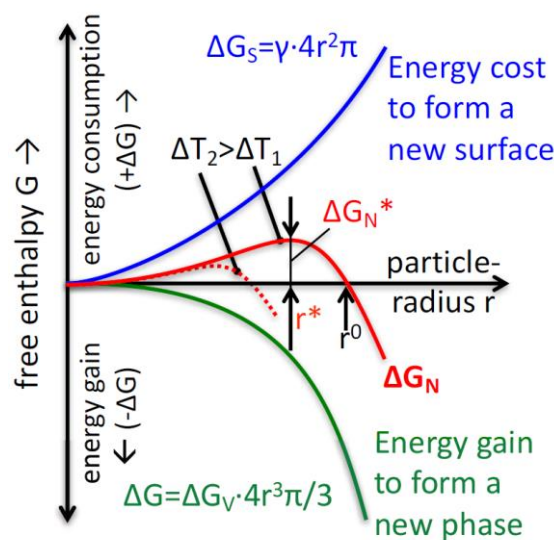
Fig. 3.8: Thermodynamics of nucleation [2].

As representatives for such mechanisms, fcc-$Al_xCr_{1-x}N$ and fcc-$(Al_xCr_{1-x})_2O_3$ are mentioned. The first one most likely decomposes into its stable compounds fcc-CrN, h-Cr_2N, and w-AlN [30,31], while the latter one transforms into α-$(Al_xCr_{1-x})_2O_3$ [29] during annealing at elevated temperatures, respectively.

Film Growth

The impact of ions or atoms from the plasma or vapour onto the surface of the substrate (e.g., tool or component) results in adsorption and thus initializing every film growth. The ongoing mechanism for nucleation can be described as combination of simultaneous adsorption, desorption, and adatom diffusion. Grain growth of film results due to the energetically preferred accumulation of the arrived ions or atoms and can be described with three different modes, see Fig. 3.9. The first one is called layer-by-layer growth described by *Frank and van der Merwe*, which occurs if the film atoms are more strongly bound to the substrate than to each other and also if the diffusion rate is high enough allowing migration along the surface of high mobile adatoms to form a thin layer. Advantageously such growth mode lead to the formation of dense films, due to the high coverage of the substrate surface which is preferred for multitude of applications. Disadvantageously layer-by-layer growth exhibits a rather low growth rate. The second mode, described by *Volmer and Weber* is called island growth, which can be seen as the opposite effect to layer-by-layer growth. During island growth the adatoms are more strongly bound to each other than to the substrate surface and thus the formed nuclei grow in three dimensions by gaining new atoms (low surface diffusion). The third mode, the mixed growth mode, is a combination of the two already mentioned growth modes described by *Stranski-Krastanov*, which is most commonly for PVD synthesised films (coatings) and can be characterised by an initially layer-by-layer growth process accompanied by the formation of three dimensional islands. This behaviour is related to the surface energy evolution during film growth.
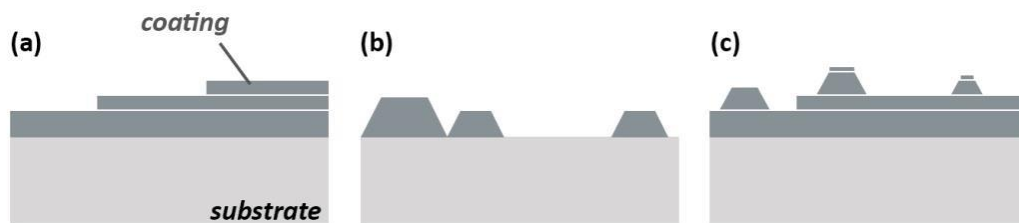
Fig. 3.9: Illustration of the three basic growth modes occurring in thin films: (a) Frank-van der Merwe, (b) Volmer-Weber, and (c) Stranski-Krastanov; from [36] originally from [18].

3.4.3 Spinodal decomposition

The understanding of the ongoing mechanism during spinodal decomposition is essential for $(Al_xCr_{1-x})_2O_3$ investigated within this work. In contrast to nucleation and growth, spinodal decomposition does not need to overcome a specific nucleation barrier [10].

PVD coatings in general are synthesised in a metastable state due to the rapidly cooling process. A initial (metastable) state of e.g. $(Al_xCr_{1-x})_2O_3$ with a certain composition x_0 can be seen as red dot in the G-x curve of Fig. 3.10. Hence, slightly chemical fluctuations will always result in an energy gain, as can be seen from the dotted line directly below the red dot. The system preferable wants to decompose towards A and B. The primary condition for spinodal decomposition is a dominating positive intermixing enthalpy ΔH_{mix} and thus the existence of a miscibility gap as well as an initial composition in which the second derivation of the Gibbs free energy is negative ($\partial^2 G/\partial x^2 < 0$), marked by dark grey shading.

Outside the spinodal area compositional variations are accompanied by an increase of energy, leading to nucleation and subsequent growth. Hence, the nucleus might differ in the chemical composition from that of the initial matrix [8].
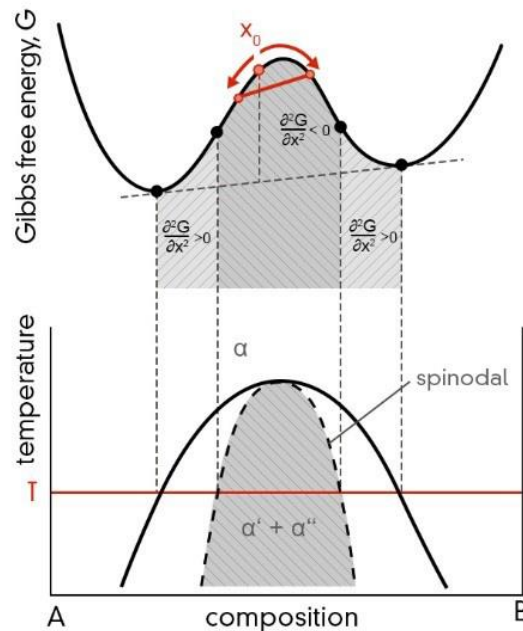
Fig. 3.10: Relation between the Gibbs free energy curve and phase diagram of a compound featuring spinodal decomposition from [8] originally after [10,37].

3.4.4 Structure Zone Model

Structure zone models (SZM) were first established by Movchan and Demchishin [38], Thornton [39] and Messier [40] in the 1960s to correlate basic deposition parameters (e.g., substrate temperature, substrate bias voltage, or gas pressure) with the developing film morphology and microstructural evolution. A further developed version of the SZM was later reported by Anders [41], see Fig. 3.11, which includes plasma based deposition and etching processes.

The three axis of the SZM can be described as follows:

- A generalised temperature, T* (x-axis), which consists of the homologous temperature (quotient of deposition temperature and melting temperature) and further depends on the temperature change caused by the potential energy of arriving particles.
- The normalised energy, E* (y-axis), which considers the energy flux in relation to the cohesive energy and the different mass ratios of the arriving particles as well as displacement and heating effects by the kinetic energy of bombarding particles.
- The film thickness, t* (z-axis), which considers "negative thickness" caused by ion etching processes.

Elevating the temperature within the deposition chamber results in an increased mobility and thus increased diffusion of atoms and ions at the substrate surface which results in the growth of dense coatings. A quite similar effect to higher the mobility of the adatoms can be achieved by an increased substrate bias voltage due to the higher energy gain of stronger attracted ions to the substrate surface. If the kinetic energy of the impinging ions, reaches a certain value, re-sputtering effects occur. Additionally if this mechanism is used to remove residuals and native oxide contaminations from the surface of the substrate the process is call substrate etching.
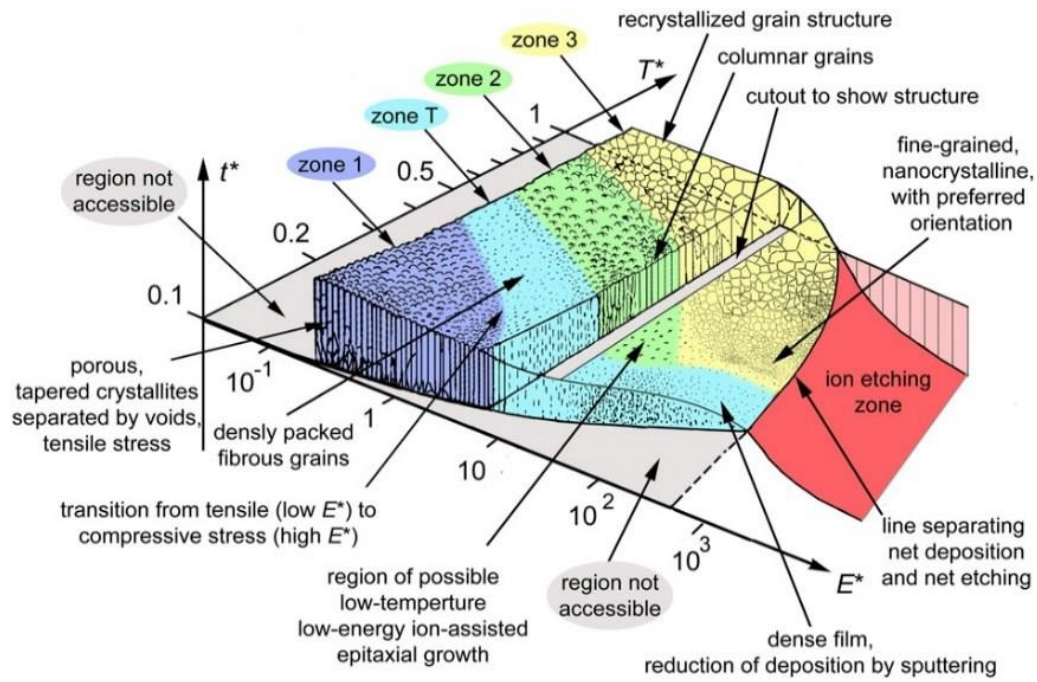
Fig. 3.11: Structure Zone Modell after Anders [41].

Another important process parameter considered in the SZM is the reactive gas or absolute chamber pressure. A high chamber pressure increases the amount of collisions and thus decreasing the mean free path of the evaporated species causing kinetic energy losses. Therefore, a low chamber pressure should be chosen in order to keep the kinetic energy of the impinging ions high enough. It should nevertheless be kept in mind that a certain pressure is required to sustain a stable plasma.

3.5 Ternary systems Al-Cr-N

The thermal stability as well as the mechanical properties of monolithically grown single-phase $Al_xCr_{1-x}N$ coatings significantly increase with increasing Al-content x [42–45]. However, the typical metastable solubility limit for Al, of the fcc phase, is around x ~0.7. Higher Al contents favour the hexagonal wurtzite structure [44,46], see Fig. 3.12. This structural transition has a substantial effect on mechanical properties, for example, the hardness decreases from ~38 GPa for single-phase fcc $Al_{0.7}Cr_{0.3}N$ to ~22 GPa for mixed and wurtzite-structured $Al_xCr_{1-x}N$ with higher Al contents [46]. Generally, excellent mechanical properties ask for the fcc phase, but excellent thermal stabilities ask for high Al contents [30,31,47]. The combination of both (fcc phase and high Al content) drives research towards the development of coatings with Al-contents as close as possible to the fcc solubility limit x ~0.7. A denser film morphology with favourable residual stress states can be obtained by adequate substrate biasing, as shown by Sabitzer et al. [48] for monolithically grown and multi-layered $Al_xCr_{1-x}N$ films. This study furthermore shows that the growth of the hexagonal wurtzite-type phase can be suppressed by a high ion bombardment even for high Al-containing layers (up to x ~0.77). The superior oxidation resistance observed for these films is based on the formation of protective Al_2O_3 and Cr_2O_3 scales at the coating surface. Following their initial formation, an effectively retarded material consumption is observed, even at elevated temperatures of 900 – 1100 °C and prolonged annealing times of 30 – 90 min [49,50].
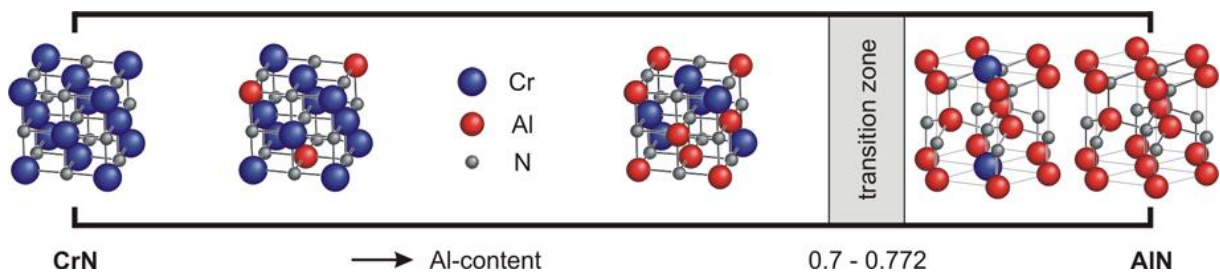
Fig. 3.12: Influence Structural development of the pseudo-binary system for transition metal aluminum nitride (TM1-xAlxN) systems with increasing AlN content exemplarily shown for the CrN-AlN system [51].

Synthesis conditions in PVD and particularly CAE trigger the growth of supersaturated metastable coatings which are subject to thermally-induced decomposition processes. For monolithically grown and multi-layered $Al_xCr_{1-x}N$ coatings it is known that fcc-$Al_xCr_{1-x}N$ decomposes into w-AlN and body centred cubic (bcc) Cr with the intermediate formation of hexagonal (h) Cr_2N via the release of nitrogen [30,31,33,52]. Such phase transitions, especially when related to large volume changes and mass losses, significantly degrade the coating performance and its initiation should be retarded beyond the maximum application temperature.

3.6 Ternary systems Al-Cr-O

Replacing nitrogen by oxygen leads to entirely different material properties within the Al-Cr-system, exhibiting even higher thermal stability and resistance in oxidising environments. Corundum-type Al_2O_3 coatings deposited onto machining tools by chemical vapour deposition for instance, significantly enhance the tool-performance and life time due to excellent wear protection, high hot hardness, and stability of Al_2O_3 at elevated temperatures [53]. The synthesis of the stable corundum-type Al_2O_3 by PVD is still challenging and the topic of many research activities [21,29,54,55]. At growth temperatures below 600 °C many various transient metastable Al_2O_3 modifications develop. The formation of $(Al,Cr)_2O_3$ solid solutions has thus attracted attention as a promising alternative, because Cr_2O_3 helps to stabilize the corundum type structure [20,21], see Fig. 3.13.
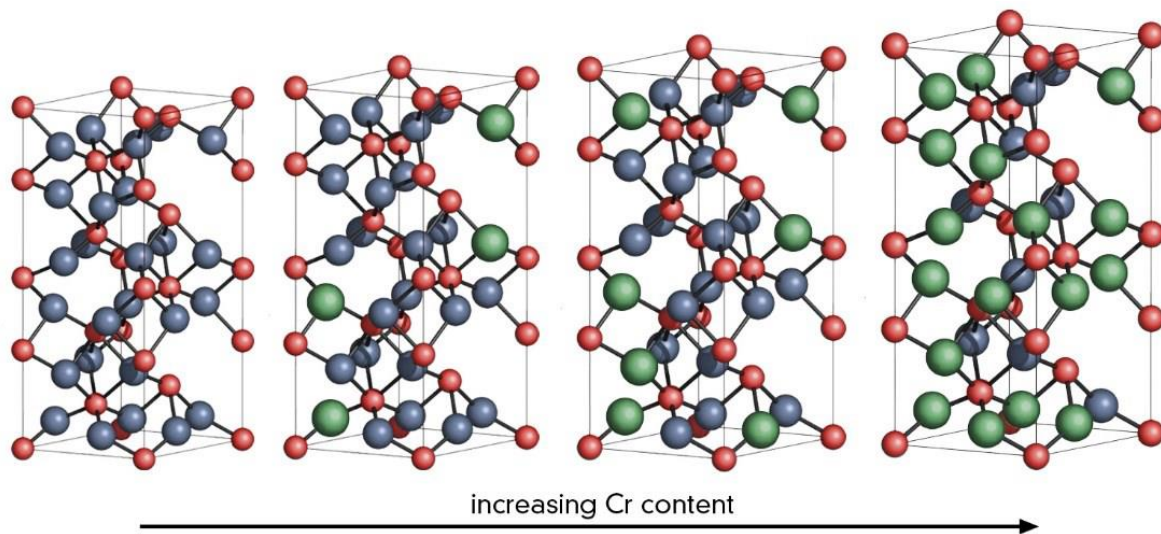
Fig. 3.13: Influence Schematic illustration of Cr (green spheres) substituting Al (blue spheres) on the metallic sublattice in Al_2O_3 leading to the formation of a hexagonal solid solution $(Al_{1-x}Cr_x)_2O_3$ taken from [8], originally from [56].

Even though Al_2O_3 and Cr_2O_3 are, thermodynamically, not miscible at temperatures below 1200 °C [57] (i.e., ~1500 K for the relevant Al-Cr-ratio of 70/30, see Fig. 3.14), the synthesis conditions of PVD in general, and CAE in particular, favour the formation of metastable $(Al_xCr_{1-x})_2O_3$ films. Here again, the Al content strongly determines the attainable phase constitution and microstructure (in fact more than in the case of nitrides).
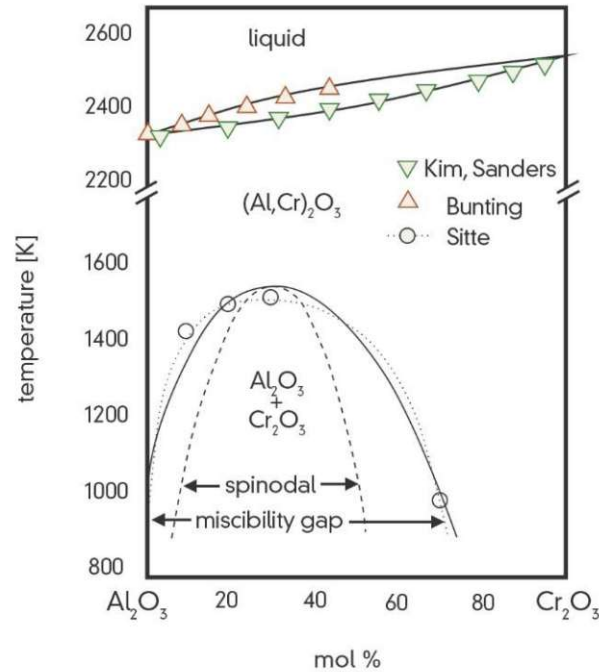
Fig. 3.14: Quasi-binary phase diagram of Al_2O_3 and Cr_2O_3 taken from [8], originally from [58].

For cathodic arc evaporation an at least two-phased composition is reported, consisting of the hexagonal corundum-type structured solid solution α-$(Al,Cr)_2O_3$ and a metastable face-centred cubic [20,21,59–63] and/or a γ-type $(Al,Cr)_2O_3$. Higher Al contents in general favour the formation of fcc structured films rather than the desired corundum type ones. Their metastable nature implies a thermally-induced phase transformation into the hexagonal corundum type structure if exposed to elevated temperatures for which the tool or component likely suffers during application. The therewith associated volume reduction induces significant tensile stresses to the material, leading to crack initiation and failure of the coating [64].

3.7 Quaternary systems Al-Cr-O-N

Combining oxides and nitrides within the PVD process, generally leads to the formation of Al-Cr-based oxynitride films. Owing to their special character, they have gained enormous interest in recent years [61,65–68]. In order to understand their performance, it is important to consider several peculiarities, due to the ionic and covalent bonding contributions. To retain the average charge neutrality, the formation of anion or cation vacancies, or anion or cation interstitials is inevitable ($2N^{3-} = 3O^{2-}$), see Fig. 3.15.
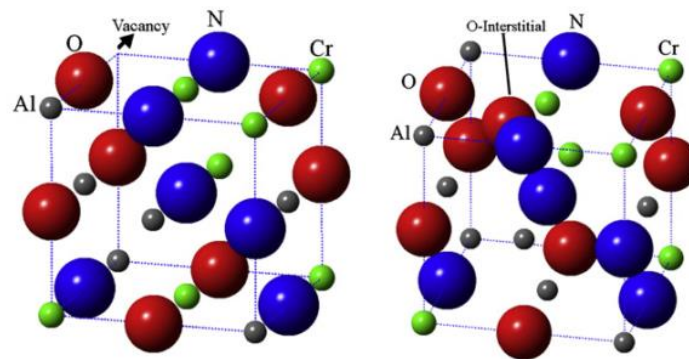
Fig. 3.15: Unit cells of a) cubic oxynitride with insertion of metal vacancy b) cubic oxynitride with insertion of interstitial anion [67].

A detailed study on the impact of such vacancies and interstitials (also in combination to form Schottky and Frenkel pairs) on the phase formation of alloyed $(Al_xCr_{1-x})_2O_3$ have been studied by Koller et al. [69]. Najafi et al. [67], for instance, reported that the substitution of nitrogen by oxygen leads to a decrease of the cubic lattice parameter a, attributing this effect to the formation of a $AlCr(O_xN_{1-x})$ solid solution with vacancies on the metallic sublattice. The stability regime of the single-phase fcc-structured solid solution is reported to be between 60 and 97 at.% oxygen (of the non-metal sublattice). The incorporation of more than 60 at.% oxygen at the non-metal sublattice leads to a hardness decrease from approximately 31.5±1.5 to 25.5±1 GPa due to changes in primary bonding contributions [70]. Due to the high activity of oxygen with the metallic species, a certain threshold value of nitrogen is required to establish chemically balanced oxynitride films. Based on the lower reactivity between N_2 and metallic species (e.g., Al and Cr) than between O_2 and metallic species, oxynitrides even form with relatively high N_2 contents (or low O_2 contents) of the reactive N_2+O_2 gas atmosphere. Khatibi et al. [71] prepared Al-Cr-oxynitrides with N_2/O_2 gas flow ratios of up to 9.

3.8 Multilayer arrangements

The formation of architecturally designed coatings, such as multilayers or superlattices, is a well-accepted and convenient method to improve their properties of particular interest. In general, an alternating layer arrangement of two different materials results in interactions of dislocations with the interfaces between the layers. These furthermore influence microstructural features such as grain and column boundaries, as well as various defects (especially macroparticles, like droplets in CAE) and coherency strains between the individual layers [72–74]. A key factor determining the attainable coating properties is the thickness of the individual layers – hence, the interface fraction related to the overall coating volume. By reducing the bilayer period to several nanometers, even structurally different materials can be forced to form coherent (or at least semi-coherent) interfaces through epitaxial growth. Thereby, thermodynamically metastable structures can be promoted over their thermodynamically stable ones [75]. The minimisation of the interfacial energy can be seen as the driving force behind the epitaxial stabilization effect through coherency strains [74].

Such coating designs have been realized for various nitride, carbide, and mixed nitride/carbide multilayer systems [76,77]. For example within TiN/AlN [78,79] and CrN/AlN [80] superlattice structures, the metastable face centred cubic (fcc) AlN phase (B1, NaCl-type) is stabilized through coherency with the fcc structured TiN and CrN layers. The thermodynamically stable phase of AlN is hexagonal (B4, wurtzite-ZnS type). Apart from structural stabilisation effects and associated self-healing capabilities [81], also improved thermo-mechanical properties have been realized for different material combinations [82–84]. Improved hardness (hence the materials behaviour against mechanical loading), for example, is mainly based on the interaction between dislocation-formation and -glide with layer-thicknesses and interface fraction as well as interface geometries (coherent, incoherent, gradient, etc.) [32].

CHAPTER **4**

4. Characterization techniques

Structural, compositional, mechanical, and thermal properties were investigated to characterize the coatings of this thesis. Each method is described in the following sections.

4.1   X-Ray diffraction

XRD is a common non-destructive characterization technique to investigate the crystallographic constitution of coatings (or thin films). It is based on the diffraction of electromagnetic waves (X-rays) on periodically arranged atoms in a crystal. The short wavelength of X-rays (in the order of atomic distances), allows for the investigation of materials in the atomic scale. Hence, when a focused X-ray beam is directed at a solid material, one part of the radiation is scattered. Due to elastic interactions with the outermost electrons of the atoms in the sample. Within the diffracted beam path, either constructive or destructive interference occurs, which results in an increased or decreased X-ray intensity profile as a function of the incident angle. Fig. 4.1 shows that two (monochromatic and coherent) waves which are diffracted at parallel lattice planes, can only be in phase, if the path difference is a multiple integer of the wavelength. The mathematical impression is referred to as the Bragg equation [1]:

$$n\lambda = 2\,d_{hkl}\sin\theta \tag{4.1}$$

λ is the wavelength of the incident X-rays (typically CuK$_\alpha$ radiation with a wavelength of 1.54 Å), θ is the angle of the incident X-ray beam, and n is the order of diffraction (n=1, 2, 3, …). The distance d_{hkl} between neighbouring parallel lattice planes is a function of the miller indices (h, k, and l) and the lattice parameter a. The following relationship between a and d_{hkl} is given for cubic crystal systems:

$$d_{hkl} = \frac{a}{\sqrt{h^2+k^2+l^2}} \tag{4.2}$$

Bragg´s law (equ. 4.1) is a necessary but not a sufficient condition for the diffraction on real crystals. It determines the appearance of diffraction patterns in the case that the atoms are just positioned at the edges of a unit cell. However, atoms at other positions - such as, for example, on boundary surfaces and in the centre of the unit cells in the case of face centred or body centred cubic structures, respectively - act as additional scattering centres which can lead to destructive interference at certain Bragg angles. As a result, some of the scattered beams predicted by Bragg´s law are not observed. For body centred cubic crystal structures, for example, the sum h + k + l must be even-numbered so that diffraction can be observed. On the other hand, all indices must be even or odd for face centred cubic structures.
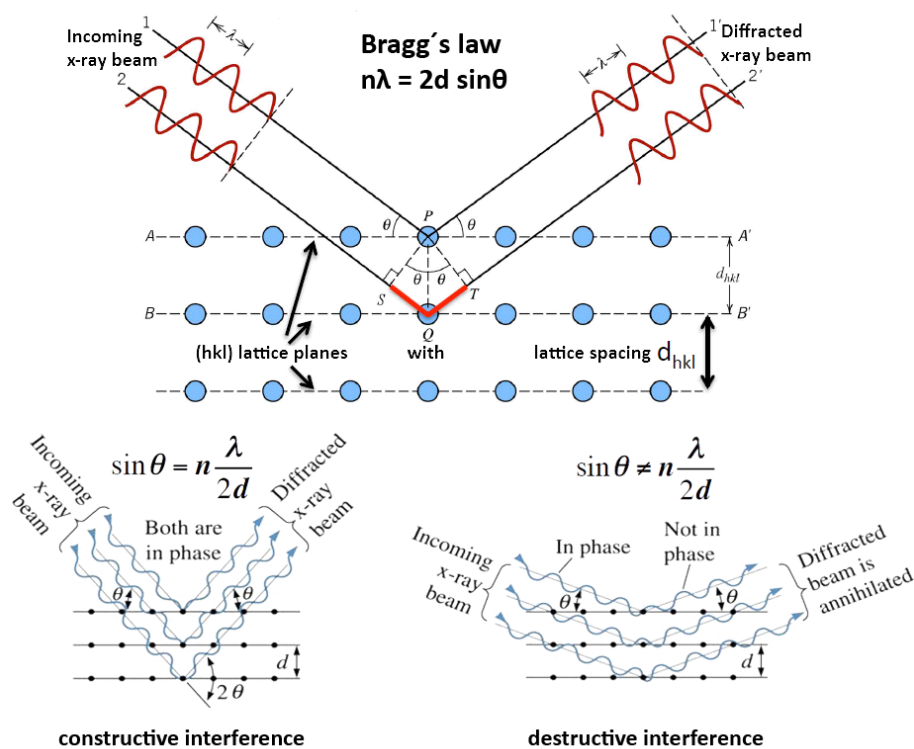
Fig. 4.1: Diffraction of X-rays at a lattice and the two resulting interference possibilities [2].

XRD investigations within this thesis were in principle arranged in the Bragg Brentano BB (θ/2θ) and Grazing Incident GI configuration, see Fig. 4.2, using the Cu K$_\alpha$ (λ≈ 1.54 Å) as a monochromatic and coherent X-ray source. In the symmetric BB scans, the incoming and diffracted angle of the beams are equal with respect to the film surface. Therefore, the scattering vector K is normal to the film surface, which means that only lattice planes parallel to the surface can be detected. In the GI configuration the angle between incoming beam and the surface (Ω typically 2°) is not equal to the diffracted beam. Therefore, the scattering vector K changes its orientation during the

measurement, which allows the investigation of crystallographic planes not parallel to the sample surface.
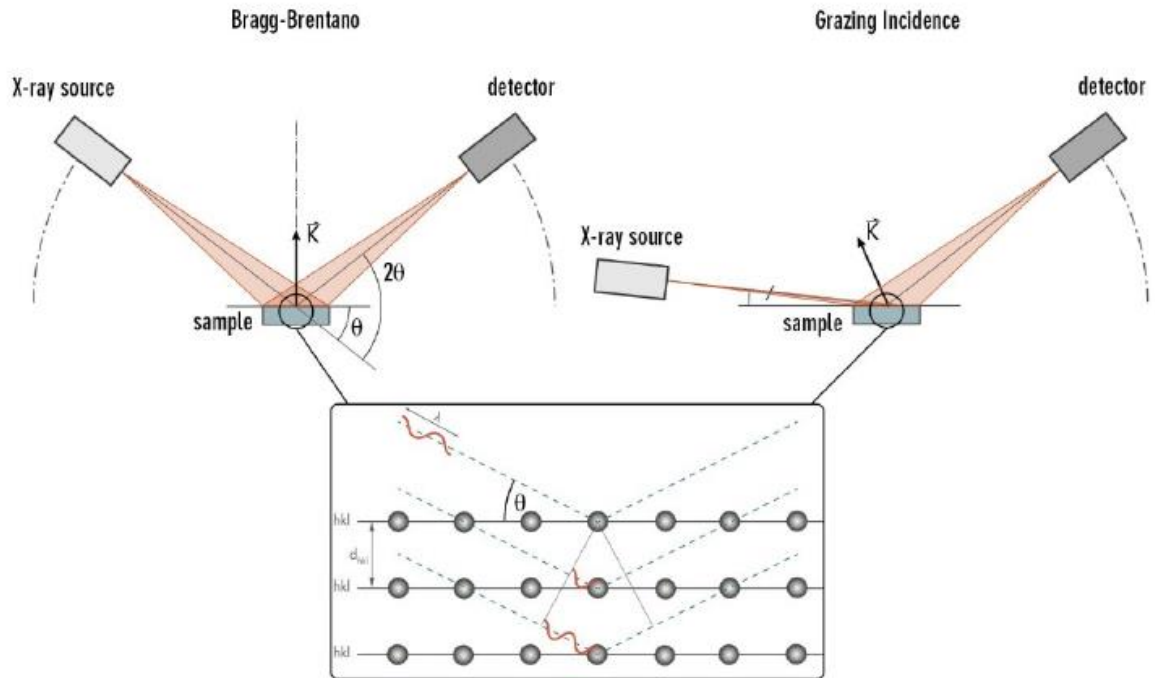
Fig. 4.2: Illustration of the two XRD arrangements used in this study: Bragg-Brentano in which source and detected rotate about the sample position and Grazing Incidence with a fixed source and adjustable detector position, from [8].

4.2 Scanning electron microscopy

In a scanning electron microscope SEM, electrons are either emitted from an electron gun by thermionic means, through an external electrical field (field emission gun, FEG), or a Schottky-type emitter (which is a thermally assisted FEG SEM), respectively. This beam is focused and screened over a defined sample area through a set of magnetic and electrostatic lenses. Thereby, the incident electrons interact with atoms in the sample, producing various signals that contain information about the sample's surface topography and composition, see Fig. 4.3. The energy exchange between the electron beam and the sample results in the reflection of high-energy electrons by elastic scattering, emission of secondary electrons by inelastic scattering and the emission of electromagnetic radiation. Each of these events can be detected by specific detectors. Generally, for imaging purpose, the back scattered electrons (BSE) as well as the secondary electrons (SE) are used, which in turn is pictured by an image enhancement system. The energy dispersive X-ray spectroscopy (EDS), for instances, is gathering the chemical information of the investigated matter by monitoring the emitted characteristic X-ray spectrum.
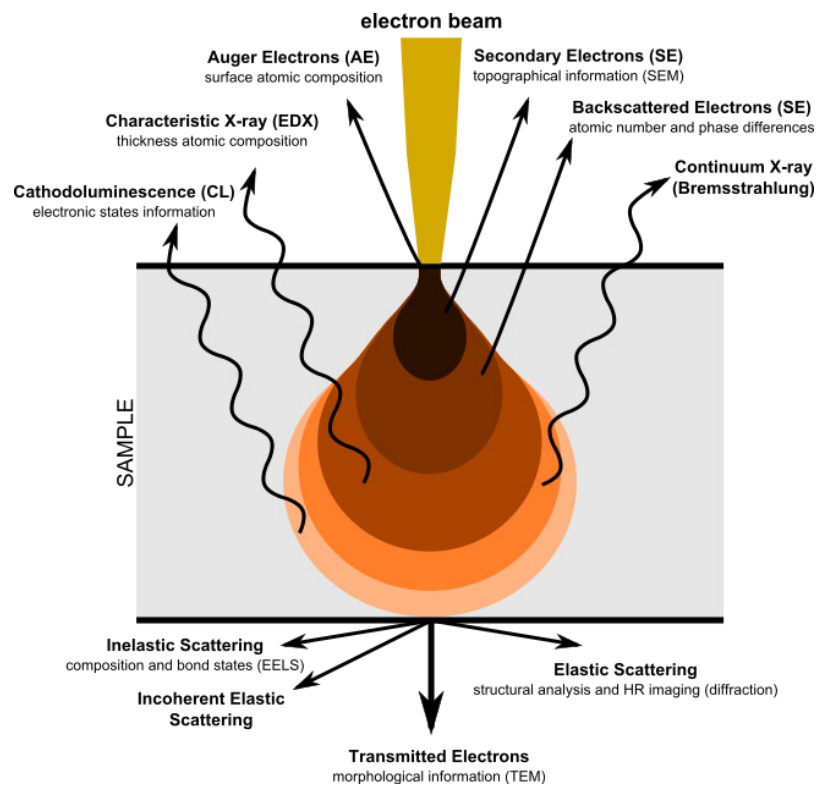
Fig. 4.3: Schematic illustration of events generated in a sample by the incident electron beam [85].

The detected secondary electrons (SE) originate from the surface near region of the investigated sample. Thus, the SE can be used to investigate surface topographies. This is typically used via top view and cross-sectional images of PVD coatings to gain information about for instance their surface constitution (roughness), morphology, thickness, and bilayer periods (in case of multilayers) if resolvable, otherwise TEM is necessary, see Fig. 4.4 and Fig. 4.5.
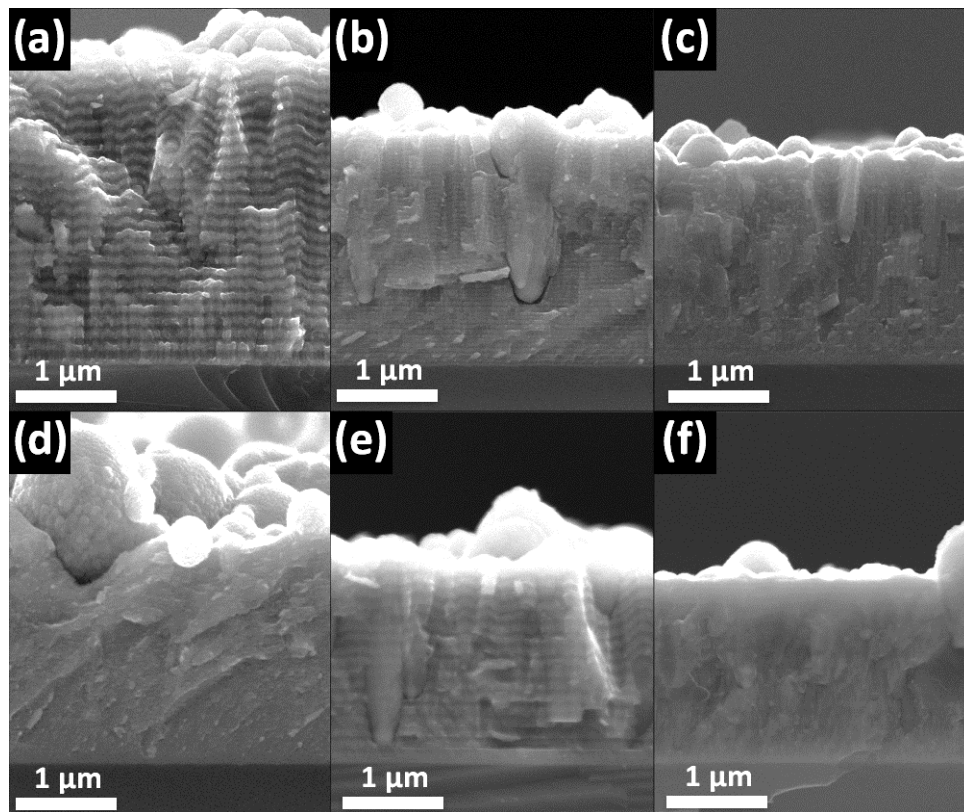
Fig. 4.4: Cross-sectional SEM images of $Al_xCr_{1-x}N/(Al_xCr_{1-x})_2O_3$ multilayers with (a) 12, (b) 25, (c)-(d) 50, (e) 80, bilayers and (f) $Al_xCr_{1-x}N/(Al_xCr_{1-x})(O_{1-y}N_y)$ multilayer coating with 75 bilayers; deposited with different reactive gas configurations.

4.3 Transmission electron microscopy

Investigating the structure as well as the chemical composition of nanometre-sized materials is the major task of a transmission electron microscope TEM, see Fig. 4.5. Compared to a SEM, in which the surface of a sample is screened by an electron beam, electrons are used to pass through a very thin specimen, during which different electron-matter-interaction processes occur. Consequently, the investigated sample has to be transparent to electrons. This means the sample thickness has to be less than hundred nanometres, depending on the material investigated, information that one is interested in, and the microscope used. A cross sectional scheme of a typical analytical transmission electron microscope AEM can be seen in Fig. 4.6. Electrons are emitted by a cathode (thermionically induced or through field emission), accelerated to 200 keV and focused on the preparation plane by a set of condenser-lenses. Further on an objective lens system creates a slightly bigger intermediate image, which is magnified by the subsequently lenses (diffraction, intermediate, projector, respectively) and can then be viewed on the screen. Alternatively, for structural information, the diffraction pattern of the specimen (lying behind the focal plane of the objective) can also be imaged. High resolution electron microscopy (HR-TEM) enables an atomic imaging of specimen details, such as lattice planes or two-dimensional defects, see Fig. 4.5d.
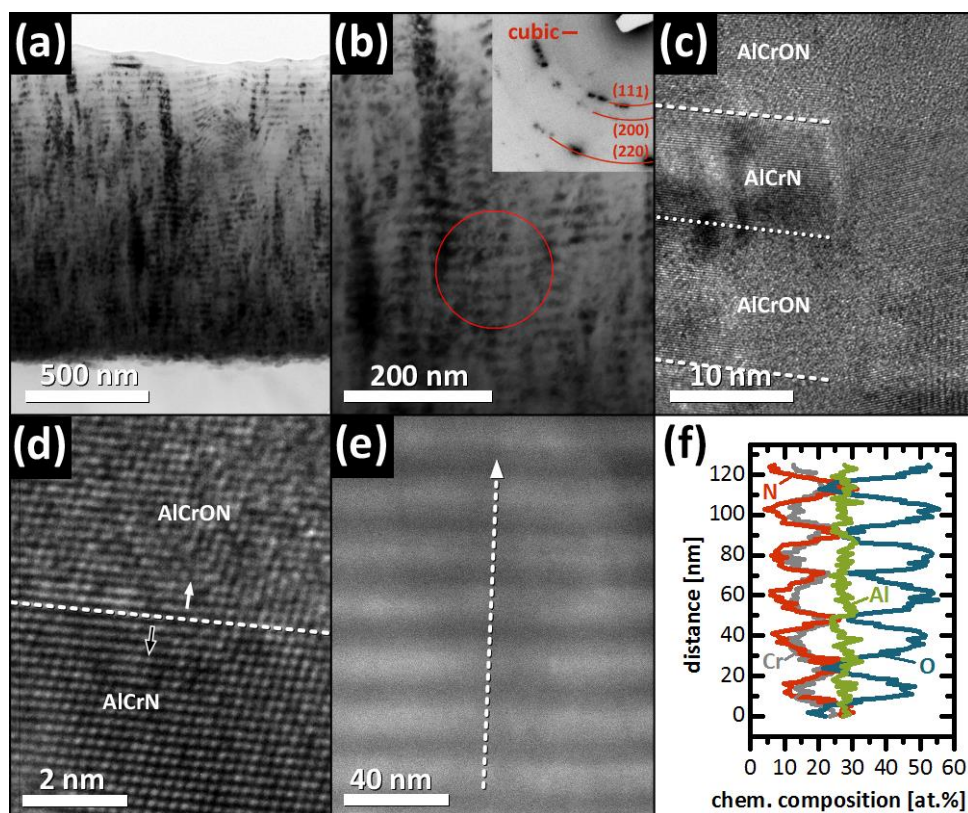
Fig. 4.5: Cross-sectional images of $Al_xCr_{1-x}N/(Al_xCr_{1-x})(O_{1-y}N_y)$ multilayers with 75 bilayers investigated with different TEM operation modes (a) BF-TEM overview of the coating, (b) BF-TEM with SAED, (c)-(d) HR-TEM, (e) STEM+EDS-line scan, and (f) resulting chemical composition obtained by (e).

Electron gun
Anode
Gun alignment coils
Gun valve
1st Condenser lens
2nd Condenser lens
Beam deflection coils
Condenser 2 aperture
CompuStage goniometer
TWIN objective lens
Specimen holder
Diffraction lens
SAD aperture
Intermediate lens
1st Projector lens
2nd Projector lens
Differential pumping aperture
Column valve
Binoculars
35mm / TV camera position
Plate camera
Focussing screen
160mm Main screen

Ion Getter Pump

Cryoblade
Specimen holder

Fig. 4.6: (a) Cross section of an analytical TEM [86].

In the common TEM (imaging or diffraction) mode, see Fig. 4.7, mainly elastic scattered electrons are involved, while for analytical purpose inelastic interactions between the primary electrons with the sample are important, see Fig. 4.3. These interactions can be used either directly via a measurement of the energy loss of the primary electrons (electron energy loss spectrometry, EELS) or via a secondary process due to a transition of an ionized atom to its ground state (energy dispersive X-ray spectroscopy, EDS). These methods are used for the site-resolved determination of the chemical composition qualitatively and quantitatively. An exact analysis of the electron spectrum allows to obtain detailed insights into the electronic structure of a solid solution, such as type of bindings. Another powerful method for investigations on structural and chemical properties, very small sample areas (typical a few tens of nanometres) is offered by scanning transmission electron microscopy (STEM), in combination with EELS and EDS.
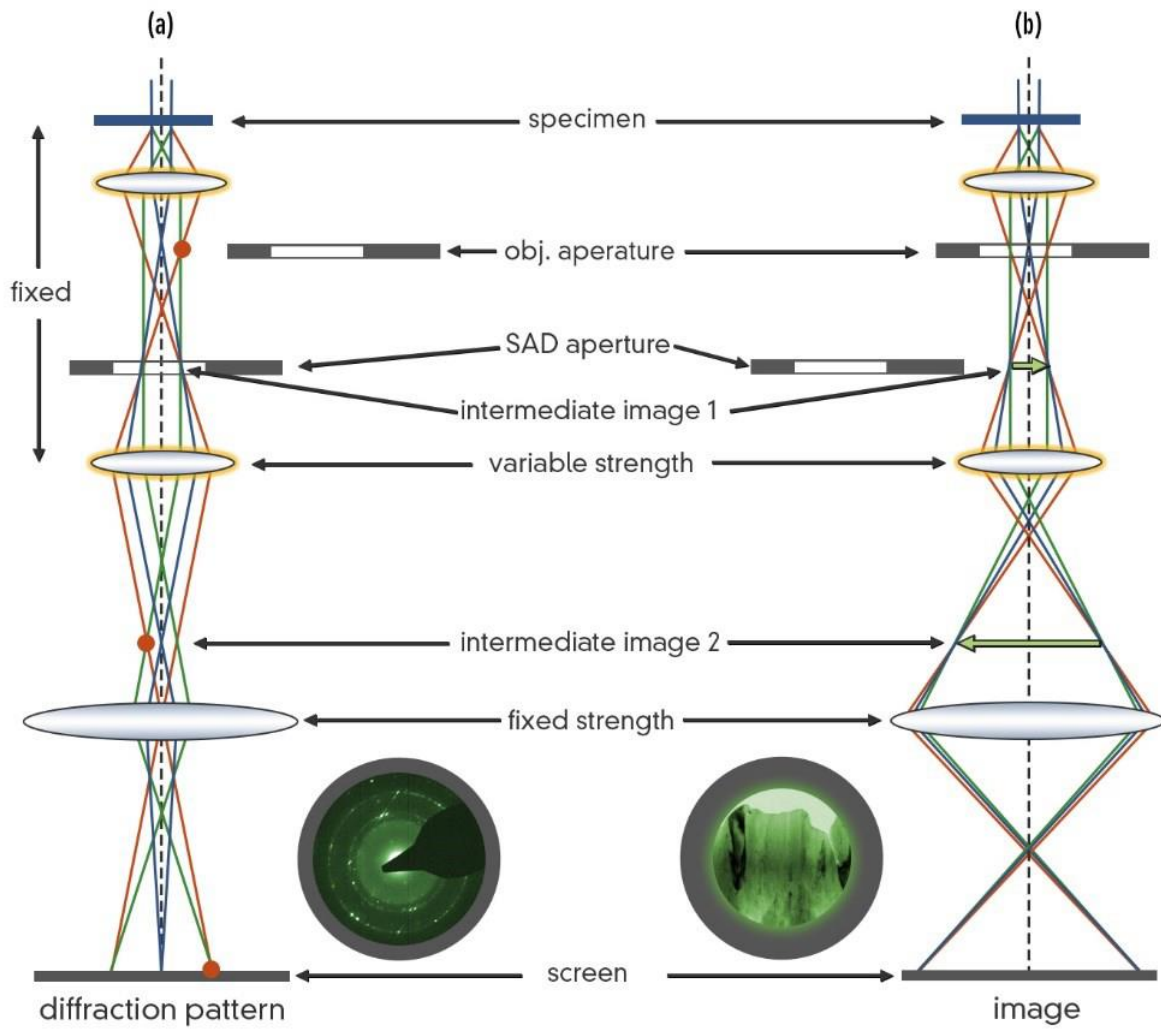
Fig. 4.7: Illustration of the two basic TEM modes: (a) electron diffraction and (b) bright field imaging [8], originally from [87].

4.3.1 Bright-Field BF and Dark-Field DF Imaging

The difference in contrast detected at the screen is mainly due to the difference in crystallographic composition, thickness, and to a certain extent also the elemental mass of the sample investigated. Electrons are scattered elastically and inelastic when they penetrate the material. With increasing sample thickness and/or increasing mass of the scattering centres (atoms), more electrons scatter to higher angles. Since a TEM is operating in a small angular range, sample areas with high thickness or heavy atoms appear much darker. In addition to the mass-thickness contrast, the diffraction contrast also occurs in the image of crystalline specimens. The incident electron beam is diffracted at suitably oriented lattice planes of the crystal lattice, whereby the transmitted electron beam loses intensity. The position of the objective aperture selected in the diffraction pattern, determines which electrons contribute to the image. If the diffracted beams are blocked, only the direct beam contributes to the image, hence the TEM operates in the bright field (BF) mode, see Fig. 4.8a and Fig. 4.9. In the dark field (DF) mode, the diffracted beam is projected and the direct beam is blocked by the aperture. For the selection of the electrons, the aperture can be correspondingly shifted ("dirty" dark field, DDF or off-axial dark field, see Fig. 4.8b and Fig. 4.10) or the diffraction pattern is shifted by tilting the incident electron beam ("classical" dark field, or axial dark field, see Fig. 4.8c).
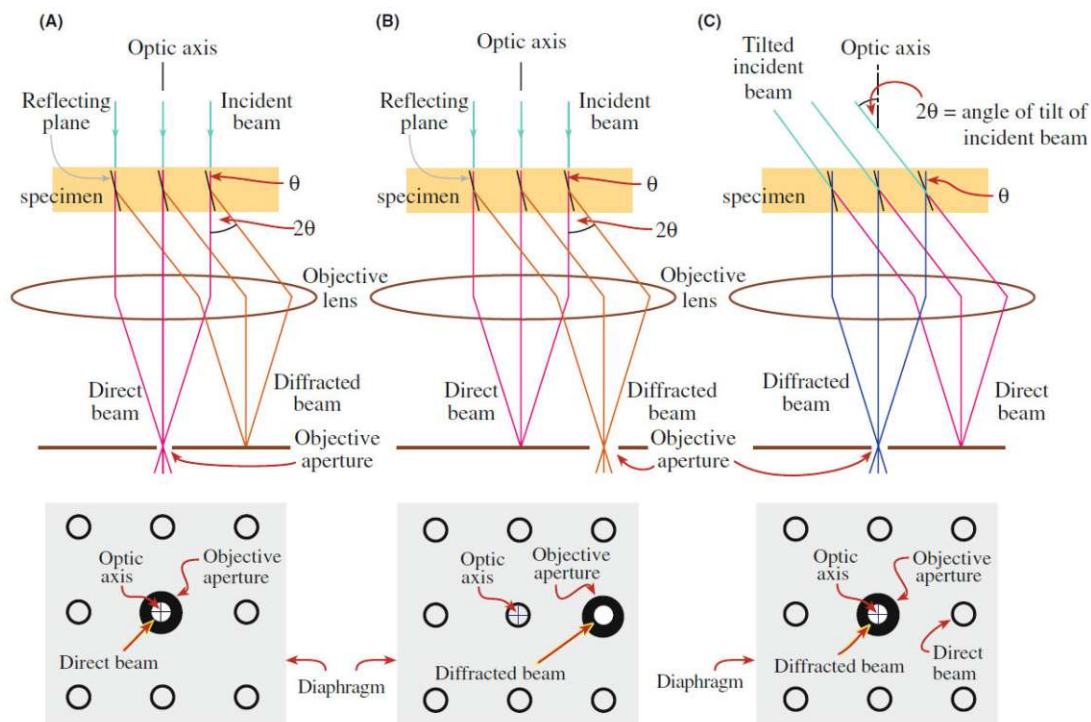
Fig. 4.8: Ray diagrams showing how the objective lens and objective aperture are used in combination to produce (A) a BF image formed from the direct electron beam, (B) a displaced-aperture DF image formed with a specific off-axis scattered beam, and (C) a CDF image where the incident beam is tilted so that the scattered beam emerges on the optic axis. The area of the DP selected by the objective aperture, as seen on the viewing screen, is shown below each ray diagram [87].
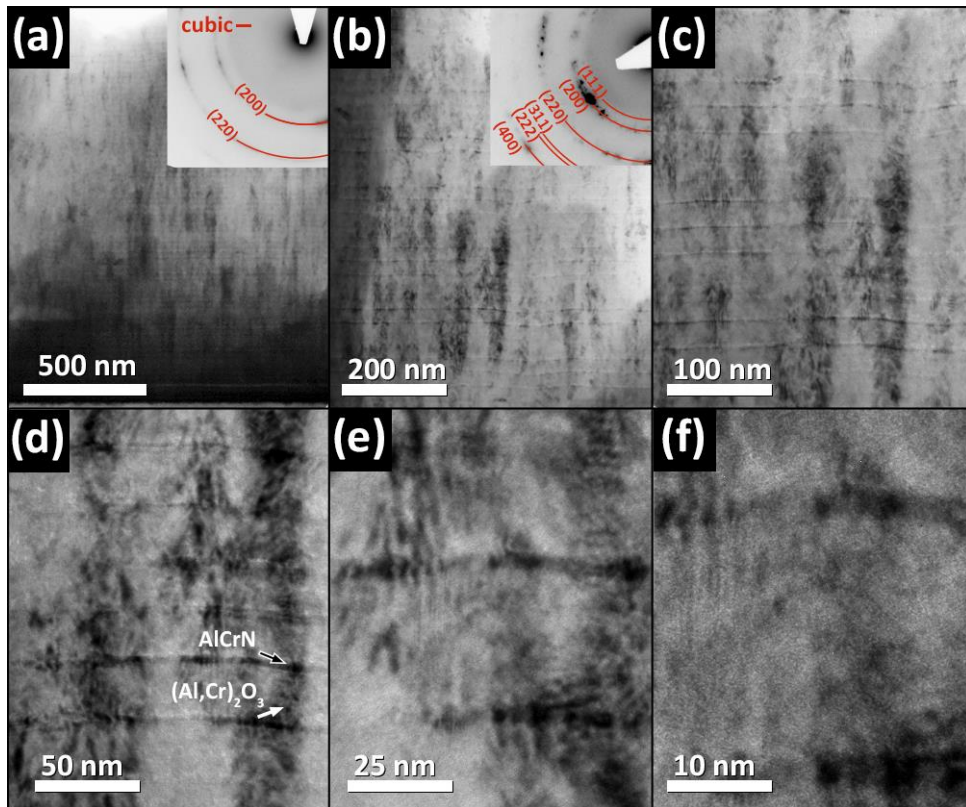
Fig. 4.9: Cross-sectional TEM bright field images of $Al_xCr_{1-x}N/(Al_xCr_{1-x})_2O_3$ multilayers with 80 bilayers investigated with increasing order of magnitude from (a) to (f) to demonstrate the individual layers and partial epitaxy growth (vertical dark features).
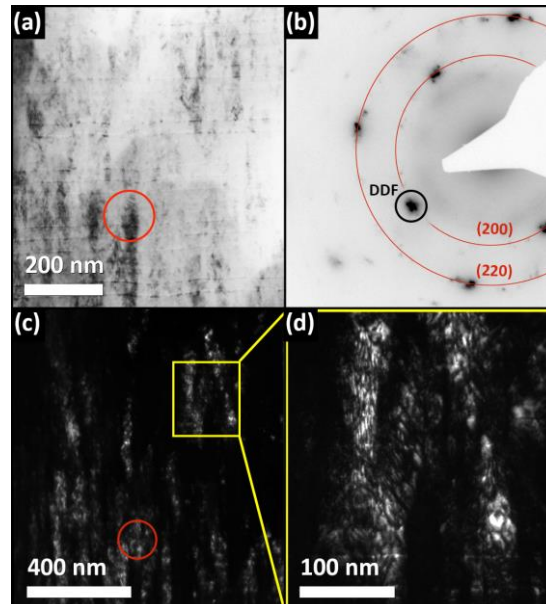
Fig. 4.10: Cross-sectional TEM (a) bright field, (b) SAED, and (c)-(d) dirty dark field images of $Al_xCr_{1-x}N/(Al_xCr_{1-x})_2O_3$ multilayers with 80 bilayers. The vertical dark features in BF-mode, which indicate partial epitaxy growth appear as vertical bright features in the DDF-mode.

4.3.2 Scanning transmission electron microscopy

Under the already mentioned imaging conditions in the TEM, a more or less large sample area is always irradiated at the same time. In scanning transmission electron microscopy STEM, the electron beam is focused and scanned across the sample, like in a SEM, while the signal of the transmitted and diffracted electrons is collected on a bright field and dark field detector, respectively, see Fig. 4.11. For imaging purpose the STEM BF mode monitored the transmitted electrons, while the STEM DF mode visualize elastically scattered electrons. STEM is also used for several types of analytic investigations, such as EDXS and EELS, where a high spatial resolution is required, see Fig. 4.12.
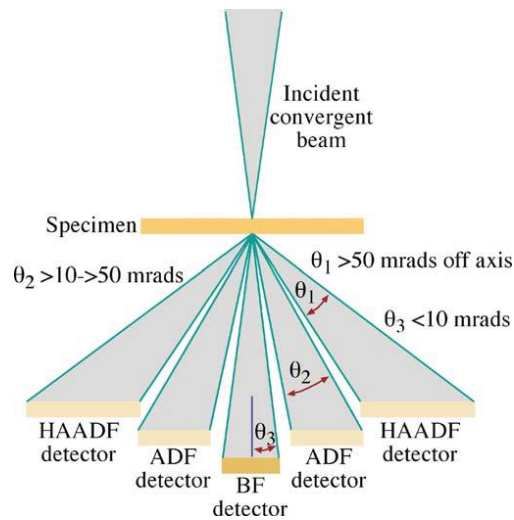
Fig. 4.11: Schematic of the HAADF detector setup for Z-contrast imaging in a STEM. The conventional ADF and BF detectors are also shown along with the range of electron scattering angles gathered by each detector [87].
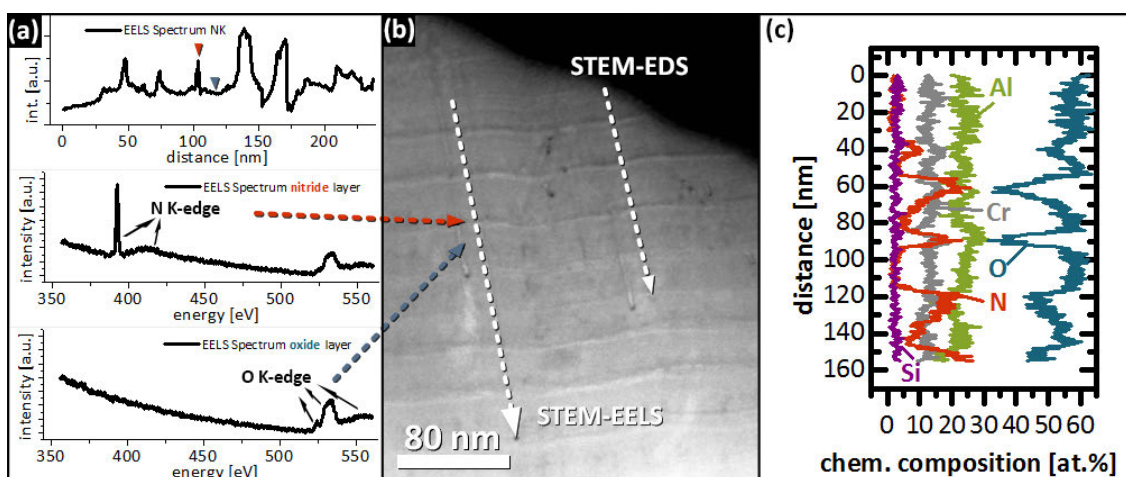
Fig. 4.12: Analytical investigations (a) EELS and (c) EDS obtained from line scans of $Al_xCr_{1-x}N/(Al_xCr_{1-x})_2O_3$ multilayers imaged in (b) STEM-BF mode.

4.3.3 Electron dispersive X-ray spectroscopy

While the elastic interaction of the electrons with the sample is crucial for diffraction, the electron dispersive X-ray spectroscopy evaluates X-ray radiation, which is produced by inelastic interaction. The incident electrons collide with the inner shell electrons of the sample atoms. This lead to a kinetic energy transfer which is sufficient enough for the inner shell electrons to leave the system. The electrons which are now missing are occupied by electrons from energetically higher shells, whereby characteristic X-rays (as well as Auger electrons) are emitted. This radiation is detected energy-dispersive and its intensity is plotted as a function of the energy. With this technique it is possible to analyse the chemical composition of sample regions much smaller than during SEM EDS, see Fig. 4.12c. Moreover, by directing the electron beam along a line or a two-dimensional area, additional and more complex information can be obtained.

4.3.4 Electron energy-loss spectrometry

Electron energy-loss spectrometry (EELS) is the analysis of the modified kinetic energy of the electrons after interaction with the sample material. These energy-loss events can be used to determine the chemical and electronic structure of the specimen atoms, which in turn reveals details of their bonding state, the nearest-neighbour atomic structure, or the specimen thickness. In general EELS is used for elemental mapping and chemical analysis of a samples composition. Due to its sensitivity to light elements, it is commonly used as supplementation to EDS, which has a much larger yield for heavier elements than for lighter ones. A typical EELS spectrum consists of three main regions, see Fig. 4.13. The first one is the zero loss peak (ZLP) region, which contains only electrons which have not interacted inelastically with the sample material. The second one is the plasmon region (~10–50 eV), which is described by collective oscillations of the valence electrons. The last one is the core loss region, which contains the ionization edges (> 100 eV) and thus the actual analytical/structural information.
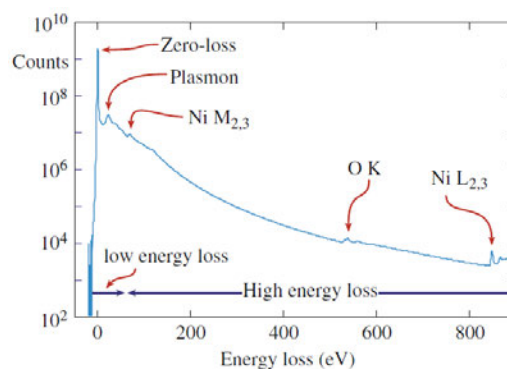
Fig. 4.13: An EELS spectrum displayed in logarithmic intensity mode. The zero-loss peak is an order of magnitude more intense than the low energy-loss portion (characterized by the plasmon peak), which is many orders of magnitude more intense than the small ionization edges identified in the high energy-loss range. Note the relatively high (and rapidly changing) background [87].

4.4   Mechanical Investigations

4.4.1   Nanointendation

One of the well-established methods for determining mechanical properties of thin films and hard coatings (such as hardness H and indentation modulus E), is nanoindentation. Within this technique the resistance of a material against penetration (elastic and plastic deformation) is measured by a defined Berkovich indenter (a three-sided diamond pyramid tip with a half angle of 65.3°). Load (P) and displacement (h) curves are monitored and subsequently evaluated according to Oliver and Pharr [88]. A scheme of a measurement, is shown in Fig. Fig. 4.14. The hardness values of the measured sample can be obtained by dividing the applied load, by the contact area, at each point along the loading curve. The indentation modulus can be derived from the lower unloading part of the load-displacement curve, where dP/dh at h_m corresponds to the stiffness (S) of a material.

In the case of thin solid films, the indentation depth should be lower than 1/10 of the coating thickness, to avoid any influence of the (mostly softer) substrates. That means the plastic deformation zone should not reach the coating-substrate-interface. Another important factor that should be considered when evaluating the load-displacement curves is the deviation of the tip from its ideal shape. For arc evaporated coatings, which typically exhibit a high surface roughness, a pre-treatment in form of polishing is necessary, in order to minimize data scattering and faulty results. Differences in the temperature of tip and sample also may have a significant influence on obtained data, which is why a certain acclimation has to be considered.
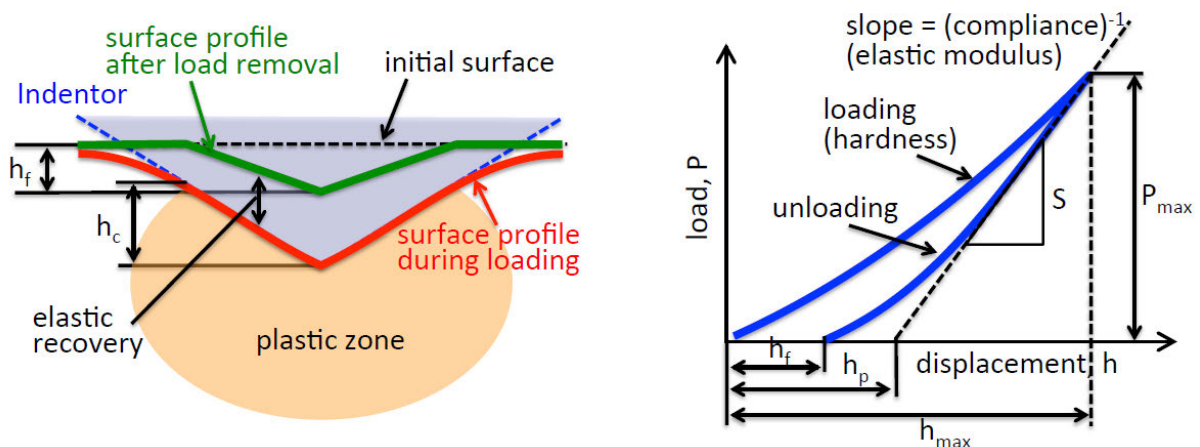
Fig. 4.14: Schematic response of a material to indentation and a typical load-displacement curve [18].

4.5 Roughness measurements

4.5.1 Profilometry

The roughness measurements within this work were performed using a profilometer. It works with a non-contact chromatography for highly accurate, fast 3D surface height measurements from 0.1 nm to 1 mm, see Fig. 4.15.

The huge benefit of the white light axial chromatism technology is a contact free measurement, which monitors relative heights based on wavelength detection that is reflected by the sample surface. Due to the direct measurement principle, there are no computational manipulations necessary [18].
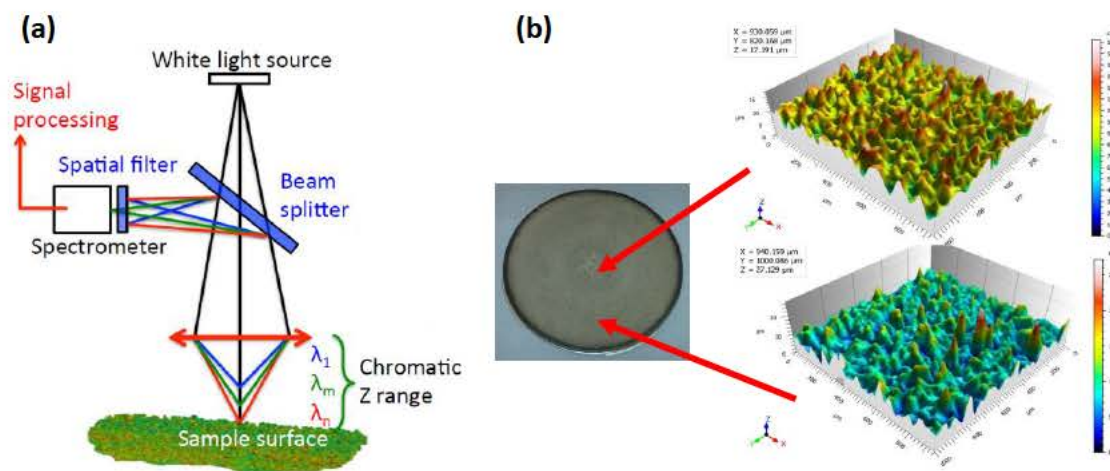
Fig. 4.15: (a) Principle of a white light interferometer (profilometer) used within this thesis [18], (b) 3D surface height measurements of a used cathode

4.6 Simultaneous thermal analysis

Microstructural and mechanical properties of hard coatings may be excellent in as-deposited state. However, during applications coatings will face more severe conditions, especially with high thermal input. To determine the usability of thin film materials as protective coatings in such extreme conditions, primary changes of the system in the desired temperature range have to be known (e.g., phase changes and/or mass loss/gain). Basically, this can be achieved by in-situ or ex-situ techniques. In the first case, the measured signals are monitored directly at a given time and temperature. The latter technique demands for subsequent investigations as for instance XRD after post-deposition annealing to evaluate the performance of the coatings.

A major advantage of a simultaneous thermal analysis (STA) is the combination of several measurement techniques, due to the identical measurement conditions (type of furnace and sample holder, sample mass, heating and cooling rate, gas flow conditions, etc.) and the perfect correlation of the different signals (all data are obtained from the same sample at the same time).

In this work a STA measuring device was used, Fig. 4.16, combining differential scanning calorimetry, or a differential thermal analyses, with a thermogravimetric analyses, which will be explained in more detail in the next subsections. During the measurements, a Rh-furnace (T_{max} = 1650 °C) is covering the sample carrier and the desired dynamic atmosphere [inert (i.e. He) or oxidizing (synthetic air)], is adjusted. The time-temperature program, which the sample is measured with, can be continuous or isotherm. The resulting signals, i.e. heat flow and mass change, are monitored by the corresponding sensors, recorded, and analysed by the respective software.
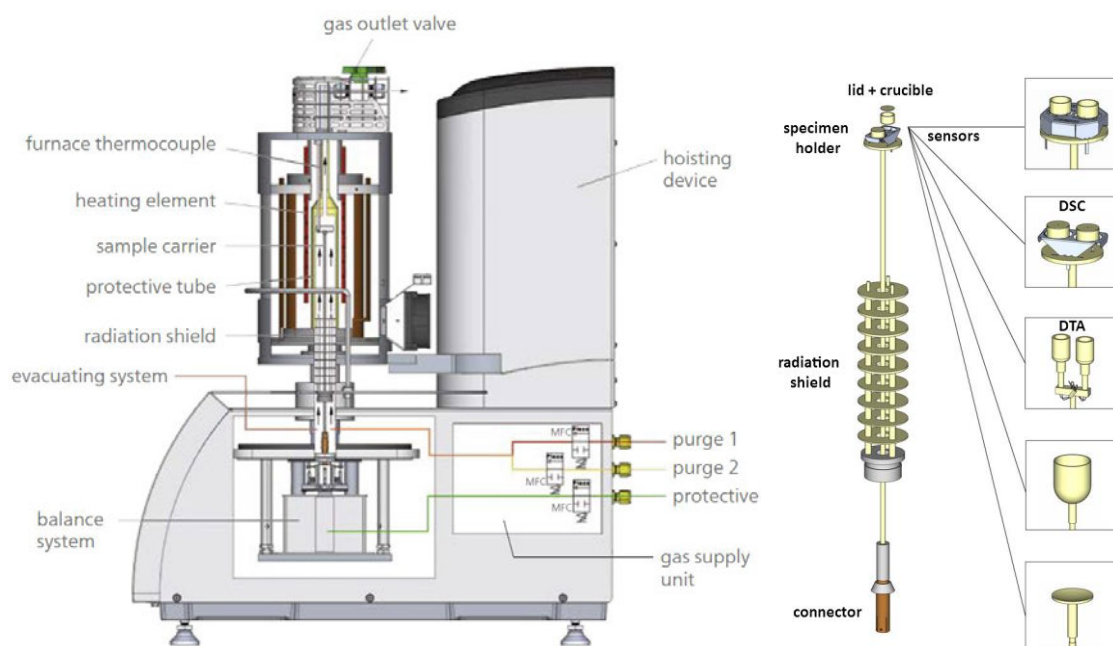
Fig. 4.16: Cross section of a STA 449 F1 Jupiter® from NETZSCH [89] with corresponding sample holder.

STA is a perfect technique to analyse thin films, due to the small amount of material necessary to obtain usable results. However it is important to note, that one cannot distinguish between the influence of the coating itself and the corresponding substrate material. Therefore, substrates, which are thermally inert in the applied temperature range, should be used. These are typically Al_2O_3 or MgO. Another option is to separate the film from the substrate. In this work, the coated low-allowed steel foil was chemically dissolved in nitric as well as hydrochloride acid. The remaining free-standing coating was subsequently either grinded to obtain coating powder, or retained in form of small coating flakes. This removal procedure should in general not influence properties of the investigated films (e.g., their chemical composition). Sample preparation from plain substrates into a STA crucible is shown in Fig. 4.17 by the example of $Ti_xZr_{1-x}N$ [51].

Fig. 4.17: Sample preparation steps for STA measurements to obtain film material without substrate. Low alloyed steel foils (a) coated with $Ti_xZr_{1-x}N$ (b). Cleaned powder after chemical substrate removal (c) placed in a STA crucible with lid (d) [51].

4.7 Differential scanning calorimetry

Differential scanning calorimetry (DSC) is a thermal analysis technique which measures the difference in temperature and heat flow rate (associated with transitions in materials) to a reference sample as a function of temperature and time [90]. Such measurements provide quantitative and qualitative information about physical and chemical changes in the samples that include endothermic (e.g., evaporation, decomposition, precipitation) and exothermic (e.g., relaxation/recovery, crystallization, oxidation) processes. The temperature difference between the sample and the reference—from which the heat flow rate can be obtained—is measured by a differential thermocouple. Only a few milligrams in mass of the sample material is used for DSC analysis, which makes it a perfect method for characterizing the thermal stability of thin films (limited coating volume available). Before starting the first DSC measurements, the equipment has to be calibrated using elemental standards with melting points covering the temperature range of interest. The resulting calibration curves for temperature and sensitivity can just be used for one defined set of measurement conditions. If any of these parameters—furnace, atmosphere, heating rate, crucible material, or sample carrier—change the entire calibration is not valid anymore. To avoid or compensate any influence from the used crucibles (also lids and inlays) a base line—measured with empty crucibles under identical conditions—is subtracted from the original measured data. It should be also noted that the crucibles themselves, the included samples, as well as the reference material change the symmetry of the system, due to their own heat capacity. Therefore using an inert reference material with equal thermal properties to the sample is one way to optimize the measurement conditions. Another way is the use of an empty crucible as reference [91], as it is done in this work. Irreversible reactions (e.g., recovery, crystallization, decomposition, precipitation) can be identified by another measurement (rerun), see Fig. 4.18, which contains the characteristics of an 'inert' sample without all the one-way reactions.
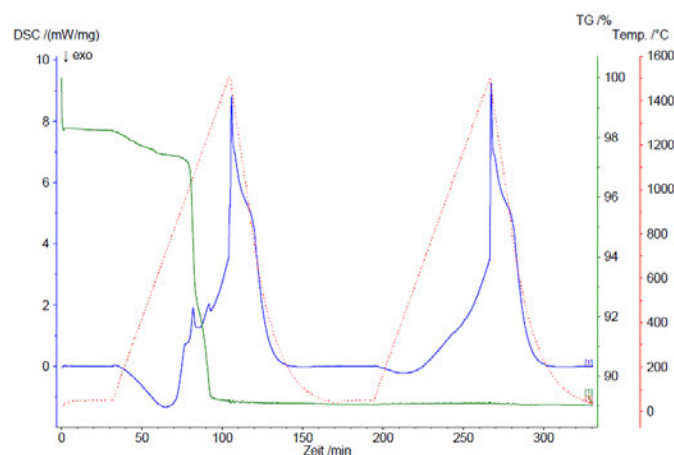
Fig. 4.18: DSC (blue) and TG (green) signals of an $Al_xCr_{1-x}N/(Al_xCr_{1-x})_2O_3$ multilayer coating annealed in dynamic inert (He) atmosphere. The use temperature program is indicated by the red dotted line.

4.8   Differential thermal analysis

The only difference of differential thermal analysis, DTA and DSC is that with the latter technique just the temperature difference is monitored during a measurement.

4.9   Thermogravimetric Analysis

Thermogravimetric analysis (TGA) or thermogravimetry (TG) is a thermal analysis method for measuring the sample mass and/or mass difference as a function of temperature and/or time [91], see Fig. 4.18. A positive or increasing mass change can be related to reaction with an oxidising atmosphere and a negative or decreasing mass change can be correlated to e.g. decomposition with volatile reaction products, see Fig. 4.19.
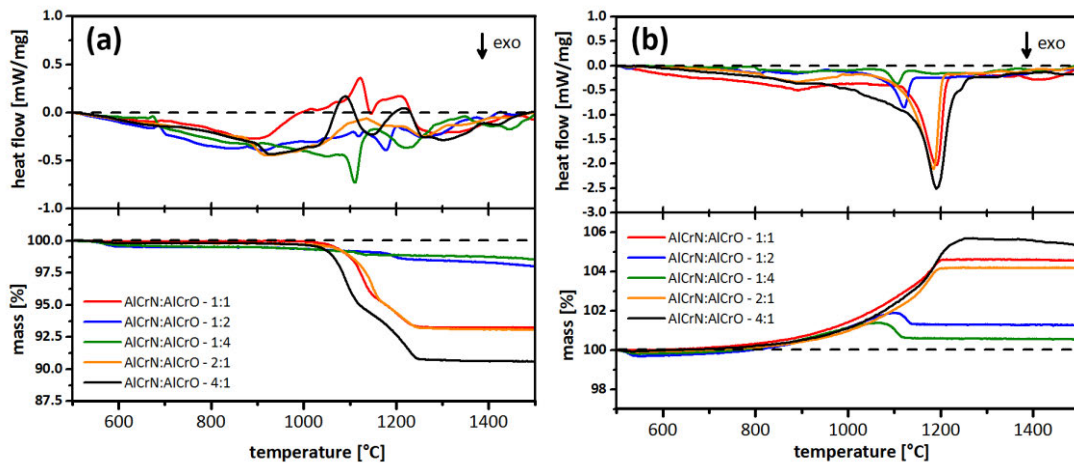
Fig. 4.19: DSC and TG signals of $Al_xCr_{1-x}N/(Al_xCr_{1-x})_2O_3$ multilayers with 80 bilayers (bilayer period ~ 45 nm) and different nitride to oxide ratios of the individual layers, annealed in dynamic (a) inert (He) and (b) oxidizing (synth. air) atmosphere.

<div align="right">

CHAPTER 5

</div>

5. Interfaces in arc evaporated Al-Cr-N/Al-Cr-O multilayers and their impact on hardness

5.1 Introduction

The most common industrially used material systems—synthesised by cathodic arc evaporation—are nitrides and oxides. Among these, Al-Cr-based films are particularly suitable for a multitude of applications, which not only require a balanced and tailored property spectrum up to 1000 °C (and beyond), but also the capability to withstand oxidising and chemically invasive environments [31,52,92–97]. However, increasing demands for higher application temperatures and extended duty cycles, require improvements even for already well-established coatings. The development of hard protective coatings presumes throughout knowledge about fundamental correlations of deposition parameters, their implications on the coatings microstructure and therewith attainable-properties. These have been intensively investigated concerning $Al_xCr_{1-x}N$, $(Al_xCr_{1-x})_2O_3$, as well as its combination in terms of quaternary Al-Cr-O-N [60,61,67,71]. Although, considerable research activities were carried out with the focus on quaternary Al-Cr-O-N hard coatings (driven by the possibility to stabilise the fcc structure even at a high Al contents), only little is known about an architectural design, combining distinct $(Al,Cr)_2O_3$ and $Al_xCr_{1-x}N$ layers themselves. Therefore, $Al_xCr_{1-x}N/(Al_xCr_{1-x})_2O_3$ multilayer coatings were developed by reactive arc evaporation with modified interface fractions and thicknesses. This allows for a correlation between architecture (defined by the interface fraction and thickness) and resulting microstructure and mechanical properties of the $Al_xCr_{1-x}N/(Al_xCr_{1-x})_2O_3$ multilayers.

5.2 Experimental

All coatings were deposited using an Oerlikon Balzers Innova batch-type cathodic arc evaporation system equipped with powder metallurgically (PM) prepared $Al_{0.7}Cr_{0.3}$ targets (Plansee Composite Materials GmbH). After ultrasonically cleaning with ethanol and acetone, the substrates (Si) were mounted on a two-fold rotation carousel with a minimum target-to-substrate distance of approximately 25 cm—and heated up to deposition temperatures of 500 °C by a combined radiation and plasma heating process for approximately 30 min. Ar ion etching for 30 min, applying the Balzers Central Beam Etching Technology, was used for a further, enhanced removing of residuals and native oxides from the substrate surfaces. Thereby, the coating adhesion to the substrates is increased.

The multilayer architecture of our coatings was realised by alternatively operating two out of four active neighbouring cathode positions in nitrogen and oxygen atmosphere, respectively. In detail, the individual nitride layers were synthesised with an arc current of 150 A and a nitrogen flow rate of 1100 sccm, whereas for the oxide layers the other two cathodes were operated at 180 A with an oxygen flow rate of 1000 sccm injected to the cathode surface. The average deposition pressure of the individual nitride and oxide layers was ~3.6 Pa and ~2.6 Pa, respectively. In order to enhance growth kinetics, a negative bipolar pulsed substrate bias of -40 V was applied. Variation in the bilayer period, thus overall interface fraction, was realised by reducing the active source times from 145, 60, to 30 s, resulting in 12, 25, and 50 bilayers [i.e., 24, 50, and 100 layers (nitrides and oxides)] in total. In addition, three different interface types—referred to as distinct, hybrid, and blurred—were established by adjusting the gas-exchange between nitrogen and oxygen as shown in Fig. 5.1, in combination of switching–on and –off of the corresponding two cathodes. For all coating variations, the process started in nitrogen atmosphere, due to the better adhesion of the nitride layers to the substrates (indicated by red layers in Fig. 5.1). An overlapping gas-exchange between oxygen and nitrogen after the active source times of 145, 60, or 30 s after which two operating cathodes (nitride deposition) are switched off and simultaneously the other two cathodes (oxide deposition) are ignited—and vice versa—leads to the formation of *blurred* interfaces between the nitride and oxide layers. A *distinct* transition between the individual nitride and oxide layers was realised by switching off all sources until the gas exchange was completed (this takes about 37 s in the machine), before the corresponding targets were ignited again. For the *hybrid* interface type, both process schemas are combined, where the transition from nitride to oxide layers is blurred, but the transition from oxide to nitride layers is distinct, as indicated in Fig. 5.1.

Chemical and morphological investigations of our multilayers were carried out using a FEI Quanta 200 Field Emission Gun Scanning Electron Microscope (FEG SEM) with an Energy Dispersive X-Ray Spectroscopy (EDS) detector attached. The surface topography was evaluated with a Nanovea PS 50 Profilometer averaging three measurements at different sample positions.

Information on the crystallographic composition was obtained by X-Ray Diffraction (XRD) in grazing-incidence arrangement (GI, angle of incidence $\Omega = 2°$, $2\theta = 15–90°$) using an Empyrean PANalytical θ-θ diffractometer with a Cu K$_\alpha$ radiation source and a scintillation detector.

More detailed examinations on the coating microstructure, and in particular the different interfaces between nitride and oxide layers, were realised by transmission electron microscopy (TEM) including high resolution TEM (HR-TEM), scanning TEM (STEM), selected-area electron diffraction (SAED), and EDS, using a TECNAI F20 FEG TEM operated with an acceleration voltage of 200 keV.

Analysis of hardness (H) and indentation modulus (E) was carried out by nanoindentation using an Ultra-Micro-Indentation II system equipped with a Berkovich diamond tip. Normal loads ranging from 16 to 2 mN in steps of 0.5 mN were applied and the indentation curves were evaluated according to Oliver and Pharr [88]. Special attention was paid to the overall indentation depths in order to minimise substrate interference.
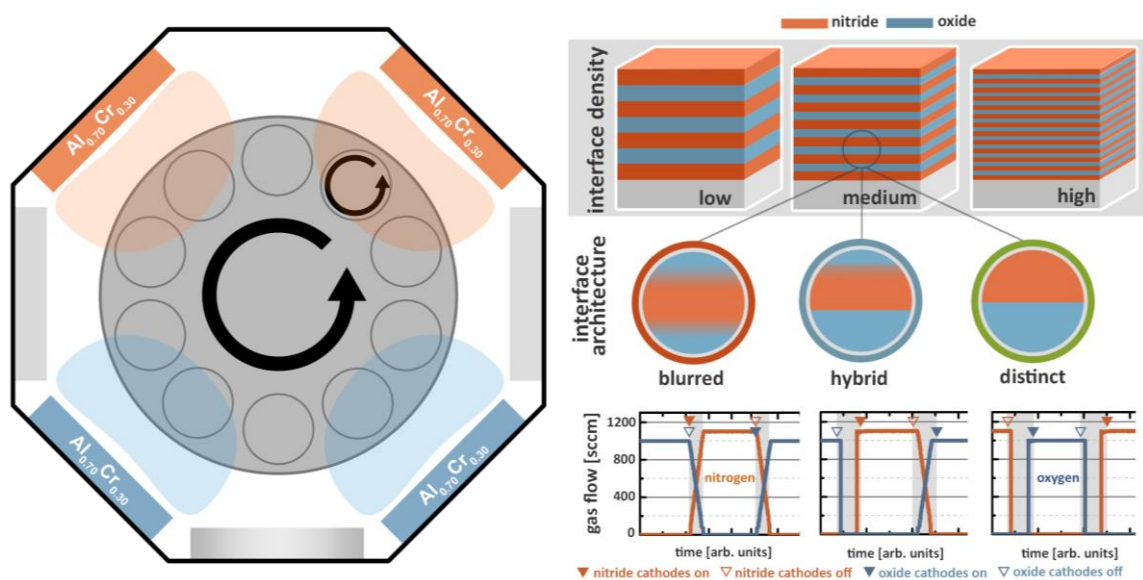
Fig. 5.1: Schematic illustration of the two fold substrate rotation deposition chamber including the individual cathode arrangement as well as the resulting three different interface geometries (blurred, hybrid, distinct) and interface volume fractions (low, medium, high) established within our (Al,Cr)N/(Al,Cr)$_2$O$_3$ multilayers.

5.3 Results and discussion

5.3.1 Growth morphology and chemical composition

Table 5.1: Elemental composition of $(Al,Cr)N/(Al,Cr)_2O_3$ multilayers obtained by SEM-EDS.

interface	architecture	elemental composition [at.%]				$(Al+Cr)/(N+O)$	$Al/(Al+Cr)$	$Cr/(Al+Cr)$	$N/(N+O)$	$O/(N+O)$
	[bilayers]	Al	Cr	N	O	[-]	[%]	[%]	[%]	[%]
distinct	12	27.1	13.3	18.5	41.2	0.68	67.1	32.9	31.0	69.0
distinct	25	25.5	12.4	15.4	46.7	0.61	67.3	32.7	24.8	75.2
distinct	50	25.0	12.2	11.2	51.6	0.59	67.2	32.8	17.9	82.1
hybrid	12	27.0	12.2	17.7	43.1	0.65	68.8	31.2	29.1	70.9
hybrid	25	26.2	11.9	14.1	47.8	0.62	68.8	31.2	22.8	77.2
hybrid	50	25.4	11.9	10.1	52.5	0.60	68.2	31.8	16.2	83.8
blurred	12	26.6	12.0	18.7	42.7	0.63	68.8	31.2	30.4	69.6
blurred	25	26.4	11.9	12.8	49.0	0.62	69.0	31.0	20.7	79.3
blurred	50	25.7	12.3	10.3	51.7	0.61	67.7	32.3	16.6	83.4

The chemical compositions of our $(Al,Cr)N/(Al,Cr)_2O_3$ multilayers, obtained by SEM-EDS, are presented in Table 5.1. All coating variations contain slightly lower Al- and slightly increased Cr-contents compared to the nominal target composition. This is in agreement with previous reports about arc evaporated monolithically grown and multi-layered $Al_xCr_{1-x}N$ coatings, using PM Al_xCr_{1-x} targets [46,48]. In the case of $(Al,Cr)_2O_3$ films, however, there are diverging reports, which indicate a certain dependence on the crystallographic composition. For fcc-like Al-Cr-O coatings, Najafi et al. observe a reduced Al-content [98], whereas for coatings with fcc and hexagonal corundum type phases an enrichment in Al is detected [55,99].

However, we observe a significant increase in oxygen content—accompanied by a reduction in nitrogen content—with increasing number of bilayers for the three coating series (with blurred, hybrid, and distinct interface types). Thus, the oxygen fraction (i.e., the O/(N+O) ratio) increases from ~70 to 83% with increasing number of bilayers. This is also represented by the total process pressure (showing a logarithmic-like function with process time), which reaches an almost constant value of ~3.3 Pa already after 30 min, when preparing the coatings with 50 bilayers. Contrary, the pressure steadily increased from ~2.7 to ~3.1 Pa during the process of the coatings with 12 bilayers.

When comparing the multilayers with the same number of bilayers but different interface geometries, the results seem to be within the error of measurement. But the calculated cation-to-anion ratio [C/A i.e., the (Al+Cr)/(N+O) ratio, see Table 5.1] shows a correlation with the interface geometry as well. For our multilayers with distinct interfaces the C/A ratio almost decreases from 0.68 to 0.59, whereas for multilayers with blurred interfaces the C/A ratio only decreases from 0.63 to 0.61. For multilayers with hybrid interfaces, the C/A variation is in-between these extremes. When

considering the combination of nearly stoichiometric oxides (i.e., C/A = 2/3) [21,55,99] with stoichiometric nitrides (i.e., C/A = 3/3) [48], the C/A-ratio should be between 2/3 and 3/3 [67]. Except for the multilayer with distinct interfaces and fewest number of interfaces, all of our coatings show C/A ratios below 2/3. Consequently, the interface region (between oxide and nitride layers) has to contain a C/A ratio significantly below 2/3. In combination with the increase in oxygen content with increasing number of bilayers, this suggests for a significant oxygen content at the interfaces, by trend higher for blurred than for distinct interfaces.

The growth morphology of our 9 different $(Al,Cr)N/(Al,Cr)_2O_3$ multilayer coatings is presented in a table-like arrangement of SEM fracture cross sections in Fig. 5.2—interface variation along the rows (blurred: a, b, c, or hybrid: d, e, f, or distinct: g, h, i) and bilayer variation along the columns (12 bilayers: a, d, g, or 25 bilayers: b, e, h, or 50 bilayers: c, f, i). The bright and dark contrasted layers correspond to $(Al,Cr)N$ and $(Al,Cr)_2O_3$, respectively. For the multilayer coatings with 12 bilayers (Fig. 5.2a, d, and g) as well as 25 bilayers (Fig. 5.2b, e, and h) the individual average layer thicknesses are almost constant across the entire coating thickness. The multilayers with 50 bilayers (Fig. 5.2c, f, and i) reveal a periodic change in layer thicknesses, represented by a contrast-superstructure—especially visible for the multilayer with distinct interfaces, Fig. 5.2i. This superstructure is the result of the interference between a certain two-fold substrate rotation speed and a certain cathode-operating time. Generally, if the cathode-operating time is smaller than the time needed for a complete rotation—and the times are not synchronized—the time a substrate faces an operating cathode changes with the rotations. This in turn leads to varied layer thicknesses (due to varied times in which the substrates face the operating cathodes) along the coating thickness. Substrate-rotation-simulations (not shown here), based on the model of Rother [100], proof this behaviour for the facility and deposition conditions used.
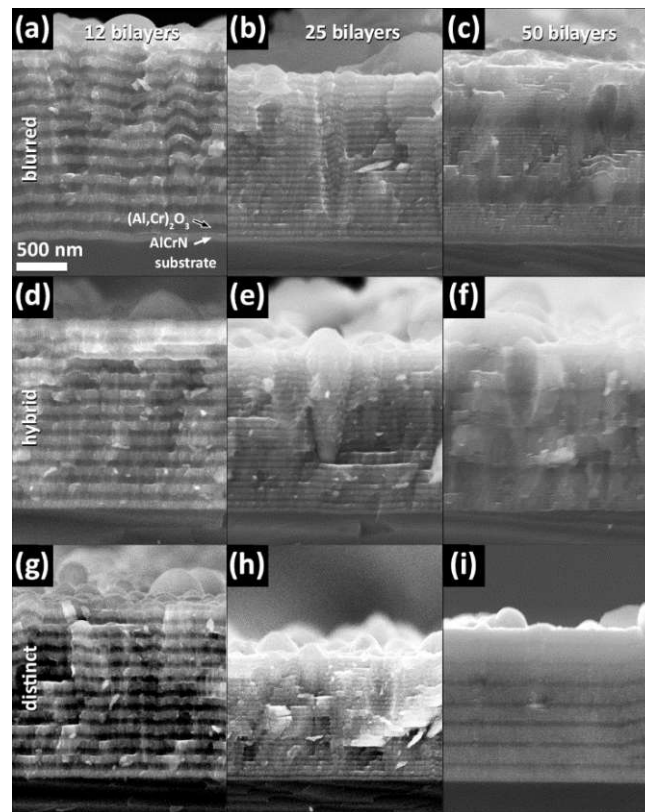
Fig. 5.2: Cross-sectional SEM images of (Al,Cr)N/(Al,Cr)$_2$O$_3$ multilayer coatings with (a, b, c) blurred, (d, e, f) hybrid, and (g, h, i) distinct interfaces, and 12, 25, and 50 bilayers, respectively, given with the same magnification.

Top-view SEM images of our multilayers reveal only a slight correlation between surface topography and bilayer periods or interface geometries (Fig. 5.3) in the same table-like arrangement of SEM images for the nine multilayer coatings like Fig. 5.2 (interface variation along the rows (blurred: a, b, c, or hybrid: d, e, f, or distinct: g, h, i) and bilayer variation along the columns (12 bilayers: a, d, g, or 25 bilayers: b, e, h, or 50 bilayers: c, f, i). The formation of droplets seems to be much higher for layers processed in oxygen atmosphere, which is also indicated in previous literature reports [24,46,48,55]. The rather high fraction of growth defects, primarily due to the deposition process of the oxide layers, is between those for monolithically grown (Al,Cr)N and (Al,Cr)$_2$O$_3$ films. The corresponding surface roughnesses R$_a$ and R$_z$ are presented in Fig. 5.4.

Fig. 5.3: Top-view SEM images of (Al,Cr)N/(Al,Cr)$_2$O$_3$ multilayer coatings with (a, b, c) blurred, (d, e, f) hybrid, and (g, h, i) distinct interfaces, and 12, 25, and 50 bilayers, respectively, given with the same magnification.

With increasing number of bilayers, hence increasing interface fraction, as well as decreasing thickness of the interfaces (i.e., from blurred to hybrid to distinct) the R$_a$ values decrease, while the R$_z$ values rather show a wide spread, see Fig. 5.4. The shorter the active source time (i.e., deposition time per layer, which decreases from 145 to 30 s) and the thinner the interface, the smoother is the surface. Both, interface fraction and thickness influence the re-nucleation processes and thus influence the surface roughness. Additionally, prevailing conditions at the cathode surface (i.e., presence of high- or low-melting phases or reaction zones) significantly influence the droplet generation and thus also the number of defects in our coatings.
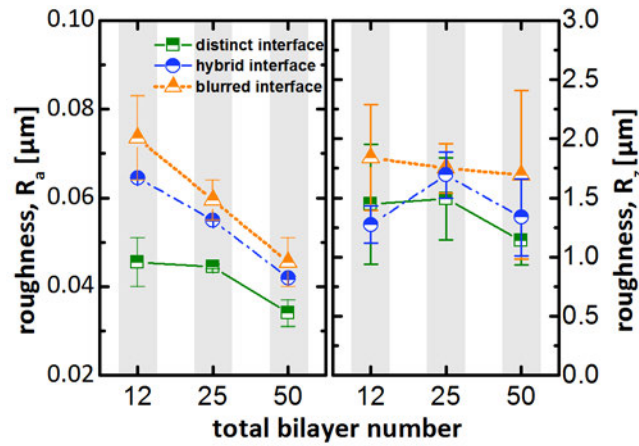
Fig. 5.4: Roughness values of $(Al,Cr)N/(Al,Cr)_2O_3$ multilayer coatings with blurred, hybrid, and distinct interfaces combined with 12, 25, and 50 bilayers.

5.3.2 Structure

X-ray diffraction of all $(Al,Cr)N/(Al,Cr)_2O_3$ multilayers, Fig. 5.5, exhibit a face-centred cubic structure, with decreasing peak-intensity for increasing number of bilayers. For comparison, also the XRD patterns of monolithically grown $(Al,Cr)N$ and $(Al,Cr)_2O_3$ coatings are added to the bottom. Separated $(Al,Cr)N$ and $(Al,Cr)_2O_3$ -XRD peaks can only be detected for the multilayers with the smallest interface fractions (i.e., 12 bilayers per total coating thickness), Fig. 5.5. The rather broad and low-intensity XRD peaks at around 37.8, 44.2, and 64.4° of 2θ can be assigned to (111), (200), and (220) lattice planes of the nitride layers, and those at around 44.8 and 66.0° 2θ are assigned to (200) and (220) lattice planes of fcc-$(Al_xCr_{1-x})_2O_3$. The decreasing XRD peak intensity with increasing interface fraction (i.e., increasing number of bilayers) suggests for decreasing coherently scattering domain sizes due to decreasing layer thicknesses. Furthermore, the full width at half maximum—evaluated for the (200) peaks of the multilayers with 12 bilayers at 2θ ~44°—increases from 0.63° to 0.73° to 0.77° from blurred to hybrid to distinct interface type/architecture, respectively.

66
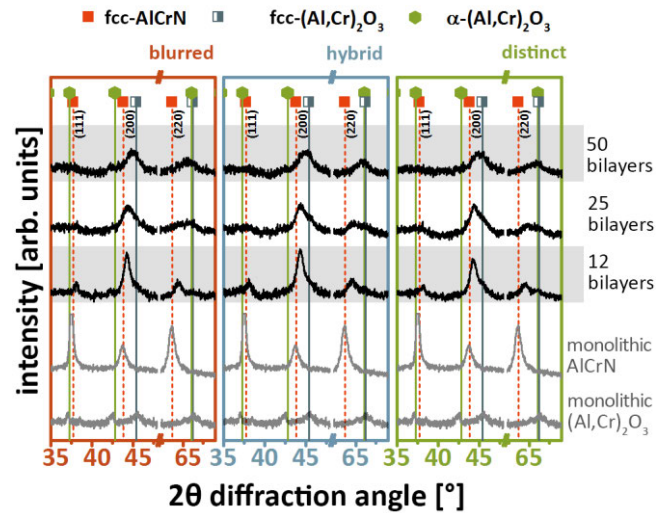
Fig. 5.5: Grazing-incidence X-ray diffraction patterns of multilayered (Al,Cr)N/(Al,Cr)$_2$O$_3$ coatings processed with 12, 25, and 50 bilayers and (a) blurred, (b) hybrid, and (c) distinct interface geometries. For comparison, monolithically grown (Al,Cr)N and (Al,Cr)$_2$O$_3$ coatings are added.

Transmission electron microscopy cross-section studies of our nine multilayer coatings—presented in Fig. 6 in the same arrangement as used for Fig. 5.2 and Fig. 5.3 [i.e., interface variation along the rows (blurred: a, b, c, or hybrid: d, e, f, or distinct: g, h, i) and bilayer variation along the columns (12 bilayers: a, d, g, or 25 bilayers: b, e, h, or 50 bilayers: c, f, i)]—yield underdense interfaces especially for the blurred transition between nitride and oxide (layers). The latter are indicated in Fig. 5.6 by white dotted lines, whereas the distinct transition between nitride and oxide layers is marked by white dashed lines (remember that the multilayer coatings termed with "hybrid" are characterized by a distinct transition from oxide to nitride layers but a blurred transition from nitride to oxide layers). Bright-contrasted layers represent the Al,Cr-oxide. The arrangement of the TEM cross-sections in Fig. 5.6 nicely shows that the interface fraction (across the entire coating thickness) successively is doubled, when increasing the number of bilayers from 12 to 25 to 50 (from left to right). Thus, the corresponding bilayer period λ successively divides by ~2 from ~170 to 80 to 40 nm. Selected area electron diffraction patterns of all coatings were obtained using a 160 nm aperture, placed at intermediate positions between substrate and film surface. In excellent agreement with our XRD results (Fig. 5.5), all multilayers crystallise in a face-centred cubic structure. The SAED patterns demonstrate diffraction rings (with highest intensities for (200) and (220) lattice planes) which appear more continuous for coatings with thinner bilayer periods—indicating finder grained structures.

Partial epitaxial growth of crystallites through the interfaces between nitride and oxide layers— indicated by dashed vertical white lines—are especially present for the multilayer with distinct interfaces and a high interface fraction, Fig. 5.6c. It is furthermore noteworthy, that the oxygen layers within the 12 bilayer coatings are generally less dense compared to the nitride layers (see Fig. 5.6a and d; bright, underdense column boundaries are marked with solid white lines).
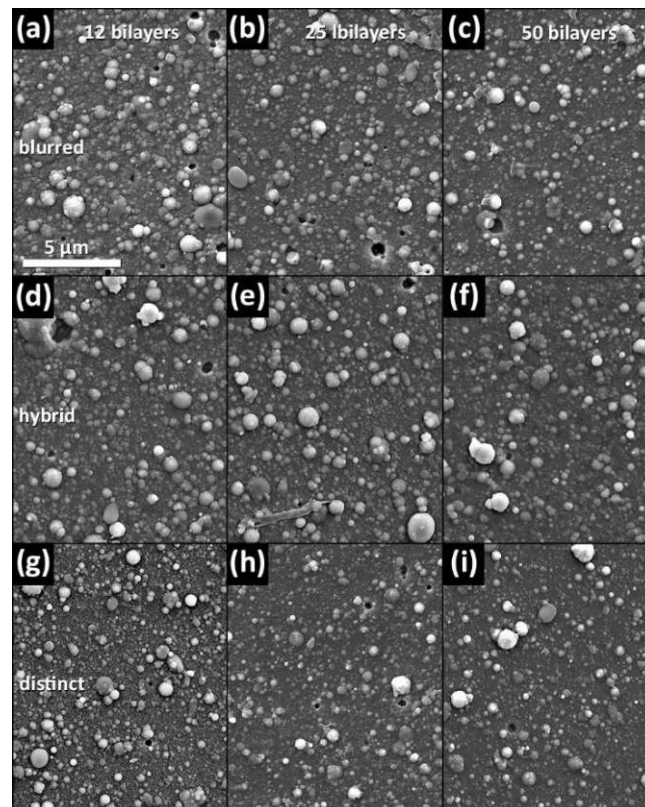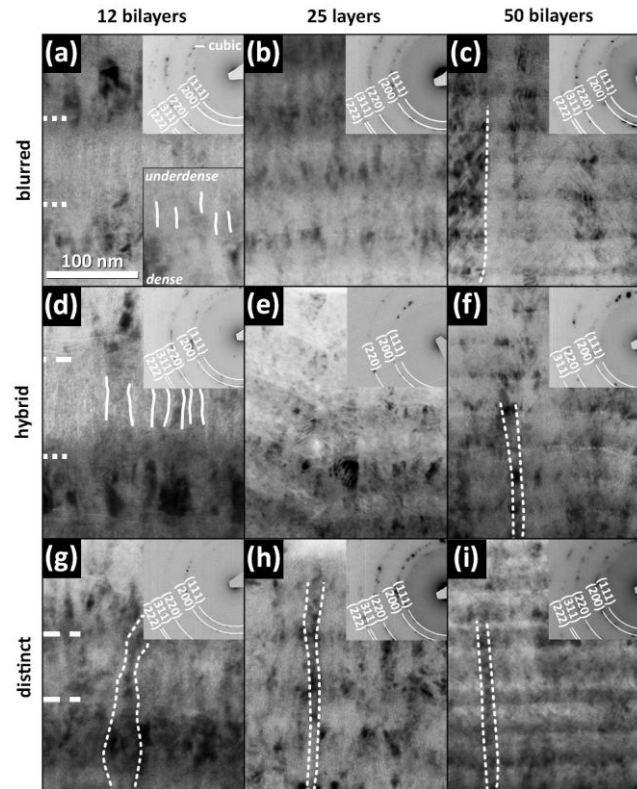

Fig. 5.6: Cross-sectional TEM images of (Al,Cr)N/(Al,Cr)$_2$O$_3$ multilayer coatings with (a, b, c) blurred, (d, e, f) hybrid, and (g, h, i) distinct interfaces, and 12, 25, and 50 bilayers, respectively. Solid vertical white lines indicate underdense grain boundaries and dashed vertical white lines continuous crystal growth through (Al,Cr)N and (Al,Cr)$_2$O$_3$ layers.

5.3.3 Mechanical properties

The hardness of our multilayer coatings with blurred interfaces (orange half-filled triangles, Fig. 5.7) significantly increases with increasing interface density (i.e., number of bilayers) from 14±1 to 22±1 GPa. Also the coatings with distinct interfaces (green half-filled rectancles, Fig. 5.7) exhibit an increased hardness, but only from 19±1 to 21±2 GPa. Again, the coatings with hybrid interfaces (blue half-filled circles, Fig. 5.7) are somehow in-between and also the indentation moduli exhibit a comparable trend, see Fig. 5.7. The influence of the different interface types on hardness is most pronounced for the (Al,Cr)N/(Al,Cr)$_2$O$_3$ multilayers with 12 bilayers , which demonstrate hardnesses of ~14,

~16, and ~19 GPa for blurred, hybrid, and distinct interface types, respectively. In the case of distinct interfaces, the relatively short transition from nitride lattice to oxide lattice (and therewith associated lattice mismatch) leads to a more effective hindering of dislocation mobility than, e.g., a gradient transition between these layers Moreover, the density of the individual layers is higher for the distinct interface type as compared with the blurred or gradient interface (please compare Fig. 5.6a, d, and g). With increasing interface fraction and thus reduced active source time per individual layer, the difference between the interface types diminishes. However in agreement with our previous results— chemical composition, growth morphology, and structure—also the mechanical properties (hardness and indentation moduli) approach the same values if the coatings with different interface types are prepared with the highest fraction of interfaces. For these coatings, the hardness with 22±1 GPa and indentation moduli with 250±12 GPa are almost perfectly in-between the values for monolithically grown (Al,Cr)N [48] and $(Al,Cr)_2O_3$ deposited using four cathodes at 500 °C. The hardness of 6±0.5 GPa of our monolithically grown $(Al,Cr)_2O_3$ can be explained by the relative low bias voltage of -40 V (DC) applied during film growth. Koller et al. [101] recently showed that the hardness of monolithically grown $(Al,Cr)_2O_3$ synthesised with four cathodes at 550 °C can increased from ~12±2 GPa to ~25±2.5 GPa by increasing the bias voltage from -60 V to -160 V (pulsed), respectively, while Pohler et al. [99] furthermore demonstrated that by an optimised bipolar pulsed substrate bias (amplitude of ±60 V and a frequency of 25 kHz) hardnesses of even ~25 GPa can be obatined (using six $Al_{0.7}Cr_{0.3}$ cathodes).
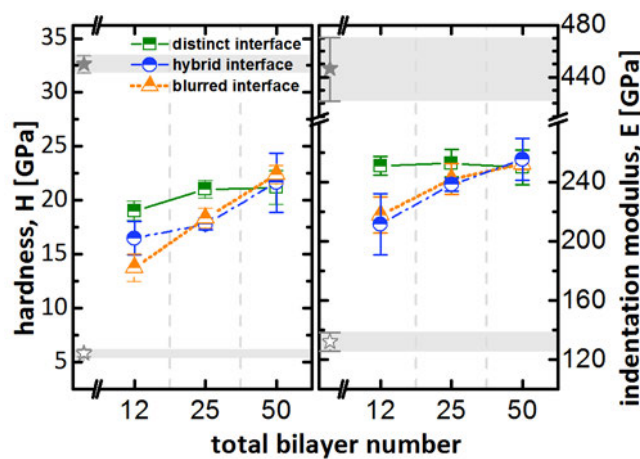
Fig. 5.7: Hardness and indentation modulus of monolithically grown (Al,Cr)N (filled stars), $(Al,Cr)_2O_3$ (open stars), as well as $(Al,Cr)N/(Al,Cr)_2O_3$ multilayer (half-filled symbols) coatings with blurred, hybrid, and distinct interfaces, and 12, 25, and 50 bilayers.

5.4 Summary and conclusions

A series of ~1.2–2 µm thin $(Al,Cr)N/(Al,Cr)_2O_3$ multilayer coatings with three different interface designs and three different total number of bilayers (hence, three different overall interface volume fractions) was deposited by reactive cathodic arc evaporation. The multilayer arrangement of nitride and oxide layers was realised by alternatively processing two (out of six) neighbouring PM $Al_{0.7}Cr_{0.3}$ cathodes in nitrogen and oxygen atmospheres, respectively. Reducing the active source time from 145 s to 60 s to 30 s leads to an increase in total number of bilayers from 12 to 25 to 50. Thus, the interface fraction is successively almost doubled resulting in decreasing bilayer periods from 170 to 80 to 40 nm. Clearly separated gas exchanges between nitrogen and oxygen lead to distinct interfaces between the individual nitride and oxide layers, whereas an overlap of nitrogen-outlet and oxygen-inlet leads to blurred interfaces between them.

Regardless of their interface types (distinct or blurred), all multilayers exhibit a cubic (fcc) structure. For the multilayers composed of 12 bilayers (hence, the largest bilayer period of ~170 nm), the individual nitride and oxide layers can be detected by XRD. Those, composed of 25 and 50 bilayers exhibit broad and significantly overlapping XRD peaks, due to their smaller bilayer periods (below 80 nm) and the close lattice parameters between cubic $(Al,Cr)N$ and cubic $(Al,Cr)_2O_3$.

With decreasing bilayer periods, not only higher surface qualities can be obtained, but also a significant improvement in mechanical properties. This is especially pronounced for the multilayers with blurred interfaces between the nitride and oxide layers, demonstrating a hardness increase from ~14 to ~16 to ~22 GPa with increasing number of bilayers from 12 to 25 to 50. The impact of interface type on mechanical properties is most pronounced for $(Al,Cr)N/(Al,Cr)_2O_3$ multilayers with 12 bilayers, demonstrating ~14, ~16, and ~19 GPa, for blurred, hybrid, and distinct interfaces.

We could thus demonstrate, that by sophisticated interface design and coating architecture the microstructure and mechanical properties of arc evaporated $(Al,Cr)N/(Al,Cr)_2O_3$ multilayers can be effectively varied over a wide range and in further consequence used to adjust the coating properties to application-specific demands.

CHAPTER **6**

6. Thermal Stability of Arc Evaporated Al-Cr-O and Al-Cr-O/Al-Cr-N Coatings

6.1 Introduction

Aluminium-chromium-based oxides and nitrides synthesised by cathodic arc evaporation (CAE) are widely-used material systems for cutting, forming, or milling operations, owing to their outstanding thermo-mechanical properties or wear and oxidation resistance [31,52,92–97,102,103]. However, the need of a further increase in performance and lifetime of tools and components call for improvements even for these already well-established and widely-used coating systems. For state-of-the-art machining applications such as dry high-speed cutting, the protective coatings ought to withstand temperatures up to 1000 °C—ideally beyond and in highly adverse environmental conditions. Consequently, coatings tailor-made for specific applications have to fulfil several criteria that demonstrate complex interdependencies [30,31,52,97].

Mechanical properties and thermal stability of many Al-alloyed transition metal nitrides, such as $Al_xCr_{1-x}N$ depend on the incorporated Al-content, their crystal structure, and phase constitution [42–45]. The synthesis of mechanically favourable single-phase face-centred cubic (fcc) coatings is typically limited by the maximum solubility of Al (x ~0.7), beyond of which a typical dual phase constitution develops – consisting of fcc and hexagonal close packed (wurtzite-type, therefore simply abbreviation with w to indicate the difference to the hexagonal closed packed, hcp structure of Cr_2N, which is also a content of this work) phases [44,46]. Excellent mechanical properties ask for fcc phases (with max. Al-content), while excellent thermal stability ask for high Al-contents in a preferably single-phase structure (regardless if fcc- or w-structured) [30,31,46,47,104]. When combining both, typically single-phase fcc $Al_xCr_{1-x}N$ coatings with highest possible Al-content are preferred. For example, Sabitzer et al. [48] showed that the formation of wurtzite-type phases can be suppressed even up to x ~0.77, by a multi-layered arrangement and high ion bombardment.

Synthesis conditions in physical vapor deposition (PVD) and particularly CAE trigger the growth of supersaturated metastable (or even thermodynamically instable) coatings,

which are thus subject to thermally-induced decomposition processes. $Al_xCr_{1-x}N$ coatings for example, decompose towards w-AlN and body centred cubic (bcc) Cr (via the formation of hcp Cr_2N under N_2-release) when annealed to temperatures beyond 900 or 1000 °C [30,31,33,52]. Such phase transitions, significantly influence (e.g., even degrade) the coating performance. Therefore, especially the w-AlN formation and the Cr–N dissociation should be retarded beyond the maximum application temperature.

The chemical combination of Al and Cr with oxygen instead of nitrogen gives rise for entirely different material properties, such as higher thermal stability even in oxidising environments. Al_2O_3 coatings applied to machining tools are capable of providing excellent wear protection and high hot hardness [53]. These coatings, either in hexagonal corundum-type α-structure or the metastable cubic κ-structure are typically grown by chemical vapour deposition (CVD) at temperatures between 800 and 1000 °C. The synthesis of $α-Al_2O_3$ coatings at temperatures below 700 °C by PVD is still challenging and the focus of many research activities [21,29,54,55,105]. Because, thereby also temperature-sensitive materials (e.g., high speed steels) could be protected. When reducing the growth temperature, many polymorphic structures of Al_2O_3 develop, which upon a subsequent thermal exposure phase-transform towards their thermodynamically stable structure $α-Al_2O_3$. Such phase transformation are typically connected with volume changes and thus, the generation of crack networks and spallation of the coating. The formation of $(Al,Cr)_2O_3$ solid solutions provides the possibility of significantly lowering the necessary deposition temperature to still form a single-phased corundum-type structured coatings. Chromium forms an isostructural α-type Cr_2O_3 with similar lattice parameters and a certain miscibility with $α-Al_2O_3$ [20]. Because there are no transient Cr_2O_3 phases (contrary to Al_2O_3), Cr_2O_3 stabilizes the corundum-type structure down to rather low deposition temperatures, depending on the Cr content [21,57]. However, the higher thermal stability of Al_2O_3 with respect to Cr_2O_3, still asks for as high Al-contents as possible (preferable in the corundum-type structure). The compromise between structure, high Al-content, and low deposition temperature (e.g., 500–600 °C for CAE) led to the development of coatings with metastable $(Al_xCr_{1-x})_2O_3$ phases [21,57,59–63]. This is a bit comparable to $Al_xCr_{1-x}N$ where CrN is used to stabilize the desired fcc structure, but the Al-content should be as high as possible. Consequently, combining excellent mechanical properties with excellent thermal stabilities would ask for a combination of high-Al-containing $Al_xCr_{1-x}N$ with high Al-containing $(Al_x,Cr_{1-x})_2O_3$.

Recently we showed, that multilayers composed of alternating $Al_xCr_{1-x}N$ and $(Al_x,Cr_{1-x})_2O_3$ layers can be developed (even in an industrial batch-type deposition system) with various oxide-nitride interface geometries and volume fractions (chapter 5).

Here, we focus on their thermal-stability and the role of their oxide-nitride interface geometry and volume fraction on phase transformations and structural modifications during annealing in vacuum and inert atmosphere up to 1500 °C.

6.2 Experimental

All coatings investigated were synthesised in an Oerlikon Balzers Innova batch-type cathodic arc evaporation system equipped with powder metallurgically (PM) prepared $Al_{0.7}Cr_{0.3}$ targets (Plansee Composite Materials GmbH). The low-alloyed steel foil, polycrystalline Al_2O_3, and Si (100) substrates were ultrasonically cleaned in acetone and ethanol for 10 minutes and then mounted on a two-fold rotation carousel with a minimum target-to-substrate distance of ~25 cm. The deposition chamber was heated to 500 °C by a combined radiation and plasma heating process for approximately 30 minutes. Ar ion etching, using the Balzers Central Beam Etching Technology, was performed for another 30 minutes, in order to remove any residuals and oxides from the substrate surfaces, and in further consequence to enhance adhesion.

Monolithically grown $(Al_xCr_{1-x})_2O_3$ were prepared by four $Al_{0.7}Cr_{0.3}$ cathodes operating 60 minutes with an arc current of 180 A and an oxygen flow rate of 1000 sccm (average process pressure of ~2.6 Pa) injected to the target surface. A negative substrate bias of -40 V (DC) was applied, in order to enhance growth kinetics. The multilayer coatings were prepared by alternatively processing two out of four active (six in total) neighbouring cathode positions in nitrogen and oxygen, respectively. For a detailed description of the deposition setup and multilayer architectures see chapter 5.2.

The thermal stability of our coatings was investigated by a combination of differential scanning calorimetry (DSC) and thermal gravimetric analysis (TGA) using a DSC-STA 449 F1 Jupiter®, calibrated with 7 elements (In, Sn, Bi, Zn, Al, Ag, Au). Dynamic measurements were carried out with a heating rate of 20 K/min up to 1500 °C in He atmosphere (protective=50 ml/min; purge=50 ml/min). In order to remove volatile contaminations, an isothermal measurement segment for 20 min at 150 °C within the equipment was applied. The crucibles for the powder samples are made of Pt-Ir alloy with an α-Al_2O_3 inlay. An empty crucible (inlay included) was utilized as reference sample. Powdered coating material was used in order to avoid substrate interference during the DSC - TGA measurements. Therefore, the coatings were chemically removed from their iron foil substrates by dissolving them in 35 % hydrochloride acid at 70 °C for approximately 30 min. The remaining film material was rinsed with acetone and manually ground to powder.

The coated polycrystalline Al_2O_3 substrates were annealed in a Centorr LF22-200 vacuum oven at annealing temperatures T_a ranging from 800 to 1500 °C in steps of 100 °C applying a heating rate of 20 K/min. The samples were hold at peak temperatures for 1 hour and cooling was performed passively (simply turning off the heater, which leads to cooling rates of ≥ 50 K/min down to 200 °C).

Chemical and morphological investigations of our coatings were carried out using a FEI Quanta 200 field emission gun scanning electron microscope (FEG SEM) with an EDAX energy dispersive X-ray spectroscopy (EDS) detector attached.

Information on the crystallographic composition was obtained by X-ray diffraction (XRD) in a Bragg-Brentano arrangement (BB: 2θ=15–90°) for annealed powder samples as well

as in grazing-incidence arrangement (GI: angle of incidence $\Omega=2°$, $2\theta=15–90°$) for the coatings on their substrates. Annealed coatings on Al_2O_3 substrates were analysed in an Empyrean PANalytical θ-θ diffractometer with a Cu K_α radiation source and a scintillation-detector.

More detailed examinations on the coating microstructure, were realised by transmission electron microscopy (TEM) including, scanning TEM (STEM), selected-area electron diffraction (SAED), and EDS), using a TECNAI F20 FEG TEM operated with an acceleration voltage of 200 keV and equipped with an EDAX Apollo XLT2 EDS detector.

The hardness (H) and indentation modulus (E) of our coatings grown on polycrystalline Al_2O_3 substrates in their as-deposited state and after annealing at $T_a=800–1500$ °C for 1 h in vacuum, were obtained by nanoindentation, using an Ultra-Micro-Indentation II system equipped with a Berkovich diamond tip. Normal loads ranging from 20 to 10 mN were applied and the indentation curves were evaluated according to Oliver and Pharr [88].

6.3 Results and discussion

6.3.1 Thermal stability and phase evolution

6.3.1.1 (Al,Cr)$_2$O$_3$ coatings

Energy-dispersive X-ray spectroscopy, carried out on monolithically grown (Al,Cr)$_2$O$_3$ on Si substrates reveal a chemical composition of (Al$_{0.74}$Cr$_{0.26}$)$_2$O$_3$ in the as-deposited state with an overall oxygen content of ~59 at.%, indicative for stoichiometric M$_2$O$_3$–type oxides. The increased Al-content as compared to the nominal target composition Al$_{0.7}$Cr$_{0.3}$ is typically observed for arc evaporated Al-Cr-O coatings in oxygen-rich conditions [55,99].
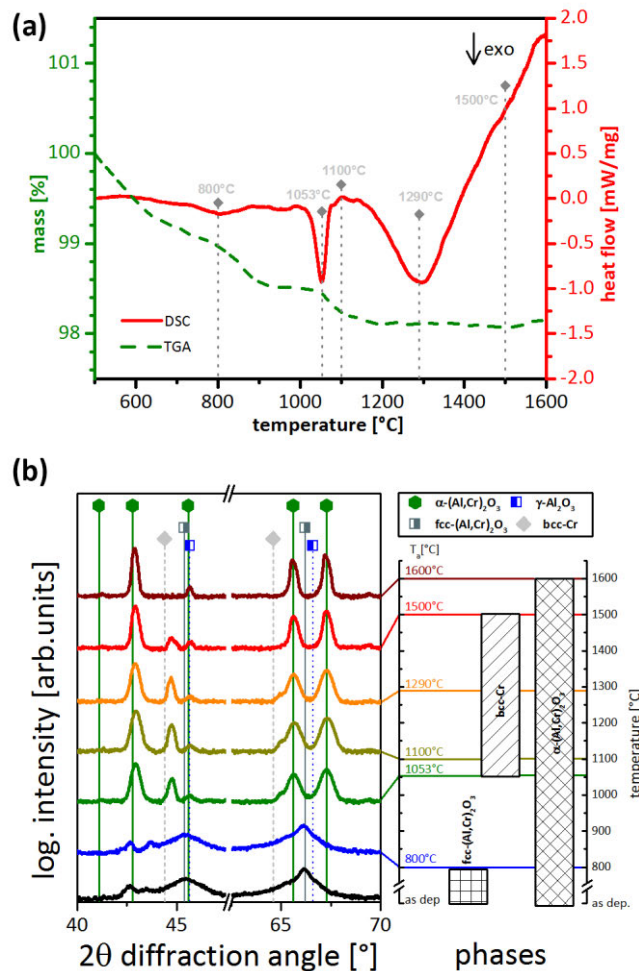
Fig. 6.1: (a) DSC/TGA and (b) XRD measurements (evolution) of (Al$_{0.74}$,Cr$_{0.26}$)$_2$O$_3$ powder samples, annealed in inert gas (He) atmosphere. The annealing temperatures are chosen based on distinct DSC and TGA features, indicated in (a). The bar chart next to the XRD patterns highlights their dominant phases.

The TGA signal of monolithically grown $(Al,Cr)_2O_3$, Fig. 6.1a, demonstrates a continuous mass loss of ~1 wt.% up to 800 °C. This might be related with evaporation of possible Al(Cr)-hydroxides, which possibly form during the substrate-dissolving-procedure in HCl. Also the formation of volatile chromium oxides can be lead to a mass loss as well, which will be discussed in detail in the next section. However, the two discrete TGA features (with 0.5 and 0.33 wt.% steps) in the temperature range 750–950 °C and 1000–1150 °C, coincide with the first two distinct DSC features in these temperature regions, Fig. 6.1a. The structural evolution of our coatings annealed at these distinct temperatures, marked in Fig. 6.1a, highlights the formation of corundum-type $(Al_xCr_{1-x})_2O_3$ solid solution and metallic bcc-Cr, Fig. 6.1b. The peak positions of the corundum-type $(Al_xCr_{1-x})_2O_3$ solid solution were calculated from the α-Al_2O_3 (ICDD #00-046-1212, corundum) and α-Cr_2O_3 (ICDD #00-038-1479, eskolaite) standard for a replacement of 30 % Al^{3+} by Cr^{3+} cations. In the as-deposited state the XRD pattern of our $(Al,Cr)_2O_3$ coating exhibits fractions of α-$(Al,Cr)_2O_3$ and fcc-$(Al,Cr)_2O_3$. The latter is identified by broad XRD peaks at $2\theta \approx 45.4°$ (200) and 66.2° (220) [63,67], in good agreement with literature reports about metastable cubic structured $(Al,Cr)_2O_3$. The fine-grained character is characteristic for cubic structured $(Al,Cr)_2O_3$ phases, whereas the corundum-type phase is typically coarser-grained, as obtain from detailed TEM studies of coatings containing both phases [55]. During annealing to 800 °C, the full-width-at-half-maximum of the (200) XRD peak of fcc-$(Al,Cr)_2O_3$ reduces by ~10 % suggesting recovery effects (where structural built-in defects, like point and line defects, arrange to lower-energy sites) and grain coarsening. After annealing at T_a = 1053 °C no metastable fcc-$(Al,Cr)_2O_3$ phase can be detected anymore (but pronounced α-$(Al,Cr)_2O_3$ XRD peaks), suggesting for a complete transformation into corundum-type α-$(Al,Cr)_2O_3$. Furthermore, two additional XRD peaks at $2\theta \approx 44.7°$ and 64.9° indicate the formation of metallic bcc-Cr or Cr-rich Cr(Al) solid solutions (due to the offset to higher 2θ diffraction angles of these XRD peaks from the standar bcc-Cr position). The intensity of this XRD peaks is high for T_a = 1053, 1100, 1290 °C, but decreases for higher temperatures and after annealing to 1600 °C no metallic Cr or Cr(Al) can be detected anymore.

6.3.1.2   (Al,Cr)N/(Al,Cr)$_2$O$_3$ coatings

DSC/TGA

The chemical composition of our multilayers corresponds to $Al_{0.68}Cr_{0.32}N/(Al_{0.74}Cr_{0.26})_2O_3$, based on chemical investigations of individually prepared $Al_{0.68}Cr_{0.32}N$ and $(Al_{0.74}Cr_{0.26})_2O_3$ coatings using the same deposition system and setup as used for the individual layer segments of our multilayers. With increasing number of bilayers from 12 to 25 to 50 (per comparable coating thickness, thus the volume fraction of nitride-oxide interfaces increases), not only the bilayer period λ decreases from ~170 to 80 to 40 nm but also the overall oxygen content increases (see chapter 5.3.1).

The influence of the volume fraction (i.e., by the number of bilayers, 12, 25, and 50) as well as the architecture (i.e., distinct, hybrid, and blurred) of the nitride-oxide interfaces

on the thermal stability of our $(Al,Cr)N/(Al,Cr)_2O_3$ multilayer coatings is presented in Fig. 6.2 by DSC and TGA curves. Thereby, Fig. 6.2a, b, and c show the influence of the volume fraction (by 12, 25, and 50 bilayers) for multilayers with distinct, hybrid and blurred nitride-oxide interfaces, respectively; and Fig. 6.2d, e, and f show the influence of the architecture (by distinct, hybrid, and blurred interfaces) for multilayers with 12, 25, and 50 bilayers, respectively. These comparative figures clearly highlight, that the volume fraction of the nitride-oxide interfaces has a stronger influence on the thermal stability than their architecture. With increasing volume fraction of the nitride-oxide interfaces (i.e., from 12 to 25 to 50 bilayers) the thermal stability always significantly increases for our $(Al,Cr)N/(Al,Cr)_2O_3$ multilayers having either distinct (Fig. 6.2a), hybrid (Fig. 6.2b), or blurred (Fig. 6.2c) type interfaces. But, the dependence of the thermal stability on the interface type is different for our multilayers with 12, 25, and 50 bilayers. While changing the nitride-oxide interface type from hybrid to blurred to distinct increases the thermal stability of our multilayers with 12 bilayers (Fig. 6.2d) and 25 bilayers (Fig. 6.2e), it decreases for our multilayers with 50 bilayers (Fig. 6.2f) from hybrid (or distinct) to blurred. Consequently, the multilayers with hybrid-type interface always (i.e., for 12, 25, and 50 bilayers) show the lowest thermal stability. But, the thermal stability of our multilayers with blurred-type interfaces is close to be lowest for 12 bilayers, close to be highest for 25 bilayers, and highest for 50 bilayers. Hence, the thermal stability most significant increases with the volume fraction of blurred-type nitride-oxide interfaces (i.e., from 12 to 25 to 50 bilayers).
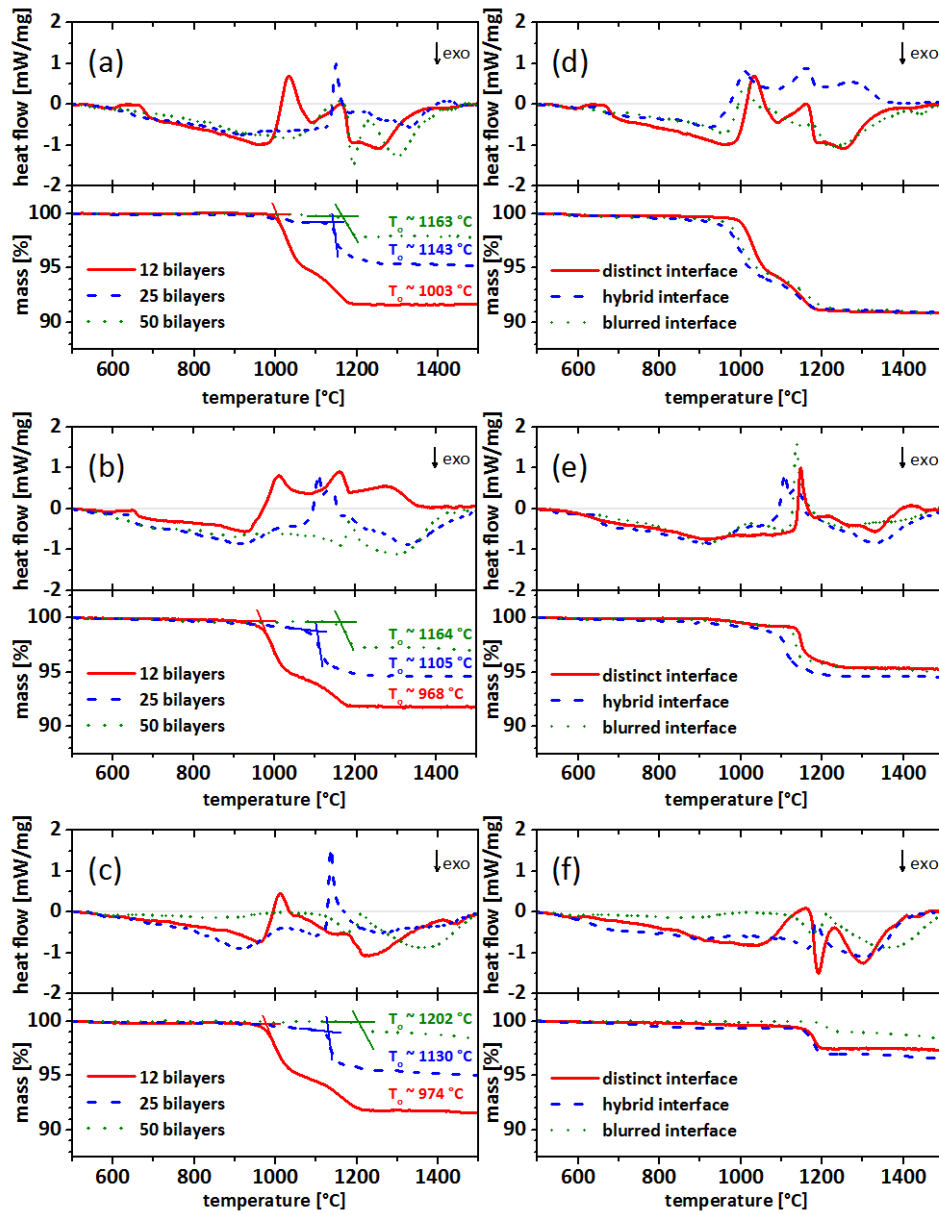
Fig. 6.2: DSC and TGA signals of our AlCrN/(Al,Cr)$_2$O$_3$ multilayer coatings with different volume fraction (number of bilayer) and architecture of their nitride-oxide interfaces. (a), (b), and (c) show the impact of the volume fraction (12, 25, or 50 bilayers) for distinct, hybrid, and blurred nitride-oxide interfaces, respectively. (d), (e) and (f) show the impact of the architecture (distinct, blurred, and hybrid) for 12, 25, and 50 bilayers, respectively.

Based on previous investigations on Al$_x$Cr$_{1-x}$N coatings [30,31,33,52,106], in combination with results obtained for (Al,Cr)$_2$O$_3$ (see previous section, Fig. 6.1) we can conclude that the exothermic DSC features up to ~900 °C of our different (Al,Cr)N/(Al,Cr)$_2$O$_3$ multilayers (different quantity and quality of nitride-oxide interfaces), basically stem from recovery processes of deposition-induced structural defects. The exothermic DSC features above ~1200 °C are basically due to grain growth, recrystallization, and/or sintering processes of our powder coating materials. The endothermic features, which

are always accompanied with a distinct mass-loss, stem from the dissociation of Cr–N bonds, to form Cr_2N and finally Cr (under N_2-release) [30,106]. This two-stage dissociation sequence is nicely represented by two endothermic features and the two distinct mass-loss features for our $(Al,Cr)N/(Al,Cr)_2O_3$ multilayers with 12 bilayers (Fig. 6.2a, b, c, and d). The quality of the nitride-oxide interfaces (i.e., weather it is distinct, blurred, or hybrid) has only a minor influence (Fig. 6.2d). However, the 12-bilayer-containing $(Al,Cr)N/(Al,Cr)_2O_3$ multilayer with distinct interfaces shows a slightly higher onset temperature for the first endothermic feature and the connected first distinct mass-loss step, than the other 12-bilayer-containing $(Al,Cr)N/(Al,Cr)_2O_3$ multilayers, see Fig. 6.2d.

Contrary to the $(Al,Cr)N/(Al,Cr)_2O_3$ multilayers composed of 12 bilayers, those composed of 50 bilayers basically show only one significant endothermic feature and one distinct mass-loss step, see Fig. 6.2f. The multilayers composed of 25 bilayers exhibit a behaviour somehow in-between these, see Fig. 6.2e. The increasing number of bilayers, and in particular the increasing number of oxide layers, act as diffusion barriers against the outward diffusion of nitrogen (from the decomposition and dissociation of $Al_xCr_{1-x}N$ towards w-AlN and bcc-Cr, under N_2-release). Thereby, the endothermic feature as well as the first significant mass-loss step shifts to higher temperatures, this is nicely presented in Fig. 6.2a, b, and c for distinct, hybrid, and blurred nitride-oxide interfaces, respectively. Thus, not only the onset temperature for this mass-loss can be shifted by ~200 °C to higher temperatures when increasing the number of interfaces from 12 to 50, but also the total mass-loss (at the maximum test temperature of 1500 ° C, for the multilayers) can be significantly reduced. For example, this onset temperature increases from 968 to 1164 °C and the total mass-loss decreases from9.1 to 3.4 wt.% for the multilayers with hybrid nitride-oxide interfaces, Fig. 6.2b.

The influence of the nitride-oxide interface architecture (i.e., distinct, hybrid, or blurred) on the thermal stability of our $(Al,Cr)N/(Al,Cr)_2O_3$ multilayers with highest thermal stability (i.e., 50 bilayers) is presented by DSC and TGA curves in Fig. 6.2f. The onset temperature for the distinct mass-loss increases from ~1165 to 1200 °C when changing the interface architecture from distinct (or hybrid) to blurred. The total mass-loss decreases from 3.4 to 2.7 to 1.6 wt.%, when changing the interface architecture from hybrid to distinct to blurred, respectively. Consequently, the $(Al,Cr)N/(Al,Cr)_2O_3$ multilayer coating with highest volume fraction (i.e., 50 bilayers) of blurred-type nitride-oxide interfaces exhibits the highest thermal stability, see the green dotted lines in Fig. 6.2c and f. Due to the significant endothermic reactions (caused by the decompositions and dissociation of the $Al_xCr_{1-x}N$ layers towards w-AlN and bcc-Cr, under N_2-release) the exothermic reaction due to the phase transformation of the $(Al,Cr)_2O_3$ layers towards their stable corundum-type α-$(Al,Cr)_2O_3$ structure can hardly be identified.

To follow the structural changes of our coatings during these DSC and TGA measurements, they were annealed in inert gas (He) atmosphere at distinct temperatures (derived from significant features of their DSC and TGA curves).

Structure evolution of multilayers with distinct-type interfaces

All $(Al,Cr)N/(Al,Cr)_2O_3$ multilayers with distinct-type interfaces crystallise in a face-centred cubic structure see the XRD patterns at the bottom of Fig. 6.3a, b, and c. Individual XRD peaks for $Al_xCr_{1-x}N$ and $(Al_xCr_{1-x})_2O_3$ phases can only be detected for the multilayers with lowest volume fraction of nitride-oxide interfaces (i.e., 12 bilayers), Fig. 6.3a. Hence, where the individual $Al_xCr_{1-x}N$ and $(Al_xCr_{1-x})_2O_3$ layers are also thickest. Annealing this multilayers to T_a = 950 °C leads to a broadening of the fcc-$(Al,Cr)_2O_3$ peaks (indicated by half-filled grey squares in Fig. 6.3a) as well as an increased background at 2θ positions 31.6, 37.2, 39.0, and 60.2°. These modifications are not pronounced but indicate the transformation of the metastable fcc-$(Al_xCr_{1-x})_2O_3$ layers towards α-$(Al,Cr)_2O_3$. The corresponding DSC signal features an exothermic peak at ~950°C (Fig. 6.2a, red solid line). Increasing the annealing temperature to T_a = 1090 °C clearly leads to the phase formation of α-$(Al,Cr)_2O_3$, γ-$(Al,Cr)_2O_3$, w-AlN, hcp-$(Cr,Al)_2N$, and bcc-Cr; see the solid green hexagons, the half-filled blue squares, the half-filled black hexagons (2θ = 32.9°), the half-filled orange hexagons (2θ = 40.6, 43.0, and 56.5°) and the solid grey diamonds (2θ = 44.4 and 64.6°) indicating these phases in Fig. 6.3a. The corresponding DSC curve shows an endothermic heat flow feature (peak temperature of 1035 °C) and there is also a distinct mass-loss step, which is connected with the dissociation of Cr–N bonds towards bcc-Cr via N_2 release.

When increasing the annealing temperature further to T_a = 1150 °C, the intensities of the XRD peaks for α-$(Al,Cr)_2O_3$ and bcc-Cr increases, while those for fcc-$(Al,Cr)_2O_3$ and hcp-$(Cr,Al)_2N$ decrease. Hence, Cr_2N-based phases further dissociate towards bcc-Cr and fcc-$(Al,Cr)_2O_3$ as well as γ-$(Al,Cr)_2O_3$ further transform to α-$(Al,Cr)_2O_3$. After annealing at T_a = 1250 °C only α-$(Al,Cr)_2O_3$ and bcc-Cr phases can be detected, see Fig. 6.3a. Thus, the metastable fcc-$(Al,Cr)_2O_3$ layers fully transformed to α-$(Al,Cr)_2O_3$ (via the formation of small fractions of γ-$(Al,Cr)_2O_3$ as well), and the $(Al,Cr)N$ layers fully decomposed and dissociated to bcc-Cr (via the intermediate formation of hcp-$(Cr,Al)_2N$ based phases). Our XRD results further suggest, that the w-AlN phases – presented at temperatures between 1090 and 1250 °C due to the decomposition of fcc-$(Al,Cr)N$ – are fully integrated in the α-$(Al,Cr)_2O_3$ phases. Important to mention is further, that the γ-$(Al,Cr)_2O_3$ and α-$(Al,Cr)_2O_3$ phases are rather γ-Al_2O_3 and α-Al_2O_3 (as there is no offset in the XRD peak position from the standard position of γ-Al_2O_3 and α-Al_2O_3, see Fig. 6.3a). We envision, that this is because the transformation of the metastable fcc-$(Al,Cr)_2O_3$ is accompanied with the decomposition of fcc-$(Al,Cr)N$ to form bcc-Cr.

The structural development of the $(Al,Cr)N/(Al,Cr)_2O_3$ multilayers with 25 bilayers is very similar, only that the individual transformations are slightly shifted to higher temperatures, please compare Fig. 6.3b and a. An additional difference is also, that the formed α-Al_2O_3-based phases contain more Cr, indicated by the larger offset of the XRD peaks to lower diffraction angles (hence, larger lattice parameters due to the incorporated of Cr).

The XRD investigations are in agreement with corresponding DSC and TGA measurements, indicating higher thermal stability and lower mass-loss as compared with the multilayer composed of 12 bilayers. Thus, even after annealing the 25-bilayer-multilayers at T_a = 1500 °C, still hcp-(Cr,Al)$_2$N phases can be detected next to α-(Al,Cr)$_2$O$_3$, and bcc-Cr, see Fig. 6.3b.

The XRD measurements of our 50-bilayer-containing multilayers support the DSC and TGA investigations, which an even higher thermal stability and further reduced mass-loss up to 1500 °C (as compared with the 25-bilayer-contoining multilayer).

Even after annealing the 50-bilayer-multilayer at T_a = 1500 °C, only rather small bcc-Cr fractions next to α-(Al,Cr)$_2$O$_3$ and significant hcp-(Cr,Al)$_2$N phase fractions can be detected by XRD, Fig. 6.3c. Here, the XRD peaks for α-(Al,Cr)$_2$O$_3$ exhibit an even more pronounced offset to smaller diffraction angles from the standard α-Al$_2$O$_3$ position (towards α-Cr$_2$O$_3$) than 25-bilayer-multilayer. Hence, more Cr is present in these α-(Al,Cr)$_2$O$_3$ phases than in those of the 12- and 25-bilayer-containing multilayers, compare Fig. 6.3a, b, and c.
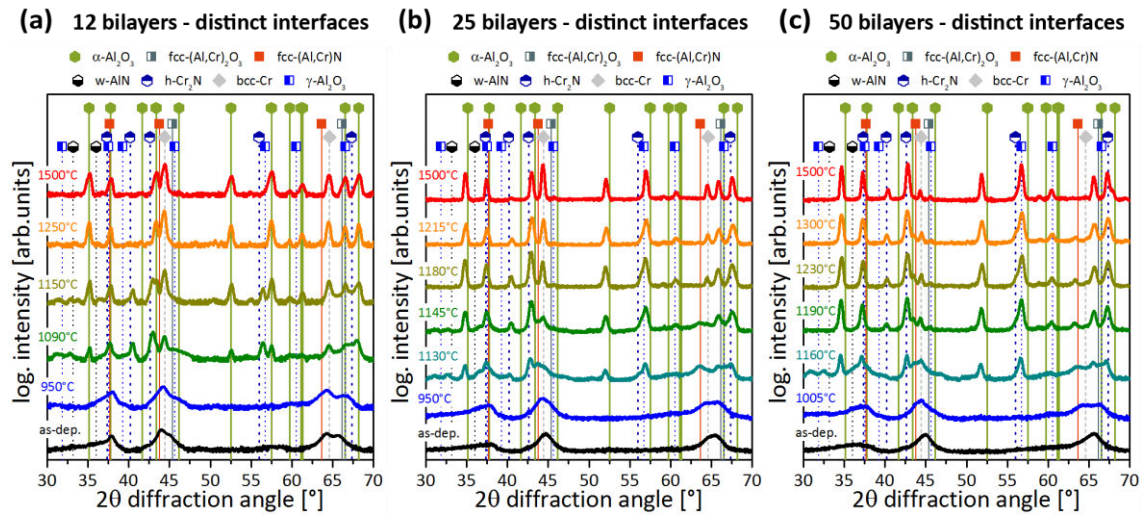
Fig. 6.3: Powder XRD evolution of AlCrN/(Al,Cr)$_2$O$_3$ multilayer coatings with (a) 12, (b) 25, and (c) 50 bilayers with distinct interfaces respectively.

Structure evolution of multilayers with blurred-type interfaces

The multilayers with blurred-type nitride-oxide interfaces, which indicate highest thermal stability during the DSC and TGA investigations, Fig. 6.2, are single-phase face-centred cubic structured in the as deposited state, see the XRD patterns at the bottom of Fig. 6.4a. With increasing volume fraction of these interfaces, hence with increasing number of bilayers from 12 (Fig. 6.4a) to 50 (Fig. 6.4c), also the XRD peak widths increase. This suggest for decreasing coherently diffracting domain sizes (in agreement with the smaller individual (Al,Cr)N and $(Al,Cr)_2O_3$ layer thickness). As already indicated by the DSC and TGA measurements, the onset temperature for N_2-release (first significant endothermic feature and mass-loss) increases with the volume fraction of the nitride-oxide interfaces (hence, from 12 to 25 to 50 bilayers). Therefore, the formation of hcp-$(Cr,Al)_2N$ phases (due to the decomposition of fcc-(Al,Cr)N towards w-AlN and $(Cr,Al)_2N$ via N_2-release) is shifted to higher temperatures, $T_a = 1010, 1135, 1200\,°C$, with increasing number of bilayers from 12 to 25 to 50. Furthermore, also the maximum temperature until hcp-$(Cr,Al)_2N$ phases can be detected increases with the bilayer number. Therefore, also the phase fraction of bcc-Cr (indicated by the corresponding XRD peak intensities) after annealing at 1500 °C significant decreases with the bilayer number, compare Fig. 6.4a, b, and c. This is in agreement with the significantly reduced mass-loss of the coatings, when increasing, when increasing their amount of bilayers (Fig. 6.2c). The further important structural change is the formation of α-$(Al,Cr)_2O_3$ phases, which can be detected after annealing the 12-, 25-, and 50-bilayer-containing multilayers at 1155, 1095, and 1175 °C. Consequently, as obtained for the $(Al,Cr)_2O_3$ coating (Fig. 6.1), the metastable fcc-$(Al,Cr)_2O_3$ or γ-$(Al,Cr)_2O_3$ phases transform to α-$(Al,Cr)_2O_3$ at ~ 1100 °C.
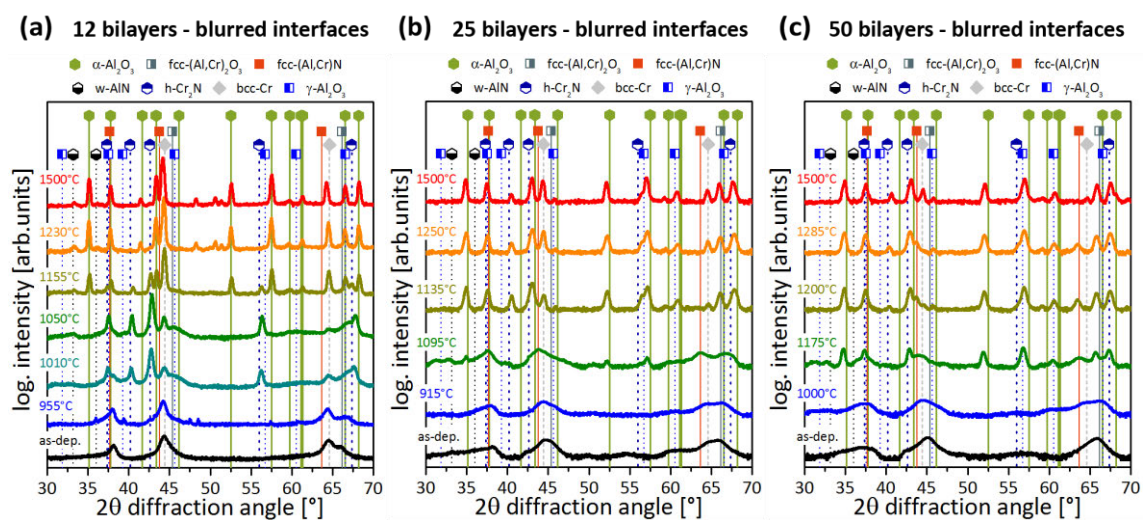
Fig. 6.4: Powder XRD evolution of AlCrN/$(Al,Cr)_2O_3$ multilayer coatings with (a) 12, (b) 25, and (c) 50 bilayers consisting of blurred interfaces respectively.

6.3.2 Morphology and microstructures

6.3.1.1 (Al,Cr)$_2$O$_3$ coatings

The SEM fracture cross section of our as-deposited (Al$_{0.76}$Cr$_{0.24}$)$_2$O$_3$ coating (on polycrystalline Al$_2$O$_3$ substrates) shows a dense columnar growth morphology, Fig. 6.5 a. Contrary to the powder XRD patterns (Fig. 6.1), XRD investigations of these coatings on their Al$_2$O$_3$ substrate (Fig. 6.5 b) do not show any significant fcc-(Al,Cr)$_2$O$_3$ phases in the as deposited state, due to the rather strong substrate peaks. The first significant coating XRD peaks can be detected for T$_a$ = 900 °C, which indicate the formation of α-(Al,Cr)$_2$O$_3$, Additionally, the small XRD peak at 2θ~44.5° suggest the formation of bcc-Cr, as obtained for the powder XRD studies of these coatings (Fig. 6.1). With increasing temperature up to 1200 °C, thee XRD peaks increase in intensity, and for even higher temperatures they also shift their position towards α-Al$_2$O$_3$, see Fig. 6.5 b. This suggests for an enrichment of the (Al,Cr)$_2$O$_3$ solid solution with Al. As no additional phases can be detected (hence, suggesting the loss of Cr by the formation of volatile Cr-oxides), we performed more detailed TEM investigations of these coatings annealed after 900, 1300, and 1500 °C.
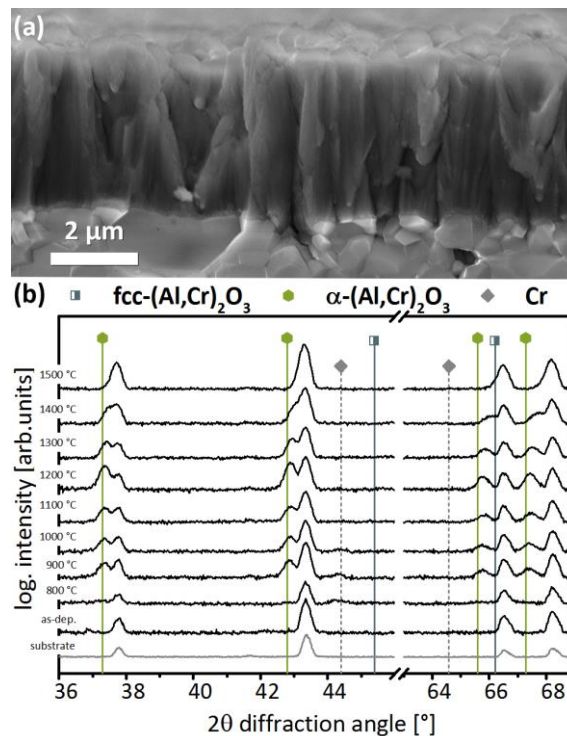
Fig. 6.5: (a) Cross-sectional SEM (as-deposited) image and (b) XRD measurements of as-deposited as well as annealed at T$_a$=800–1500 °C (in 100 °C steps) in vacuum for 1 h, monolithically grown (Al,Cr)$_2$O$_3$.

Bright field cross sectional TEM invastigations of the coating after annealing at 900 °C for 5 min, Fig. 6.6a and b, reveal a fine-columnar underdense microstructure, which is dominated by metastable cubic $(Al,Cr)_2O_3$ solid solutions, see the SAED inset of Fig. 6.6 b. The morphology of the coating is not significantly influenced by the annealing at 900 °C, and also no corundum-type phase can be detected (in the substrate near region). Higher magnifications (Fig. 6.6c and d) not only reveal the presence of incorporated spherical and flat-shaped macroparticles, but also thermally-induced diffusion-zones indicated by speckled features (areas) around them.
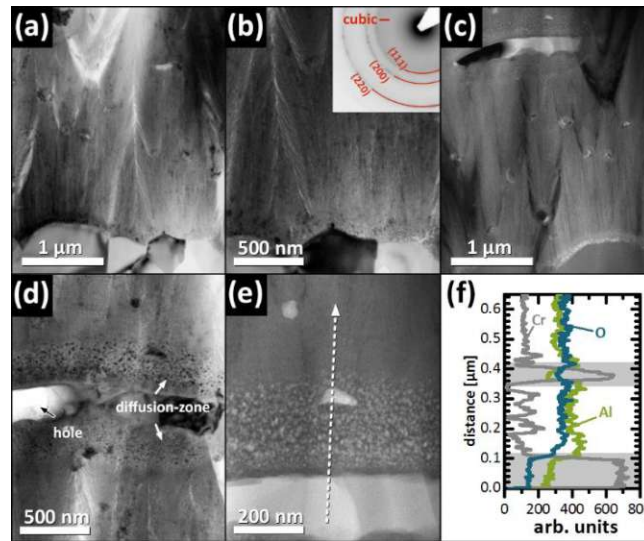
Fig. 6.6: (a) Cross-sectional TEM overview, (b) SAED substrate near region, (c) STEM overview, (d) TEM-BF image of droplet, (e) STEM image and (f) EDS-linescan of droplet of annealed $(Al,Cr)_2O_3$ at T_a=900 °C in vacuum for 5 min.

The enhanced thermal stability of the oxide coating as compared to metallic or intermetallic material is nicely shown by the thermally-induced decomposition of the example of the flat-shaped intermetallic droplet, see the TEM BF and STEM images in Fig. 6.6d and e, respectively. The dashed white line in Fig. 6.6e indicates the direction of the EDS line-scan which is provided in Fig. 6.6f. The bright appearing features indicate Cr-enrichments (dark grey line) whereas the darker surrounding represents the oxide coating consisting of Cr, Al (green line), as well as oxygen (blue line).

By annealing our $(Al,Cr)_2O_3$ coatings in vacuum for 1 h at 1300 °C (Fig. 6.7a, b, and c) and 1500 °C (Fig. 6.7d, e, and f), their structure significant coarsened and all metastable phases transformed to corundum-type solid solutions. Although, EDS has some uncertainties, especially for light elements (explaining the rather low oxygen content) the loss in Cr is significant, when compare the sample annealed after 1300 and 1500 °C, Fig. 6.7c and f, respectively. Thus these studies support our suggestion based on the XRD studies (Fig. 6.5), that especially at higher temperatures also volatile Cr-oxides can be formed, leading to the shift of the XRD position of α-$(Al,Cr)_2O_3$ towards α-Al_2O_3, due to the loss of Cr-oxides.
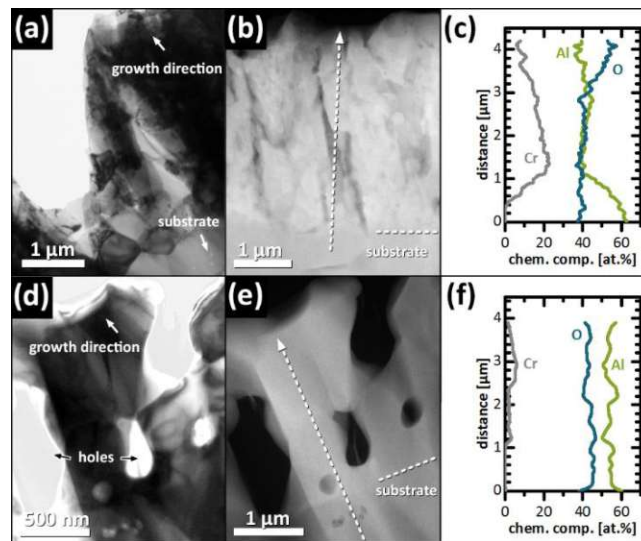
Fig. 6.7: (a) Cross-sectional TEM BF image, (b) and (c) STEM and corresponding EDS line-scan of $(Al,Cr)_2O_3$ after annealing at T_a=1300 °C for 1 h. (d) Cross-sectional TEM BF image, (e) STEM overview with corresponding EDS line-scan (f) of annealed $(Al,Cr)_2O_3$ at T_a=1500 °C in vacuum for 1 h.

6.3.3 Thermo-Mechanical properties

Detailed investigations of the mechanical properties (indentation hardness and modulus), after vacuum-annealing up to 1500 °C, are conducted on the $(Al_{0.76}Cr_{0.24})_2O_3$ coating (to have a reference) and on four different $(Al,Cr)N/(Al_{0.76}Cr_{0.24})_2O_3$ multilayers. For the multilayers we selected those with 12 bilayers having different nitride-oxide interface types (distinct, hybrid, and blurred), and the multilayer with the highest thermal stability – 50-bilayer-containing $(Al,Cr)N/(Al,Cr)_2O_3$ with blurred nitride-oxide interfaces – see Fig. 6.8.

The hardness of our $(Al,Cr)_2O_3$ reference coating (half-filled black hexagons in Fig. 6.8) initially decreases with increasing annealing temperature from ~4.2±1 GPa (as-deposited value) to ~2.3±1 GPa (T_a = 1000 °C). The rather low as-deposited hardness value is due to the rather low and non-pulsed substrate bias of – 40 V (in combination with an insulating substrate). These conditions were also used for the $(Al,Cr)N/(Al,Cr)_2O_3$ multilayers, and selected to increase the impact of the volume fraction and nature of the nitride-oxide interfaces, and to increase the impact of the crystal structure. In our previous study we showed that the difference (in mechanical properties) between the $(Al,Cr)N/(Al,Cr)_2O_3$ multilayers decreases with increasing number of bilayers (see chapter 5.3.3). As obtained by DSC/TGA and XRD studies, basically, recovery effects take place in our $(Al,Cr)_2O_3$ coatings upon annealing to ~1000 °C, explaining the observed hardness decrease. With the onset of significant α-$(Al,Cr)_2O_3$ formation (at ~1000 °C, see Fig. 6.1), also the hardness exhibits a significant increase to ~5 GPa, which stays there up to even 1500 °C. A corresponding dependence is obtained for the indentation modulus, yielding an increase by the transformation to α-$(Al,Cr)_2O_3$ from ~100 to 150 GPa, see Fig. 6.8.

Also for the $(Al,Cr)N/(Al,Cr)_2O_3$ multilayers, the impact of the α-$(Al,Cr)_2O_3$ formation on the hardness is most pronounced for those having the lowest hardness values at these temperature ranges. This clearly shows, in agreement with the DSC/TGA and XRD studies, that the significant formation of α-$(Al,Cr)_2O_3$ phases is at ~100 °C higher temperatures in the $(Al,Cr)N/(Al,Cr)_2O_3$ multilayers than in the $(Al,Cr)_2O_3$ coatings. The comparison of the 12-bilayer-containing multilayers nicely shows, that while those with distinct-type nitride-oxide interfaces have highest as-deposited hardness, this hardnening-effect is already lost after annealing at 800–900 °C, see Fig. 6.8.

The hardness of these 12-bilayer-containing multilayers is rather similar after annealing at $T_a \geq$ 900 °C. The temperature-dependent behaviour of their indentation-moduli is comparable to that of their hardness.

The multilayer with the highest thermal stability – the 50-bilayer-containing $(Al,Cr)N/(Al,Cr)_2O_3$ with blurred nitride-oxide interfaces – also shows the highest hardness with $T_a \geq$ 800 °C, see Fig. 6.8. Their hardness is relatively constant at ~10 GPa up to T_a = 1300 °C, then it even increases to ~17 GPa with T_a = 1500 °C. Based on our DSC/TGA, XRD, and hardness investigations we can conclude that althought their fcc-

(Al,Cr)N layers decompose and dissociate to form hcp-$(Cr,Al)_2N$ via N_2-release, the transformation of their fcc-$(Al,Cr)_2O_3$ layers towards α-$(Al,Cr)_2O_3$ effectively helps to keep their hardness relatively constant up to 1300 °C. The further Al-enrichment of α-$(Al,Cr)_2O_3$ towards α-Al_2O_3 (via the formation of volatile Cr-oxides, see Fig. 6.7) during annealing at even higher temperatures is responsible for the obtained hardness and indentation moduli increase.
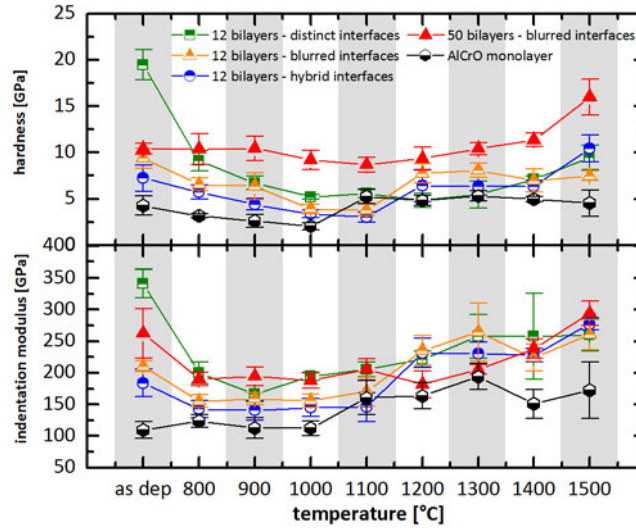
Fig. 6.8: Hardness and indentation modulus of monolithically grown $(Al,Cr)_2O_3$ (black half-filled hexagons), as well as $(Al,Cr)N/(Al,Cr)_2O_3$ multilayer coatings with 12 bilayers and blurred (orange half-filled triangles), hybrid (blue half-filled circles), distinct interfaces (green half-filled squares), as well as 50 bilayers with blurred interfaces (red filled triangles).

6.4 Summary and conclusions

Monolithically grown $(Al_xCr_{1-x})_2O_3$ as well as $Al_xCr_{1-x}N/(Al_xCr_{1-x})_2O_3$ multilayer coatings were arc evaporated using powder metallurgically prepared $Al_{0.7}Cr_{0.3}$ targets. These coatings were studied in detail for their thermal stability, and their phase evolution during annealing. While for annealed powdered $(Al_xCr_{1-x})_2O_3$, the metastable face centred cubic $(Al,Cr)_2O_3$ phase transforms into the corundum-type $(Al,Cr)_2O_3$ solid solution at ~1050 °C, which remains stable up to 1600 °C, a significant change of the latter was found for $(Al_xCr_{1-x})_2O_3$ deposited on Al_2O_3 substrates after annealing at elevated temperatures for 1 h. Dissociation of the corundum-type $(Al,Cr)_2O_3$ solid solution to α-Al_2O_3 and transient chromium oxides can be approved by XRD and TEM investigations.

According to DSC/TGA results we can conclude that, in the case of the multilayers, the thermal stability increases, with higher number of bilayers, regardless of their interface types (distinct and blurred). The decomposition of CrN into h-Cr_2N and further to c-Cr, via N_2 release, can be therefore retarded up to ~1200 °C.

Based on our results we can conclude that a multi-layer arrangement with optimized bilayer period is superior to the monolithically grown $Al_xCr_{1-x}N$ and $(Al_xCr_{1-x})_2O_3$ counterparts, deposited under similar conditions.

CHAPTER **7**

7. Thermal Stability of Arc Evaporated Al-Cr-O-N Coatings

7.1 Introduction

Metal oxynitride coatings in general have recently attracted considerable attention due to their special physical and chemical properties, which make them promising candidates for new applications [107–118]. Here, especially the development of Al-Cr-based oxynitrides, has gained enormous interest as protective hard coatings in the last decades [61,65–68]. Their specific properties arise from their special mixture of ionic and covalent bonding contributions. When nitrogen substitutes for oxygen (or vice versa) at the non-metallic sublattice, maintaining a global charge neutrality (because $2N^{3-} = 3O^{2-}$) promotes the formation of vacancies, and/or interstitials or forces the metal ions to change their valance state, which directly influences the bonding states. For example Najafi et al. [67] reported that the substitution of nitrogen by oxygen leads to a decrease of the cubic lattice parameter a, due to the formation of an $Al_xCr_{1-x}(O_yN_{1-y})$ solid solutions with vacancies on the metallic sublattice. The maximum oxygen content of the non-metallic sublattice to still prepare single-phased face centred cubi (fcc)-structured solid solutions can be as high as 97 at.%, depending on the deposition conditions. But for more than 60 at.% oxygen the hardness decrease from approximately 31.5±1.5 GPa ($Al_xCr_{1-x}N$) to 25.5±1 GPa, due to changed primary bonding contributions [67]. The high affinity of oxygen to the metallic species requires a rather high nitrogen content (of the reactive atmosphere during deposition) prepare oxynitride coatings with a high nitrogen content. Oxynitrides easily form with relatively low O_2 contents of the reactive N_2+O_2 gas atmosphere [71]. Although, considerable research activities were carried out with the focus on quaternary Al-Cr-O-N hard coatings (driven by the possibility to stabilise the fcc structure even for high Al contents), only little is known about their thermal stability and phase evolution during annealing at elevated temperatures. Therefore, we developed $(Al_xCr_{1-x})(O_{1-y}N_y)$ coatings with different N-to-O ratios, y, and studied their thermal stability (during annealing in inert atmosphere up to 1500 °C) using a combination of differential scanning calorimetry (DSC) and thermogravimetric analyses (TGA) with subsequent X-ray diffraction (XRD).

7.2 Experimental

All coatings investigated were synthesised in an Oerlikon Balzers Innova batch-type cathodic arc evaporation system equipped with powder metallurgically (PM) prepared $Al_{0.7}Cr_{0.3}$ targets (Plansee Composite Materials GmbH). The substrates, low alloyed iron steel foil, polycrystalline Al_2O_3 and Si (100) stripes ($20x7x0.4$ mm³), were ultrasonically cleaned in acetone and ethanol for 10 minutes and then mounted on a two-fold rotation carousel with a minimum target-to-substrate distance of approximately 25 cm. The deposition chamber was heated to 500 °C by a combined radiation and plasma heating process for approximately 30 minutes. Ar ion etching, using the Balzers Central Beam Etching Technology, was performed for another 30 minutes, in order to remove any residuals and oxides from the substrate surfaces, and in further consequence to enhance adhesion.

One $(Al_x,Cr_{1-x})N–(Al_x,Cr_{1-x})_2O_3–(Al_x,Cr_{1-x})N$ gradient-coating (transition from a nitride to an oxide and back to a nitride), five different $(Al_xCr_{1-x})(O_{1-y}N_y)$ oxynitride coatings, as well as the corresponding $(Al_x,Cr_{1-x})N$ and $(Al_x,Cr_{1-x})_2O_3$ coatings were deposited with four $Al_{0.7}Cr_{0.3}$ targets operated for 60 minutes with a constant arc current of 180 A. The oxynitride coatings were prepared with N_2/O_2 reactive gas mixtures of either 90/10, 85/15, 80/20, 75/25 or 70/30 at a pressure of 2.8 ± 0.7 Pa. The gradient-coating was prepared by constantly decreasing the nitrogen flow rate from 1000 to 0 sccm, while increasing the oxygen flow rate from 0 to 1000 sccm (within 30 min), and decreasing the oxygen flow back from 1000 to 0 sccm, while increasing the nitrogen flow rate from 0 to 1000 sccm (within another 30 min). In order to enhance growth kinetics, a negative substrate bias of -40 V DC was used for all coatings prepared.

Chemical and morphological investigations of our coatings were carried out using a FEI Quanta 200 Field Emission Gun Scanning Electron Microscope (FEG SEM) with an Energy Dispersive X-Ray Spectroscopy (EDS) detector attached.

The morphology, chemistry, and microstructure od the gradient-coating was investigated in detail by transmission electron microscopy (TEM) including high resolution TEM (HR-TEM), scanning TEM (STEM), selected-area electron diffraction (SAED), and EDS, using a TECNAI F20 FEG TEM operated with an acceleration voltage of 200 keV with an EDAX Apollo XLT2 EDS detector attached.

The thermal stability of our coatings was investigated by a combination of DSC and TGA using a DSC-STA 449 F1 Jupiter®, calibrated with 7 elements (In, Sn, Bi, Zn, Al, Ag, Au). The dynamical measurements were carried out with a heating rate of 20 K/min up to 1500 °C in flowing He atmosphere (protective=50 ml/min; purge=50 ml/min). In order to remove volatile contaminations, an isothermal annealing for 20 min at 150 °C was conducted. The crucibles for the powder samples are made of Pt-Ir alloy with an α-Al_2O_3 inlay. An empty crucible (inlay included) was utilized as reference. Powdered coating material was used in order to avoid substrate interference during the DSC - TGA measurements. Therefore, the coatings were chemically removed from the iron foil substrate by dissolving it in 35 % hydrochloride acid at 70 °C for approximately 30 min.

The remaining film material was rinsed with acetone and manually ground to powder.

Coated polycrystalline Al_2O_3 substrates were annealed in a Centorr LF22-200 vacuum oven at annealing temperatures T_a ranging from 800 to 1500 °C in steps of 100 °C using a heating rate of 20 K/min, a holding time of 1h. Cooling was performed passively, by switching off the heater, which results in cooling rates of at least 50 K/min down to 200 °C.

Information on the crystallographic composition was obtained by X-Ray Diffraction (XRD) in a Bragg-Brentano arrangement (BB: 2θ=15–90°), for as deposited and annealed powder samples as well as in grazing-incidence arrangement (GI: angle of incidence Ω=2°, 2θ=15–90°), for as deposited and annealed coatings on Al_2O_3 substrates using an Empyrean PANalytical θ-θ diffractometer with a Cu K_α radiation source and a scintillation-detector.

7.3 Results and discussion

7.3.1 Growth morphology, chemistry, and microstructure

The growth morphology of our gradient-coating, Fig. 7.1a shows a SEM cross section overview image, which contains dark and bright contrasted regions representing (Al,Cr)N and (Al,Cr)$_2$O$_3$, respectivley. Their intermediate transition zones thus correspond to (Al$_x$Cr$_{1-x}$)(O$_{1-y}$N$_y$) oxynitrides with different n-to-O ratios, y. The substrate near region of our coating (N-rich) is more compact (with a lower amount of droplets) than the columnar structured zone in the middle of the cross section (which is O-rich). This is confirmed by corresponding transmission electron microscopy cross-section studies, Fig. 7.1b. Selected area electron diffraction patterns of the transition zone from (Al,Cr)N to (Al,Cr)$_2$O$_3$ were obtained using a 160 nm aperture, placed at six positions (marked by numbered white circles) in the substrate near region directly next to each other, Fig. 7.1c. These diffraction patterns (presented inf Fig. 7.1d, e, f, g, h, and I with corresponding TEM cross sections) indicate a single-phase face-centred cubic structure for thes regions, with a change from random-like towards pronounced (200) and (220) orientation with increasing distance from the substrate.
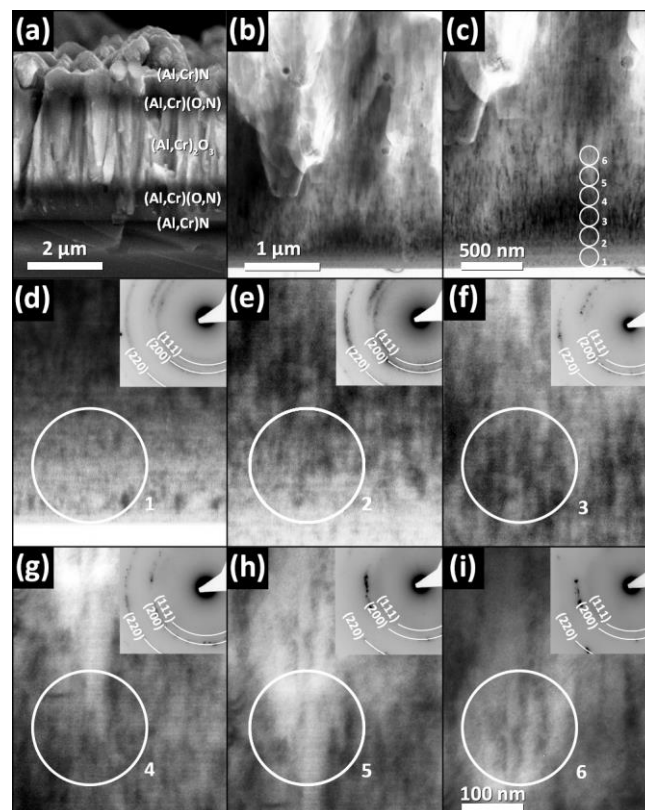
Fig. 7.1: Cross-sectional overview images of our (Al,Cr)N–(Al,Cr)$_2$O$_3$–(Al,Cr)N gradient coating by (a) SEM and (b,c) TEM. TEM details of the regions indicated in (c) are given in (d, e, f, g, h, and i) with corresponding SAED insets.

STEM-EDS measurements, Fig. 7.2, demonstrate that the nitride-to-oxide transition zone of our ~4.4 µm thick gradient-coating is already completed after 1 µm distance from the substrate. Within this 1 µm, the nitrogen content decreases from ~30 to ~4 at.%, while the oxygen content increases from ~10 to ~56 at.%. The Al and Cr content decrease from ~42 to ~28 at.% and ~20 to 13 at.%, respectively. After the first 1-µm, the chemical composition is nearly unchanged up to ~3.5 µm. This clearly highlights the much higher attraction of oxygen to the metals than nitrogen. Please remember that until the middle of the coating (~2.2 µm) the N_2 flow rate (within the deposition chamber) continuously decreased from 1000 to 0 sccm while the O_2 flow rate increased from 0 to 1000 sccm (and vice versa from ~2.2 µm to the final thickness of the coating of ~4.4 µm).
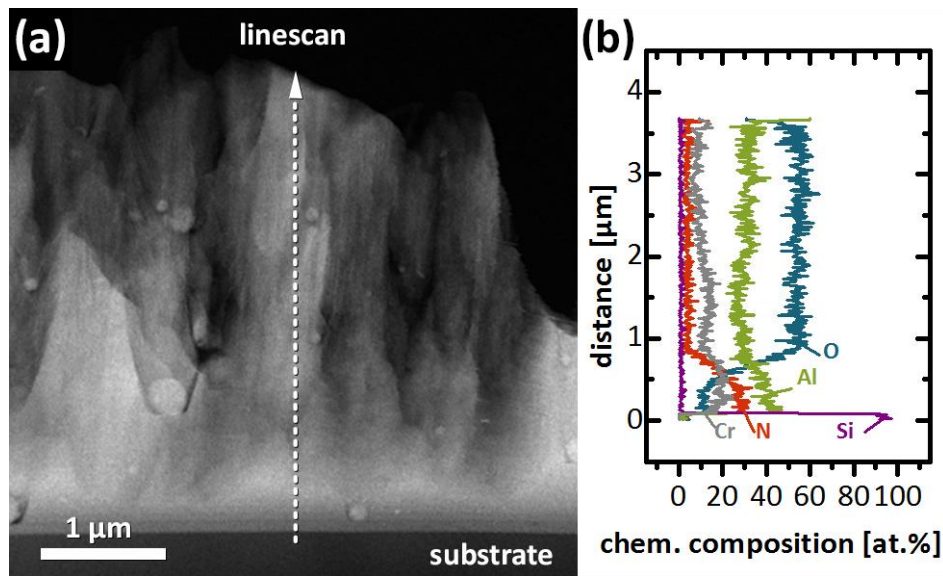
Fig. 7.2: (a) Cross-sectional STEM image with (b) EDS-linescan of our (Al,Cr)N–(Al,Cr)$_2$O$_3$–(Al,Cr)N gradient coating (the total coating thickness was ~4.4 µm).

The The SEM-EDS obtained chemical composition of our $(Al_xCr_{1-x})(O_{1-y}N_y)$ oxynitride coatings, prepared with different N_2/O_2 gas flow rations, is presented in Table 1. Although, sample A was prepared with a very high N_2/O_2 gas flow ratio of 90/10 (%-ratio), their oxygen content is already ~16.0 at.%. This again (in addition to the EDS-linescan of our nitride-oxide-nitride gradient coating, Fig. 7.2) significantly highlights the much higher reactivity of O_2 than N_2 with the metallic species (Al and Cr). With further increasing the O_2 content of the reactive atmosphere, hence decreasing the N_2/O_2 ratio to 70/30 (sample E), the oxygen content within our oxynitride increases to 54.5 at% and the nitrogen content decreases to 5.0 at%. Simultaneously, the cation-to-anion ratio [represented by (Al+Cr)/(O+N) in Table 1] decreases from 0.9 to 0.68. But, although the O-content and N-content of our $(Al_xCr_{1-x})(O_{1-y}N_y)$ oxynitrides continuously increases and decreases, respectively, with decreasing N_2/O_2 ratio, their Al/(Al+Cr) ratio, x, is nearly

93

unchanged at ~0.6, see Table 1 and Fig. 7.3b. Only the oxynitride prepared with the lowest N_2/O_2 ratio (70/30) has a slightly higher Al/(Al+Cr) ratio of x ~0.63. This is also the coating, which shows already a significant formation of fcc-$(Al,Cr)_2O_3$ like phases and α-$(Al,Cr)_2O_3$, see Fig. 7.3a.

Table 7.1: Elemental composition of monolithically grown $(Al_xCr_{1-x})(O_{1-y}N_y)$ obtained by SEM-EDS.

sample	N_2/O_2 in gas flow	chemical composition [at.%]				$\dfrac{Al}{(Al+Cr)}$	$\dfrac{Cr}{(Al+Cr)}$	$\dfrac{O}{(O+N)}$	$\dfrac{N}{(O+N)}$	$\dfrac{(Al+Cr)}{(O+N)}$
	[%]	Al	Cr	O	N	[%]	[%]	[%]	[%]	
A	90/10	27.9	19.3	16.0	36.7	59.1	40.9	30.3	70.7	0.90
B	85/15	26.8	17.6	25.5	30.0	60.3	39.7	45.9	54.1	0.80
C	80/20	25.6	17.5	35.0	21.9	59.4	40.6	61.6	38.4	0.76
D	75/25	24.2	16.2	48.3	11.3	60.0	40.0	81.0	19.0	0.68
E	70/30	25.7	14.8	54.5	5.0	63.4	36.6	91.6	8.4	0.68

For comparison, also the XRD patterns of monolithically grown $(Al,Cr)N$ and $(Al,Cr)_2O_3$ coatings—prepared with comparable settings—are added at the bottom to Fig. 7.3a. The XRD patterns, Fig. 7.3a clearly show that up to N_2/O_2 ratios of 80/20 our $(Al_xCr_{1-x})(O_{1-y}N_y)$ oxynitrides basically crystallize in the fcc-$(Al,Cr)N$ like structure, please see the (111), (200), and (220) peaks at 2θ ~38, 45, and 65 °, respectively (indicated by red solid squares in Fig. 7.3a). For N_2/O_2 ratios of 75/25 and 70/30, especially the (111) XRD peaks are almost not detectable anymore. The decreasing intensity of the (111) XRD peak intensity with increasing O-content of our oxynitrides, can be related to changed surface energies. Castaldi et al. [119] suggested, that for fcc-structured CrN_yO_{1-y}, the surface energy of (111) planes increases with the oxygen content, because substituting N with O would increases the polarization due to the higher electronegativity. Consequently, (111) planes are less preferable for higher O contents and thus the (111) XRD peaks decrease in intensity.

With increasing O-content, the XRD peak positions at 2θ ~38, 45 and 65 ° continuously shift to higher diffraction angles, from fcc-$(Al,Cr)N$ towards fcc-$(Al,Cr)_2O_3$. Consequently, this indicates decreasing lattice parameters (presented in Fig. 7.4) and a change from fcc-$(Al,Cr)N$ like to fcc-$(Al,Cr)_2O_3$ like phases, which also suggest for the formation of metal vacancies (for the B1-like NaCl-type structure). This is in agreement with the concomitant reduction of the cation-to anion ratio, Table 7.1, and recent results by Stüber et al. [61] and Khatibi et al. [120] reporting the formation of fcc-structured Al–Cr–O–N and Al–Cr–O thin films, respectively. The comparison with the $(Al,Cr)N$ coating, prepared with comparable deposition conditions (same deposition system, $Al_{0.7}Cr_{0.3}$ targets, bias potential, deposition pressure, substrate temperature) in N_2 atmosphere (hence, N_2/O_2 flow ratio of 100/0) clearly highlights that already small additions of oxygen promote the crystallization in fcc structure, Fig. 7.3. Without oxygen, a significant fraction of wurtzite structured w-AlN based phases are present. This behaviour is in agreement with other density functional theory calculations, highlighting that the fcc

structure (contrary to hexagonal structured counterparts) is relatively insensitive for vacancies. These are preferred, when oxygen substitutes for nitrogen to keep the charge balance (N^{3-} vs. O^{2-}), which is also indicated by the above-mentioned decrease in cation-to anion ratio in parallel.

When evaluating the lattice parameters from the SAED patterns taken during the cross sectional studies of our $(Al,Cr)N$–$(Al,Cr)_2O_3$–$(Al,Cr)N$ gradient-coating, and correlating these regions with the N_2/O_2 flow rate present during deposition, we obtain an excellent correlation with the lattice parameters of our $(Al_xCr_{1-x})(O_{1-y}N_y)$ oxynitrides, see Fig. 7.4.
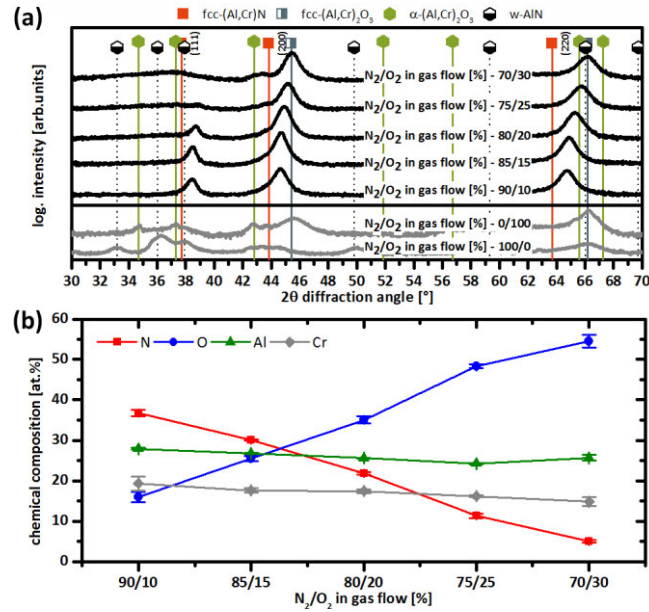
Fig. 7.3: (a) XRD patterns and (b) chemical composition of powdered $(Al_xCr_{1-x})(O_{1-y}N_y)$ oxynitride coatings. The XRD patterns are labelled with the N_2/O_2 gas flow ratio (in %) used during their deposition.
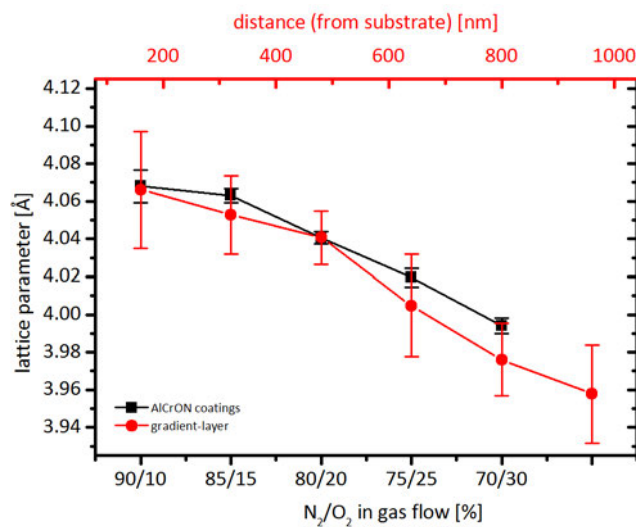
Fig. 7.4: Lattice parameter of the fcc-structured $(Al_xCr_{1-x})(O_{1-y}N_y)$ coatings and of the transition zone in our nitride-oxide-nitride gradient coating obtained from the XRD and SAED patterns, respectively.

7.4 Thermal stability and phase evolution

The base-line subtracted DSC (heat flow) and TGA (mass loss) signals of our five different $(Al_xCr_{1-x})(O_{1-y}N_y)$ oxynitrides during annealing in He atmosphere up to 1500 °C, show reduced endothermic contributions and significantly reduced mass-loss, especially for the coatings prepared with N_2/O_2 ratios of 75/25 and 70/30 (hence, O-rich), see Fig. 5. Based on our previous studies on the thermal stability of (Al,Cr)N [30,31,52] and $(Al,Cr)_2O_3$ (chapter 6.3.1.1), we can conclude that the exothermic DSC features up to ~1000 °C, basically stem from recovery processes of deposition-induced structural defects. The superimposed endothermic features, for example for the highest N-containing oxynitride (prepared with $N_2/O_2 = 90/10$), with peak temperatures of ~1150 and 1180 °C are due to dissociation of Cr–N bonds to form hexagonal close packed (hcp) Cr_2N and body centred cubic (bcc) Cr, respectively, via N_2-release [30,106]. The connected two-step N_2-release (from CrN to Cr_2N to Cr) can nicely be seen by the mass-loss curve having two different slopes, Fig. 7.5, due to the different bonding states of nitrogen in fcc-CrN and hcp-Cr_2N. The rather strong exothermic DSC features between 1300 and 1400 °C are due to grain growth, recrystallization, and/or sintering processes. (The comparison between DSC and TGA clearly shows that the TGA signal is more suitable to rate the thermal stability of our $(Al_xCr_{1-x})(O_{1-y}N_y)$ oxynitrides with respect to their dissociation of Cr–N bonds and the connected N_2-release).

The comparison of the TGA curves of our five different $(Al_xCr_{1-x})(O_{1-y}N_y)$ oxynitrides suggest, that the coatings prepared with N_2/O_2 ratios of 90/10, 85/15, and 80/20, end up with virtually the same mass-loss after annealing up to 1500 °C, Fig. 7.5. This is somehow surprising as their N-content is different. The coating prepared with N_2/O_2 ratios of 75/25 and 70/30 exhibit significantly lower mass-loss of ~4.7 and < 1 %, respectively, according to their lower N-content. These coatings also show the highest onset temperature of ~1150 °C for the mass-loss.
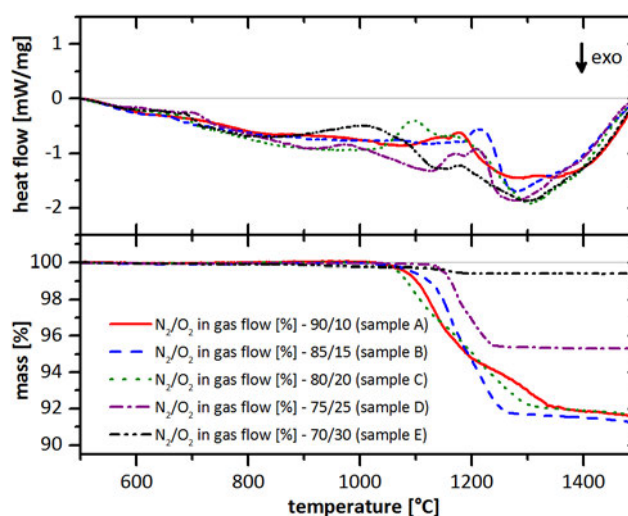
Fig. 7.5: DSC and TGA signals of powdered $(Al_xCr_{1-x})(O_{1-y}N_y)$ oxynitride coatings during annealing in He atmosphere up to 1500 °C.

The structural investigations by XRD of these five different $(Al_xCr_{1-x})(O_{1-y}N_y)$ oxynitrides prepared with N2/O2 ratios of 90/10, 85/15, 75/25, and 70/30, Fig. 7.6a, b, c, and e, respectively, show their phase transformations annealing at selected temperatures. The three N-rich oxynitrides show a comparable transformation of their fcc structure with increasing T_a. With increasing oxygen content, the formation of w-AlN like phases is postponed to higher temperatures, see Fig. 7.6a, b, and c. In the intermediate temperature ranges (1100–1300 °C) the formation of hcp-Cr_2N phases can be detected, which upon further annealing transform to bcc-Cr, in agreement with their significant mass-loss curves. After annealing at 1500 °C, these coatings exhibit a significant fraction of metallic bcc-Cr, w-AlN, and α-$(Al,Cr)_2O_3$. The formation of the latter can be detected after annealing at T_a = 1500 °C, their α-$(Al,Cr)_2O_3$ phases are rather Al-rich, as indicated by their XRD peak position being close to α-Al_2O_3.

 Contrary to these observations, the two O-rich coatings prepared with N2/O2 ratios of 75/25 and 70/30, Fig. 7.6d and e, respectively, exhibit significant smaller fractions of metallic bcc-Cr after annealing at T_a = 1500 °C (indicated by their rather low XRD peak intensities). For the oxynitride with highest oxygen content (prepared with N2/O2 = 70/30), almost no bcc-Cr but still some hcp-Cr_2N can be detected for T_a = 1500 °C, see the small XRD peak at $2\theta \sim 40$ ° in Fig. 7.6e. Furthermore, these two oxynitrides exhibit a significant formation of crystalline α-$(Al,Cr)_2O_3$ phases for $T_a \geq 1120$ °C. This temperature corresponds to the exothermic feature during their DSC investigations (compare Fig. 7.5). Due to their lower fraction of metallic bcc-Cr present, the XRD peak positions for these α-$(Al,Cr)_2O_3$ phases, are rather close to the calculated position for a α-$(Al_{0.7},Cr_{0.3})_2O_3$ solid solution. Hence, there is a higher Cr content soluted in the α-$(Al,Cr)_2O_3$ phases than for the other three oxynitride coatings (Fig. 7.6a, b, and c).

These structural changes are qualitatively presented in Fig. 7.7a and b for our $(Al_xCr_{1-x})(O_{1-y}N_y)$ oxynitrides with lowest and highest oxygen content (i.e., prepared with N2/O2 ratios of 90/10 and 70/30), respectively.
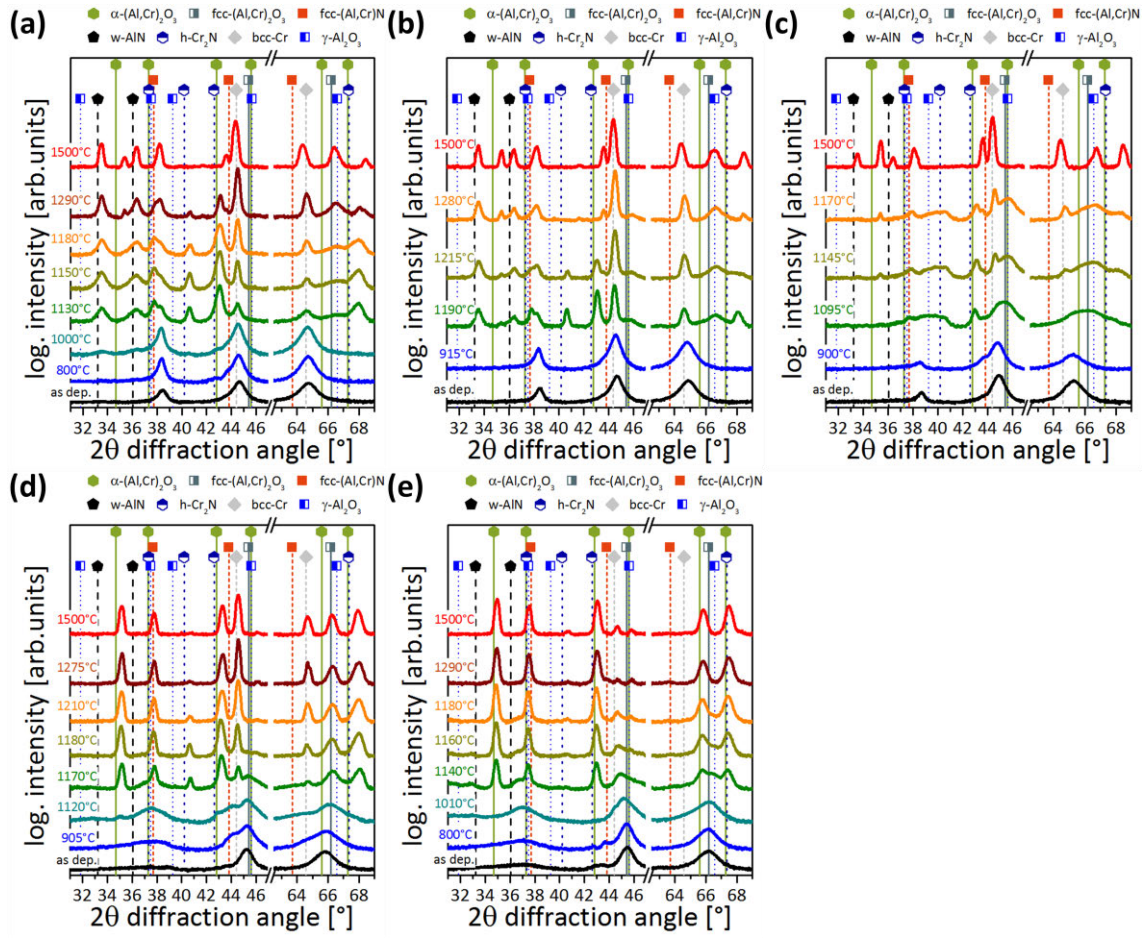
Fig. 7.6: XRD patterns of our $(Al_xCr_{1-x})(O_{1-y}N_y)$ oxynitrides prepared with N_2/O_2 ratios of (a) 90/10, (b) 85/15, (c) 82/20, (d) 75/25, and (e) 70/30. The individual patterns are labelled with the annealing temperatures T_a.
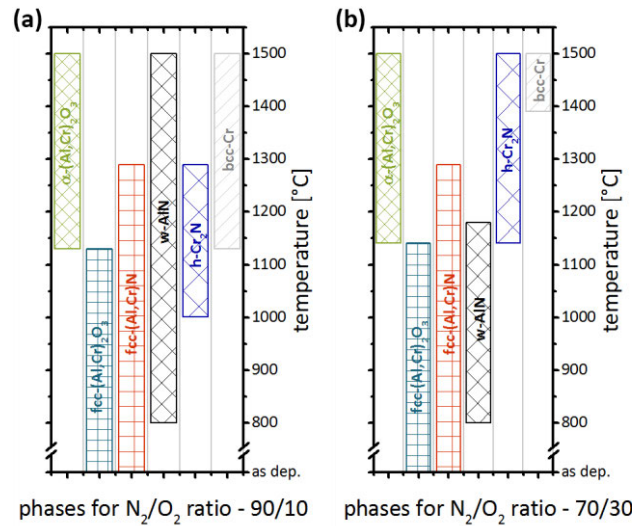
Fig. 7.7: The bar charts highlights the phases with the annealing temperatures T_a of our $(Al_xCr_{1-x})(O_{1-y}N_y)$ oxynitrides prepared with N_2/O_2 ratios of (a) 90/10 and (b) 70/30.

7.4.1 Thermo-Mechanical properties

To further proof the high thermal stability of the O-rich $(Al_xCr_{1-x})(O_{1-y}N_y)$ oxynitrides, we have vacuum-annealed coated polycrystalline Al_2O_3 substrates at Ta ≤ 1500 °C (for 1 h), and subsequently measured their hardness and structural evolution. The XRD measurements are in line with the presented XRD patterns in Fig. 7.8.
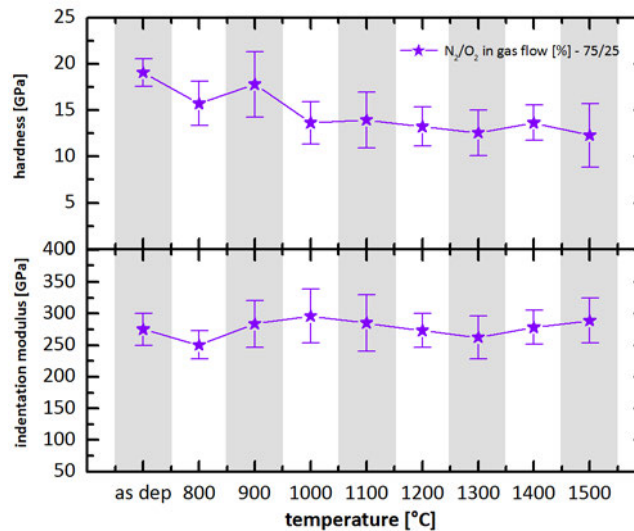
Fig. 7.8: Hardness and indentation modulus of our $(Al_xCr_{1-x})(O_{1-y}N_y)$ oxynitrides prepared with N_2/O_2 ratios of 75/25.

The hardness of the O-rich $(Al_xCr_{1-x})(O_{1-y}N_y)$ oxynitride coating prepared with N_2/O_2 ratios of 75/25 decreases with increasing annealing temperature from ~19 GPa (as deposited value) to ~13 GPa (T_a ≥ 1000 °C), while the indentation modulus of ~275 GPa stays relatively constant up to even 1500 °C, see Fig. 7.8. The hardness drop after annealing T_a = 1000 °C, can be assigned to the decomposition of Cr–N bonds and thus the dissociation of CrN to Cr_2N and further to Cr via N_2-release.The transformation of fcc-$(Al,Cr)_2O_3$ towards α-$(Al,Cr)_2O_3$ at this temperature might effectively help to keep the hardness relatively constant up to 1500 °C.

7.5   Summary and conclusions

Various $(Al_xCr_{1-x})(O_{1-y}N_y)$ coatings – arc evaporated using $Al_{0.7}Cr_{0.3}$ targets and different nitrogen-to-oxygen ratios, y – studied in detail for their phase evolution and thermal stability. The development of $(Al_xCr_{1-x})(O_{1-y}N_y)$ coatings with characteristic nitrogen-to-oxygen ratios stems on elaborated cross sectional TEM and SAED studies of $(Al,Cr)N$–$(Al,Cr)_2O_3$–$(Al,Cr)N$ gradient coatings (using the same $Al_{0.7}Cr_{0.3}$ targets). Based on dynamical differential scanning calorimetry and thermogravimetric analysis up to 1500 °C, in combination with subsequent X-ray powder diffraction, we can conclude, that the thermal stability of $(Al_xCr_{1-x})(O_{1-y}N_y)$ oxynitrides increase with increasing O content, up to ~81 at.% of the non-metallic sublattice. Especially, the high O-containing coatings are prone for the formation of volatile Cr-oxides. However, the typically observed two-step dissociation process of Cr–N bonds towards Cr (via the formation of Cr_2N and N_2-release), retards to a one-step process (up to 1500 °C) for N-contents below 10 at.% of the non-metallic sublattice.

Consequently, by knowledge-driven finetuning of the nitrogen-to-oxygen ratio, the thermal stability of $(Al_xCr_{1-x})(O_{1-y}N_y)$ oxynitrides can be designed for their application-based specific needs.

8. Dependence of chemistry, morphology, and properties of Al-Cr-O-N coatings on the synthetic air flow during arc evaporation

8.1   Introduction

Oxynitride coatings in general have recently gained an intense interest due to their outstanding physical and chemical properties, making them promising alternatives for already well established coating systems for specific application, but also provide the possibility to enter new application fields [107–118]. Here, especially Al-Cr-based oxynitrides have attracted considerable attention [61,65–68].

When preparing oxynitrides, and solid solutions are formed, vacancies and interstitials (interstitials are less preferable than vacancies, especially in Al-Cr-O [121]) are required to keep an overall charge balance. For example, the decreasing lattice parameter a, of the cubic structure in $(Al_xCr_{1-x})(O_{1-y}N_y)$ solid solutions, is basically due to the formation of vacancies at the metallic sublattice [67]. Already with small additions of N to the metal sublattice, the crystallisation in a face centred cubic (fcc) structure is preferred, thus single-phase fcc-structured solid solutions are possible for oxygen contents already below 97 at.% (of the non-metallic sublattice). For oxygen contents below 60 at.% (of the non-metallic sublattice) hardness even above 31 GPa can be obtained, due to the resulting changes in the bonding states [70]. Even for relatively low O_2 partial pressures of the reactive gas atmosphere (composed of O_2 and N_2), high O-containing $(Al_xCr_{1-x})(O_{1-y}N_y)$ oxynitrides can be synthesized by arc evaporation of Al-Cr cathodes, due to the very high O-affinity of Al and Cr [71] (see chapter 7).

Although considerable research activities are carried out on Al-Cr-O-N hard coatings, only little is known about arc evaporated oxynitrides prepared with synthetic air, and especially the effect of the synthetic air flow on chemistry, morphology and properties of $(Al_xCr_{1-x})(O_{1-y}N_y)$ oxynitrides and their multilayers has not been studied so far. Therefore, we developed $(Al_xCr_{1-x})(O_{1-y}N_y)$ oxynitrides with different N-ratios, y (of the non-metal sublattice), as well as their multilayers, by simply varying the synthetic air

flow during arc evaporation of $Al_{0.7}Cr_{0.3}$ cathodes (without adding any other gases).

8.2 Experimental

All coatings investigated were synthesised in an Oerlikon Balzers Innova batch-type cathodic arc evaporation system equipped with powder metallurgically (PM) prepared $Al_{0.7}Cr_{0.3}$ cathodes (Plansee Composite Materials GmbH). The low alloyed iron steel foil and Si (100) substrates were ultrasonically cleaned in acetone and ethanol for 10 min and then mounted on a two-fold rotation carousel with a minimum cathode-to-substrate distance of approximately 25 cm. The deposition chamber was heated to 500 °C by a combined radiation and plasma heating process for approximately 30 min. Ar ion etching, using the Balzers Central Beam Etching Technology, was performed for another 30 min, in order to remove any residuals and oxides from the substrate surfaces, and in further consequence to enhance adhesion.

Four different $(Al_xCr_{1-x})(O_{1-y}N_y)$ oxynitrides, were deposited by using only synthetic air (80% N_2 and 20% O_2) as the gas carrier with absolute flow rates of 200, 500, 800, and 1100 sccm (or 50, 125, 200, and 275 sccm per cathode, resulting in total pressures of ~0.2, 1.2, 2.0, and 3.3 Pa) during arc evaporation of four $Al_{0.7}Cr_{0.3}$ cathodes with 150 A arc current for 120 min. A negative substrate bias of -40 V (DC) was applied for these coatings.

The $(Al_xCr_{1-x})(O_{1-y}N_y)$ multilayers – combining N-rich and O-rich oxynitrides layers (150 and 112 bilayers) – are prepared by alternatingly operating a neighbouring pair of $Al_{0.7}Cr_{0.3}$ cathodes that are individually fed with 500 (250 per active source, p.a.s) or 1000 (500 p.a.s.) sccm synthetic air flow (the arc current was 150 A). The average gas pressure during preparing the individual layers was thus ~0.5 and ~1.2 Pa, respectively. Operating each cathode pair for 30 s before switching to the other leads to a bilayer period of ~20 nm. Two variants this $(Al_xCr_{1-x})(O_{1-y}N_y)$ multilayer-type are realized by preparing a smooth or steep transition between the individual N-rich and O-rich layers (according to the smooth or steep change from 125 to 200 sccm p.a.s. synthetic air flow). The smooth transition, which lead to blurred interfaces is described in more detail in chapter 5, while the steep transition, which lead to distinct interfaces is adapted from [122].

In order to enhance growth kinetics, a negative bipolar pulsed substrate bias of -40 V was applied for the multilayer coatings.

Chemical and morphological investigations of our coatings were carried out using a FEI Quanta 200 Field Emission Gun Scanning Electron Microscope (FEG SEM) with an Energy Dispersive X-Ray Spectroscopy (EDS) detector attached.

The thermal stability of our coatings was investigated by a combination of differential scanning calorimetry (DSC) and thermal gravimetric analysis (TGA) using a DSC-STA 449 F1 Jupiter®, calibrated with 7 elements (In, Sn, Bi, Zn, Al, Ag, Au). The dynamic measurements were carried out with a heating rate of 20 K/min up to 1500 °C in a dynamical He as well as synthetic air atmosphere (protective=50 ml/min; purge=50 ml/min), respectively. In order to remove contaminations, an isothermal annealing step

(within the DSC-STA) was conducted for 20 min at 150 °C. The crucibles for the powder samples are made of Pt-Ir alloy with an α-Al_2O_3 inlay, and an empty crucible (inlay included) was used as reference. To avoid substrate interference during the DSC - TGA measurements, the coatings were removed from their iron foil substrates by dissolving the substrates in 30 % hydrochloride acid at 70 °C for approximately 30 min. The remaining film material was rinsed with acetone and manually ground to powder.

Information on the microstructure and crystallography was obtained by X-Ray diffraction (XRD) in Bragg-Brentano arrangement (BB: 2θ=15–90°), for as deposited and annealed powder samples as well as in grazing-incidence arrangement (GI: angle of incidence Ω=2°, 2θ=15–90°), for as deposited coatings on Si substrates using an Empyrean PANalytical θ-θ diffractometer with a Cu K_α radiation source and a scintillation-detector.

The hardness (H) and indentation modulus (E) of our coatings grown on Si substrates in their as-deposited state were obtained by nanoindentation, using an Ultra-Micro-Indentation II system equipped with a Berkovich diamond tip. Normal loads ranging from 20 to 10 mN were applied and the indentation curves were evaluated according to Oliver and Pharr [88].

8.3 Results and discussion

8.3.1 Chemical composition, growth morphology, and structure

The chemical compositions of our $(Al_xCr_{1-x})(O_{1-y}N_y)$ oxynitride coatings and their multilayers, determined by SEM-EDS, exhibit lower Al and higher Cr contents than the nominal cathode $Al_{0.7}Cr_{0.3}$ composition. This is in agreement with previous reports on arc evaporated $(Al_xCr_{1-x})(O_{1-y}N_y)$ coatings, using PM Al_xCr_{1-x} cathodes [71]. The $(Al_xCr_{1-x})(O_{1-y}N_y)$ oxynitride coatings exhibit a significantly increased oxygen content – accompanied by a reduced nitrogen content – with increasing synthetic air flow rate (although no other gas sources were used or added). This suggest that the absolute oxygen pressure during deposition significantly determines the oxygen content of our $(Al_xCr_{1-x})(O_{1-y}N_y)$ oxynitride coatings, whereas the high N_2 ratio in synthetic air (80% N_2 and 20% O_2) helps to prepare N-rich $(Al_xCr_{1-x})(O_{1-y}N_y)$ oxynitrides even for lower total pressures. These results agree with studies on the O_2-flow dependent oxide formation during arc evaporation of Al-Cr cathodes (done by my college Valentin Dahlbauer, who hasn´t published this results yet). Thus, the nitrogen fraction (i.e., the N/(O+N) ratio, y) decreases from 0.8 (ON-50) to even 0.0 (ON-200 and ON-275) when increasing the synthetic air flow rate from 50 to ≥ 200 sccm (p.a.s.). Here we need to mention that ON-200 shows a small fraction of a nitride phase after annealing in He atmosphere up to 1500 °C, this is not the case for ON-275. Hence, ON-200 contains N, but below the detection limit of our EDS facility used, whereas ON-275 is an oxide coating.

Table 8.1: Elemental composition of our $(Al_xCr_{1-x})(O_{1-y}N_y)$ oxynitrides (ON) and their multilayers (ML) obtained by SEM-EDS. The Al/(Al+Cr) ratio corresponds to x and the N/(O+N) ratio corresponds to y. The nomenclature of the ON samples indicates the used synthetic air flow (in sccm p.a.s.), and that of the ML samples indicates the interfaces type (smooth or steep) between the N-rich and O-rich layers.

sample	synth. air p.a.s. [sccm]	chemical composition [at.%]				$\dfrac{Al}{(Al+Cr)}$ [%]	$\dfrac{Cr}{(Al+Cr)}$ [%]	$\dfrac{O}{(O+N)}$ [%]	$\dfrac{N}{(O+N)}$ [%]	$\dfrac{(Al+Cr)}{(O+N)}$
		Al	Cr	O	N					
ON-50	50	24.3	13.6	12.5	49.5	64.1	35.9	20.2	79.8	0.61
ON-125	125	23.3	12.2	55.0	9.5	65.6	34.4	85.3	14.7	0.55
ON-200	200	26.8	13.8	59.4	0.0	66.0	34.0	100.0	0.0	0.68
ON-275	275	25.3	15.9	58.8	0.0	61.4	38.6	100.0	0.0	0.70
ML-smooth[1]	125/250	24.2	11.9	55.0	8.8	67.0	33.0	86.2	13.8	0.57
ML-steep[2]	125/250	24.0	12.1	49.2	14.7	66.5	33.5	77.0	23.0	0.56

[1]ML-smooth:
Multilayer with a smooth transition between the $(Al_{0.66}Cr_{0.34})(O_{0.85}N_{0.15})$ and $(Al_{0.62}Cr_{0.38})_2O_3$ layers
[2]ML-steep:
Multilayer with a steep transition between the $(Al_{0.66}Cr_{0.34})(O_{0.85}N_{0.15})$ and $(Al_{0.62}Cr_{0.38})_2O_3$ layers

The metal-to-nonmetal ratio of $(Al_{0.66}Cr_{0.34})(O_{1.0}N_{0.0})$ (ON-200) and $(Al_{0.62}Cr_{0.38})_2O_3$ (ON-275) is rather close to 2/3, indicating the formation of $(Al,Cr)_2O_3$ based compositions, see Table 8.1, as the stable oxides of Al and Cr would suggest. Contrary, the N-rich oxynitrides $(Al_{0.64}Cr_{0.36})(O_{0.2}N_{0.8})$ (ON-50) and $(Al_{0.66}Cr_{0.34})(O_{0.85}N_{0.15})$ (ON-125) as well as the multilayers (ML-smooth and ML-steep) have metal-to-nonmetal ratios between only 0.55 and 0.61, which would suggest vacancies at the metal sublattice, as the formation of interstitials at the non-metal sublattice is rather expensive [67,121]. As the accuracy of EDS, especially for light elements such as N and O, is limited, we don´t want to over-interpret the metal-to-nonmetal ratio. However, the trend of a decreasing ratio from 0.61 to 0.55 (hence, increasing metal vacancies) with increasing O-content fits to the charge balance (if O^{2-} substitutes N^{3-}, fewer cations are needed for a balance).

The growth morphology of our $(Al_xCr_{1-x})(O_{1-y}N_y)$ oxynitrides changes from a dense $(Al_x,Cr_{1-x})N$-like towards $(Al_x,Cr_{1-x})_2O_3$-like with increasing flow rate from 50 to 125 to 200 to 275 sccm (p.a.s.), see Fig. 8.1a, b, c, and d, respectively. Especially the boundary cases, samples ON-50 (Fig. 8.1a) and ON-275 (Fig. 8.1d) almost perfectly represent their corresponding nitrides and oxides, respectively. The overview furthermore shows, the enormous increase in coating thickness due to the increased synthetic air flow, and the increased surface roughness (basically due to higher droplet fractions), which is typically when changing from nitrides to oxides. This behaviour is also due to the intense arc generation on the cathode surface in O_2 atmosphere, whereas in N_2 atmosphere finer but widely ramified arcs are generated.

The growth morphology of our $(Al_xCr_{1-x})(O_{1-y}N_y)$ multilayers (composed of layers that have been prepared with 125 and 250 sccm p.a.s.), is almost perfectly between those of the oxynitrides prepared with 50 and 125 sccm (p.a.s.), please compare Fig. 8.1e and f with Fig. 8.1a and b. The individual layers of our multilayers ML-smooth and ML-steep cannot be resolved within the SEM investigations, due to their small bilayer period of ~20 nm, which is calculated by dividing their total coating thickness 3.06 and 2.24 μm with their 150 and 112 bilayers, respectively. Due to the smaller total number of bilayers for ML-steep, the coating is thinner, which was a result of an unintended shut-down of the deposition process.
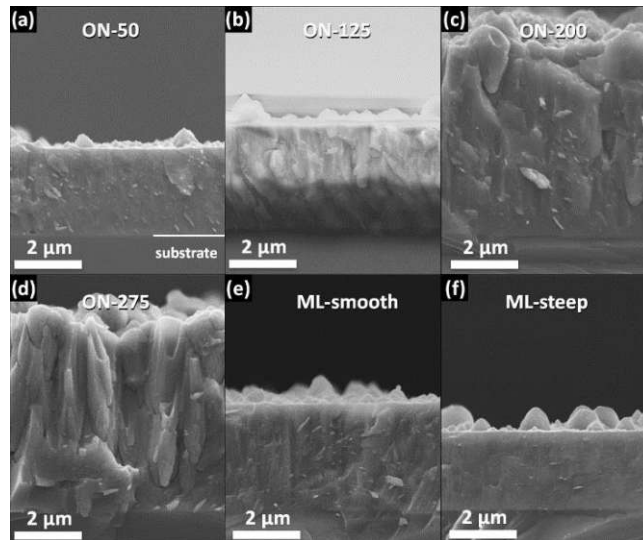
Fig. 8.1: Cross-sectional SEM images of $(Al_xCr_{1-x})(O_{1-y}N_y)$ oxynitrides prepared with (a) 50, (b) 125, (c) 200, and (d) 275 sccm (p.a.s.) synthetic air flow. The SEM cross sections of the $(Al_xCr_{1-x})(O_{1-y}N_y)$ multilayers are given in (e) and (f) with a smooth and steep transition between their layers prepared with 125 and 250 sccm (p.a.s.), respectively.

With increasing oxygen content of our $(Al_xCr_{1-x})(O_{1-y}N_y)$ oxynitrides, their structure changes from a single phase face-centred cubic nitride-like towards a mixed cubic and hexagonal oxide-like structure, see Fig. 8.2. The $(Al_xCr_{1-x})(O_{1-y}N_y)$ multilayers exhibit XRD patterns according to their layered constituents (prepared with 125 or 250 sccm synthetic air flow). Here, especially for the multilayer with a steep transition between their layers, these lead to slightly separated XRD peaks.
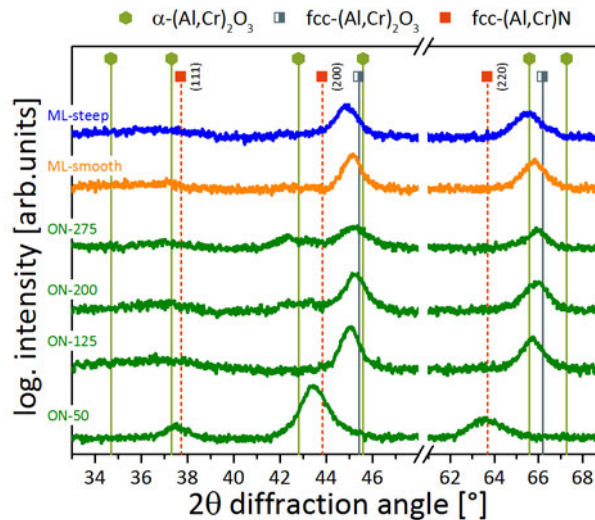
Fig. 8.2: Grazing-incidence X-ray diffraction patterns of $(Al_xCr_{1-x})(O_{1-y}N_y)$ oxynitrides prepared with 50, 125, 200, and 275 sccm (p.a.s.) and $(Al_xCr_{1-x})(O_{1-y}N_y)$ multilayers with a smooth and steep transition between their layers prepared with 125 and 250 sccm (p.a.s.), respectively.

106

The With increasing O-content (i.e., increasing synthetic air flow) the hardness of our $(Al_xCr_{1-x})(O_{1-y}N_y)$ oxynitrides decreases from 33.2±1.4 to 14.6±1.5 GPa, Fig. 8.3. This is in agreement with the transition from a dense (Al,Cr)N-like coating (ON-50), to a $(Al,Cr)_2O_3$-like coating (ON-275). Correspondingly, also the indentation modulus decreases from 303±12 GPa to 210±10 GPa with increasing oxygen content. For a good comparison, we also prepared $(Al_{0.7}Cr_{0.3})N$ (with four operating $Al_{0.7}Cr_{0.3}$ sources and 275 sccm N_2 p.a.s.) and $(Al_{0.7}Cr_{0.3})_2O_3$ (with four operating $Al_{0.7}Cr_{0.3}$ sources and 250 sccm O_2 p.a.s.) coatings. Their hardness and indentation modulus is added to Fig. 8.3.

Because the growth morphology of our $(Al_xCr_{1-x})(O_{1-y}N_y)$ multilayers (with a smooth and steep transition between their layers prepared with 125 and 250 sccm p.a.s) is closer to that of the N-rich oxynitrides also their hardness is relatively high with ~26±3 GPa (see the half-filled orange and blue triangles in Fig. 8.3.
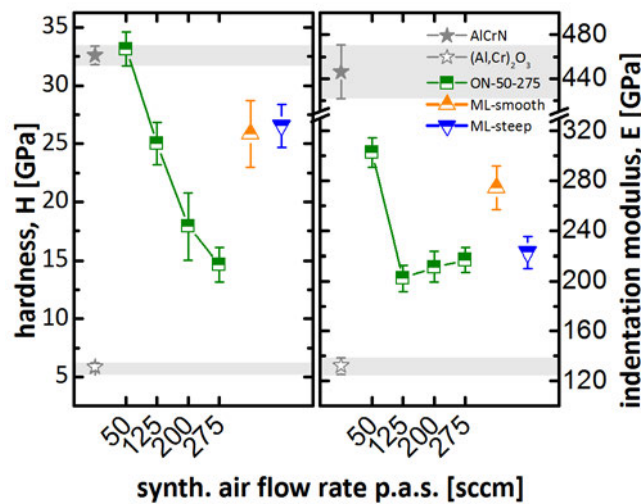
Fig. 8.3: Hardness and indentation modulus of $(Al_xCr_{1-x})(O_{1-y}N_y)$ oxynitrides prepared with 50, 125, 200, and 275 sccm (p.a.s.) and $(Al_xCr_{1-x})(O_{1-y}N_y)$ multilayers with a smooth and steep transition between their layers prepared with 125 and 250 sccm (p.a.s.), respectively. For comparison, H and E of the corresponding nitride $(Al_{0.7}Cr_{0.3})N$ and oxide $(Al_{0.7}Cr_{0.3})_2O_3$ coatings are added. These values are taken from [48,123].

8.3.2 Thermal stability and phase evolution

The DSC and TGA curves of our coatings exhibit distinct features, which can be described with the help of the $(Al_xCr_{1-x})(O_{1-y}N_y)$ oxynitride prepared with 125 sccm (p.a.s.) synthetic air flow, Fig. 4a. This coating has a chemical composition according to $(Al_{0.66}Cr_{0.34})(O_{0.85}N_{0.15})$, see Table 8.1, and exhibits distinct mass-loss features in their TGA curve as well as exothermic and endothermic features in their DSC curve. Based on these features, several as deposition coating samples were annealed to individual temperatures (indicated in Fig. 8.4a) and investigated by XRD afterwards, Fig. 8.4b. These patterns clearly show that starting from a fcc dominated structure small fractions of w-AlN phases develop upon annealing to 1235 °C. The dominating XRD peaks of the fcc phase exhibit a small reduction in their width, indicative for structural recovery effects (where structural built-in defects arrange to lower energy site). Consequently, the exothermic features of the corresponding DSC curve are basically due to precipitation and recovery. Higher temperatures clearly lead to a pronounced formation of α-Al_2O_3 based phases, with XRD peak positions almost perfectly matching with α-$(Al,Cr)_2O_3$, fcc-$Al_{0.7}Cr_{0.3}N$ and hcp-Cr_2N and bcc-Cr. The latter two are responsible for the detected mass-loss (as they generate by the dissociation of CrN bonds under release of N_2) with an onset temperature of ~1313 °C, and the endothermic contributions (at 1100-1300 °C) to the DSC signals. The pronounced DSC feature with a peak at around 1300 °C coincides with the annealing temperature of 1300 °C, after which a significant fraction of α-$(Al,Cr)_2O_3$ can be detected, compare Fig. 8.4b and a.
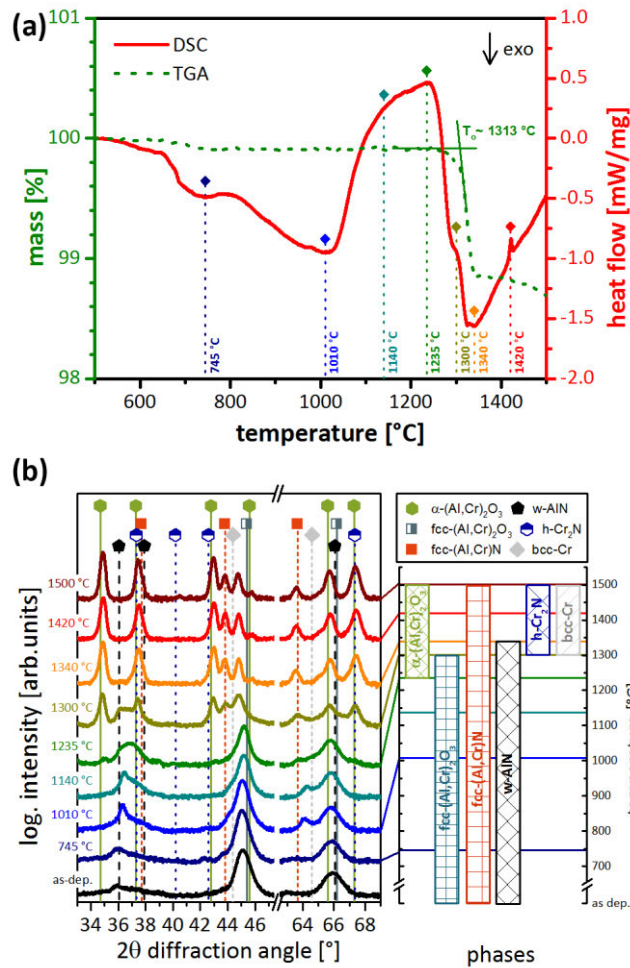
Fig. 8.4: (a) DSC/TGA of $(Al_{0.66}Cr_{0.34})(O_{0.85}N_{0.15})$ powder sample (ON-125), during annealing in He atmosphere. The corresponding XRD patterns after the treatments to selected temperatures (indicated in (a) are given in (b), with the indicated phase evolution. The peak positions for α-$(Al_{0.7}Cr_{0.3})_2O_3$, fcc-$(Al_{0.7}Cr_{0.3})N$, and fcc-$(Al_{0.7}Cr_{0.3})_2O_3$ are indicated [linearly interpolated between the standard peak positions for α-Al_2O_3 (ICDD #00-046-1212) and α-Cr_2O_3 (ICDD #00-038-1479), respectively fcc-AlN (ICDD #00-025-1495) and fcc-CrN (ICDD #01-076-1494)], as well as those for w-AlN (ICDD #00-025-1133), hcp-Cr_2N (ICDD #00-035-0803), and bcc-Cr (ICDD #04-002-9097).

Comparing this $(Al_{0.66}Cr_{0.34})(O_{0.85}N_{0.15})$ oxynitride with the others and the two $(Al_xCr_{1-x})(O_{1-y}N_y)$ multilayers, Fig. 8.5 clearly highlights the impact of their N-content on the onset temperature for the mass-loss (which is always connected with an endothermic contribution to the DSC signal), in agreement with our earlier findings (see chapter 6 and 7). The highest N-containing oxynitride $(Al_{0.64}Cr_{0.36})(O_{0.2}N_{0.8})$ (ON-50), shows a DSC curve as well as a TGA curve rather similar to $Al_xCr_{1-x}N$ nitrides [30,52], with the significant two-step mass-loss indicative for the dissociation of CrN to Cr_2N to Cr (under release of N_2). The distinct change in the slope of the mass-loss at ~1100 °C is based on the changed CrN bonding character. At lower temperatures, N_2 is basically released from CrN, whereas at higher temperatures, N_2 is released from Cr_2N.

The oxynitrides with N-contents below the detection limit, $(Al_{0.66}Cr_{0.34})(O_{1.0}N_{0.0})$ (ON-200) and $(Al_{0.62}Cr_{0.38})_2O_3$ (ON-275), exhibit almost no mass loss (~0.2 wt.%) during

annealing up to 1500 °C. Especially, the $(Al_{0.62}Cr_{0.38})_2O_3$ oxynitride (ON-275, repared with 275 sccm synthetic air p.a.s.) exhibits DSC and TGA curves according to $(Al,Cr)_2O_3$-based coatings [29,54], with their typical features due to the transformation of fcc- and/or γ-Al_2O_3-based phases towards α -Al_2O_3-based phases (see chapter 6 and 7).
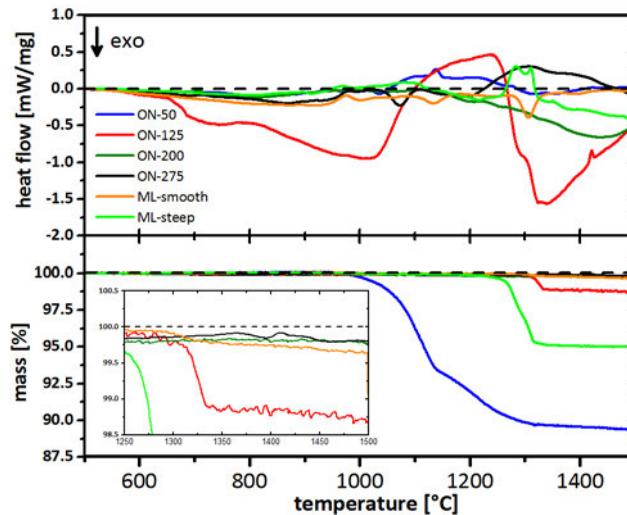
Fig. 8.5: DSC and TGA signals of of $(Al_{0.64}Cr_{0.36})(O_{0.2}N_{0.8})$, $(Al_{0.66}Cr_{0.34})(O_{0.85}N_{0.15})$, $(Al_{0.66}Cr_{0.34})(O_{1.0}N_{0.0})$, and $(Al_{0.62}Cr_{0.38})_2O_3$ coatings, and the multilayers with a steep and smooth transition between their $(Al_{0.66}Cr_{0.34})(O_{0.85}N_{0.15})$ and $(Al_{0.62}Cr_{0.38})_2O_3$ layers (ML-steep and ML-smooth) during dynamical heating in He up to 1500 °C.

The two $(Al_xCr_{1-x})(O_{1-y}N_y)$ multilayers, with either a smooth or a steep transition between their individual layers (basically $(Al_{0.66}Cr_{0.34})(O_{0.85}N_{0.15})$ and $(Al_{0.62}Cr_{0.38})_2O_3$ layers, when using the nomenclature of the oxynitrides prepared with similar conditions), exhibit different DC as well as TGA curves. The multilayers with smooth layer-transitions (ML-smooth) shows almost no mass-loss even up to 1500 °C, actually very similar to our $(Al_{0.62}Cr_{0.38})_2O_3$ (ON-275). However, the multilayer with steep layer-transition (ML-steep) shows a distinct mass-loss with an onset temperature of ~1260 °C and an endothermic features with two distinct peaks. This multilayer has an overall N-to-(O+N) ratio of ~0.23, whereas the other one has only 0.14. Consequently, their different behaviour is not that surprising, but more important is that the multilayer with smooth layer-transitions (exhibition an N-to-(O+N) ratio of ~0.14) shows a significant lower mass-loss up to 1500 °C than the oxynitride with a comparable overall N-content $(Al_{0.66}Cr_{0.34})(O_{0.85}N_{0.15})$ (ON-125).

When performing these treatments in synthetic air, the individual processes are superimposed by oxidation reactions (especially of the N-partners). These can be nicely seen in the DSC and TGA curves, especially for the highest N-containing oxynitride, $(Al_{0.64}Cr_{0.36})(O_{0.2}N_{0.8})$ (ON-50), Fig. 8.6a and b, respectively. The TGA signals show a mass-gain, starting at ~750 °C for all coatings, and a mass-loss at higher temperatures. The mass-loss shifts to higher temperatures with lower N content, in agreement with the

studies in inert atmosphere. Except for the highest N-containing coating, $(Al_{0.64}Cr_{0.36})(O_{0.2}N_{0.8})$ (ON-50), all others have reached their fully oxidized state with $T_a = 1300$ °C, as here no further mass change or DSC features can be detected. The $(Al_{0.64}Cr_{0.36})(O_{0.2}N_{0.8})$ oxynitride (ON-50) shows a significant increasing mass for $T_a > 1230$ °C, due to the oxidation of the former metallic N-bonding-partners. At around 1400 °C also this coating is fully oxidized, indicated by the stable TGA and DSC curves. Again, the multilayer with smooth layer-transitions outperforms that with steep layer-transitions, as suggested by the lower but also postponed mass-loss, see Fig. 8.6. This is also in agreement with the total mass-gain of out coatings up to 1500 °C, which increases with their initial N-content.

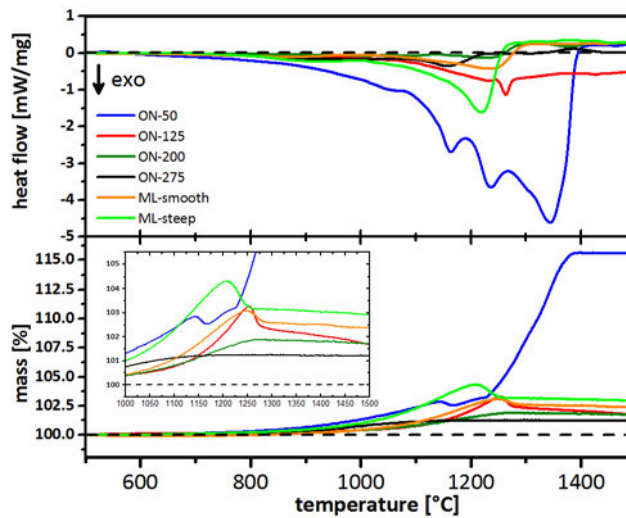Fig. 8.6: DSC and TGA signals of of $(Al_{0.64}Cr_{0.36})(O_{0.2}N_{0.8})$, $(Al_{0.66}Cr_{0.34})(O_{0.85}N_{0.15})$, $(Al_{0.66}Cr_{0.34})(O_{1.0}N_{0.0})$, and $(Al_{0.62}Cr_{0.38})_2O_3$ coatings, and the multilayers with a steep and smooth transition between their $(Al_{0.66}Cr_{0.34})(O_{0.85}N_{0.15})$ and $(Al_{0.62}Cr_{0.38})_2O_3$ layers (ML-steep and ML-smooth) during dynamical heating in synthetic air up to 1500 °C.

The general structure evolution of our coatings from their as deposition state during annealing in He or synthetic air is presented in Fig. 8.7a, b, and c, respectively, by corresponding XRD patterns. The XRD patterns of our as deposited free-standing coating samples (removed from their substrates, Fig. 8.7a) agree with those of our as deposited samples on Si substrates, presented in Fig. 8.2. The N-richest oxynitride, $(Al_{0.64}Cr_{0.36})(O_{0.2}N_{0.8})$ (ON-50), basically exhibits a fcc-$Al_xCr_{1-x}N$-based structure, whereas the structure of the other oxynitrides, $(Al_{0.66}Cr_{0.34})(O_{0.85}N_{0.15})$ (ON-125), $(Al_{0.66}Cr_{0.34})(O_{1.0}N_{0.0})$ (ON-200), and $(Al_{0.62}Cr_{0.38})_2O_3$ (ON-275), is composed of an fcc-$(Al_xCr_{1-x})_2O_3$-based phase with increasing α-$(Al_xCr_{1-x})_2O_3$-based phase fraction for decreased N-contents, see Fig. 8.7a. The multilayers are also basically composed of fcc-$(Al_xCr_{1-x})_2O_3$-based phases, with XRD peak positions (between fcc-$Al_xCr_{1-x}N$ and fcc-$(Al_xCr_{1-x})_2O_3$) according to their N-content, see Table 8.1.

After annealing in He to 1500 °C, the N-richest oxynitride, $(Al_{0.64}Cr_{0.36})(O_{0.2}N_{0.8})$ (ON-50), transformed from a basically single-phase fcc structure to a material composed of w-AlN, α-Al_2O_3, and bcc-Cr, see Fig. 8.7b. The lower N-containing oxynitride, $(Al_{0.66}Cr_{0.34})(O_{0.85}N_{0.15})$ (ON-125), which is also mainly single-phase fcc-structured (but here, more according to fcc-$(Al_xCr_{1-x})_2O_3$), transformed towards α-$(Al,Cr)_2O_3$, fcc-$(Al,Cr)N$, and bcc-Cr. Also the oxynitride $(Al_{0.66}Cr_{0.34})(O_{1.0}N_{0.0})$ (ON-200), with a N-content below the detection limit of our EDS, exhibits an fcc-$(Al,Cr)N$ phase next to α-$(Al,Cr)_2O_3$ after annealing in He to 1500 °C. But here, no bcc-Cr can be detected. This is in contrast to the oxynitride prepared with the highest synthetic air flow p.a.s., $(Al_{0.62}Cr_{0.38})_2O_3$ (ON-275), which contains no fcc-$(Al,Cr)N$ phase but bcc-Cr after annealing to 1500 °C, in He, Fig. 8.7b. This could be based on their slightly higher metal-to-oxygen ratio (slightly above 2/3) and higher Cr content, see also.

Also here, the two different multilayers, with either steep or smooth layer-transition, exhibit a different behaviour. The multilayer with steep layer-transition exhibits metallic bcc-Cr and small fractions of hcp-Cr_2N, next to the dominating α-$(Al,Cr)_2O_3$ phases after annealing in He. In contrast, the multilayer with smooth layer-transitions basically shows only α-$(Al,Cr)_2O_3$ and fcc-$(Al,Cr)N$ phases after annealing in He up to 1500 °C, which is in agreement to the corresponding DSC and especially TGA measurements, Fig. 8.5, where no significant mass-loss, (due to the dissociation of CrN to Cr_2N to Cr via N_2-release) is detected. Furthermore, their α-$(Al,Cr)_2O_3$ phases seem to have a higher Cr content resolved as indicated by the corresponding XRD peak position which are closer to α-$(Al,Cr)_2O_3$ than those of the multilayer with originally steep layer-transitions, where the corresponding XRD peak positions are actually closer to α-Al_2O_3 (please compare ML-smooth with ML-steep in Fig. 8.7b).

The XRD patterns of all our oxynitrides and multilayers, after oxidising in synthetic air up to 1500 °C, Fig. 8.7c, exhibit only fractions of corundum-type α-Al_2O_3 or α-$(Al,Cr)_2O_3$.

The coatings with the highest N-contents, the $(Al_{0.64}Cr_{0.36})(O_{0.2}N_{0.8})$ (ON-50) oxynitride and the multilayers with steep layer-transitions, show the formation of Al- and Cr-rich α-$(Al,Cr)_2O_3$ based phases (indicated by the double peak nature of the corresponding

XRD peaks). We envision, that Cr (from the dissociation of Cr–N bonds) is incorporated to the neighbouring $(Al,Cr)_2O_3$ layers and/or forms volatile Cr-oxides, whereas the remaining Al-rich phases will be transferred to α-Al_2O_3.
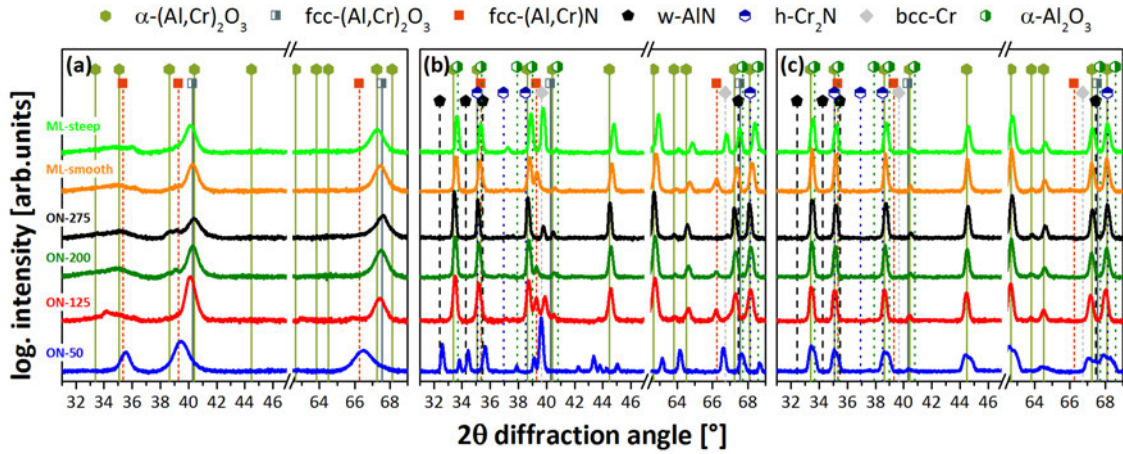
Fig. 8.7: XRD measurements of of free standing (powder-like) oxynitrides, $(Al_{0.64}Cr_{0.36})(O_{0.2}N_{0.8})$ (ON-50), $(Al_{0.66}Cr_{0.34})(O_{0.85}N_{0.15})$ (ON-125), $(Al_{0.66}Cr_{0.34})(O_{1.0}N_{0.0})$ (ON-200), and $(Al_{0.62}Cr_{0.38})_2O_3$ (ON-275), and multilayers with a steep and smooth transition between their $(Al_{0.66}Cr_{0.34})(O_{0.85}N_{0.15})$ and $(Al_{0.62}Cr_{0.38})_2O_3$ layers (ML-steep and ML-smooth). (a) as deposited state, (b) after annealing in He to 1500 °C, and (c) after annealing in synthetic air to 1500 °C.

8.4 Summary and conclusions

Various $(Al_xCr_{1-x})(O_{1-y}N_y)$ oxynitrides with different N-nonmetal-fractions (i.e., N/O+N, y) and their multi-layered arrangements were developed by varying the synthetic air flow (without any other gas addition) during arc evaporation of powder metallurgical prepared $Al_{0.7}Cr_{0.3}$ cathodes.

The $(Al_xCr_{1-x})(O_{1-y}N_y)$ oxynitride coatings crystallize with a single-phase face centred cubic fcc-(Al,Cr)N-based structure for $y \geq 0.8$, and with a phase composition of fcc-$(Al,Cr)_2O_3$-like and corundum type α-$(Al,Cr)_2O_3$-based structures for $y < 0.8$. Combining $(Al_xCr_{1-x})(O_{1-y}N_y)$ layers with $y = 0.15$ and ~0.0 to form multilayers with bilayer periods of ~20 nm leads to fcc dominated microstructures for smooth as well as steep layer-transitions.

The hardness of our as deposited $(Al_xCr_{1-x})(O_{1-y}N_y)$ oxynitrides, decreases from ~33 to 15 GPa with decreasing y from 0.8 to 0, while the multilayers have a hardness of ~26 GPa.

The onset temperature T_{onset} for thermally induced dissociation of Cr–N bonds of our oxynitrides, to finally form Cr under N_2-release, significantly increases from ~1000 to 1300 °C with decreasing N-content y from 0.8 to 0.15. When preparing the multilayer with smooth layer-transition no mass-loss can be detected (up to the maximum temperature of 1500 °C), whereas those with steep layer-transitions (due to N_2-release) with T_{onset} ~ 1250 °C. Dynamic oxidation treatments of our coatings in synthetic air up to 1500 °C, clearly show exceptionally increased resistance with decreasing nitrogen content y.

Based on our results we can conclude, that by varying the synthetic air flow during arc evaporation of Al-Cr cathodes (here, $Al_{0.7}Cr_{0.3}$), $(Al_xCr_{1-x})(O_{1-y}N_y)$ oxynitrides with $y \leq 0.8$ can be prepared, having excellent mechanical properties and thermal stabilities. Periodically alternating the synthetic air flow during arc evaporation of these Al-Cr cathodes, furthermore allows for the preparation of $(Al_xCr_{1-x})(O_{1-y}N_y)$ multilayers with modulated N and O contents, y.

9. Summary and Contribution to the field

This extensive study of AlCr-based nitride [$(Al_x,Cr_{1-x})N$], oxide [$(Al_xCr_{1-x})_2O_3$], and oxynitride [$(Al_xCr_{1-x})(O_{1-y}N_y)$] coatings highlights the tremendous impact of the reactive gas conditions on the coating properties. Here, especially the impact of different types of reactive gases (O_2, N_2, and synthetic air), their distribution during the deposition process, and flow rate on coating architecture, interface geometry (for multilayers), chemical composition, microstructure, mechanical properties, and thermal stabilities are studied in detail.

Although $Al_xCr_{1-x}N$, $(Al_xCr_{1-x})_2O_3$, and $(Al_xCr_{1-x})(O_{1-y}N_y)$ coatings are nowadays used in a multitude of different industrial applications, little is known about the impact of their chemical composition and architecture on their thermo-mechanical properties. Therefore, this is the major topic of this thesis:

A series of $(Al,Cr)N/(Al,Cr)_2O_3$ multilayer coatings with three different interface designs and altered layer architecture (overall interface volume fraction) was deposited by reactive cathodic arc evaporation. The multilayer arrangement was realised by alternatively processing two (out of four) neighbouring cathodes in nitrogen and oxygen atmosphere. Variations in the interface volume fraction were realised by reducing the active source time from 145, 60, to 30 s, resulting in decreasing bilayer periods from 175 to 30 nm. The different interface geometries (namely distinct, hybrid, and blurred) were established through reactive gas-exchange variations between the individual nitrogen and oxygen processes. As a result of the different bonding character at the interfaces— i.e. the transition from oxide to nitride and vice versa—a higher interface volume fraction also results in increased oxygen contents, whereas no clear relation to the interface geometry is given. However, all multilayers were grown in a cubic (fcc) structure with a pronounced (200) and (220) orientation. By decreasing the individual $(Al,Cr)N$ and $(Al,Cr)_2O_3$ layer thickness, hence increasing overall interface volume fraction, not only higher surface qualities can be obtained, but also a significant improvement in mechanical properties. Their hardness increase from ~14, ~16, and ~19 GPa approximately 22 GPa for blurred, hybrid, and distinct interface geometries, respectively. Based on these results we can conclude, that the alternating arrangement of $(Al,Cr)N/(Al,Cr)_2O_3$ multilayer films with different interface architectures represent a

promising approach to tailor specific coating properties towards application driven needs. The interface volume fraction is most essential in terms of mechanical properties.

Furthermore, monolithically grown $(Al_xCr_{1-x})_2O_3$ and $Al_xCr_{1-x}N/(Al_xCr_{1-x})_2O_3$ multilayer coatings, which were synthesised by reactive arc evaporation using powder metallurgical prepared $Al_{0.7}Cr_{0.3}$ targets were investigated with respect to their thermal stability and phase evolution during annealing in vacuum and inert atmospheres. While for powder annealed $(Al_xCr_{1-x})_2O_3$, the cubic $(Al,Cr)_2O_3$ phase transforms into the corundum-type $(Al,Cr)_2O_3$ solid solution at ~1050 °C, which remains stable up to 1600 °C, a significant change of the latter was found for $(Al_xCr_{1-x})_2O_3$ deposited on Al_2O_3 substrates after annealing at elevated temperatures for 1 h. Dissociation of the corundum-type $(Al,Cr)_2O_3$ solid solution to α-Al_2O_3 and volatile chromium oxides can be approved by XRD and TEM investigations. Investigations on powder as well as Al_2O_3 substrates, indicate the formation and evaporation of volatile chromium-oxides also for $Al_xCr_{1-x}N/(Al_xCr_{1-x})_2O_3$ multilayer coatings. DSC/TGA results point out that in the case of the multilayers, the thermal stability increases, with higher number of bilayers, regardless of their interface types (distinct or blurred). The decomposition of CrN into h-Cr_2N and further to c-Cr, via N_2 release, can be therefore retarded up to ~1200 °C. Hence, a multi-layer arrangement with optimized bilayer period is superior to the monolithically grown $Al_xCr_{1-x}N$ and $(Al_xCr_{1-x})_2O_3$ counterparts, deposited under similar conditions.

To verify the benefit of a multilayer arrangement with specific tailored architecture and interfaces, a similar study on arc evaporated $(Al_xCr_{1-x})(O_{1-y}N_y)$ coatings was carried out. Therefore, a cathodic arc evaporated monolithically grown gradient-layer—with a continuous transition from (Al,Cr)N to $(Al,Cr)_2O_3$ and back to (Al,Cr)N—was synthesised using powder metallurgically prepared $Al_{0.7}Cr_{0.3}$ targets. The transition zone from nitride to oxide was investigated in detail by TEM-SAED and STEM-EDS, to understand the structural and chemical evolution taking place through continuous transitions or blurred interfaces between individual (Al,Cr)N and $(Al,Cr)_2O_3$ layers.

This information was used to deposit the $(Al_xCr_{1-x})(O_{1-y}N_y)$ films with specifically tailored –structural and chemical properties and studied in detail for their thermal stability.

DSC/TGA results again point out that in the case of (Al,Cr)(O,N), the thermal stability increases, with increasing O content. The decomposition of CrN into h-Cr_2N and subsequently to c-Cr, via N_2 release, can be successfully retarded from ~1090 to 1150 °C. Thus, only 50 °C lower than the onset temperature for the before mentioned multilayer arrangement of individual (Al,Cr)N and $(Al,Cr)_2O_3$ layers.

Consequently, a multilayer arrangement with a high interface fraction and blurred interfaces between the individual nitride and oxide layers is preferred for increased thermal stability. Hence, (Al,Cr)(O,N) multilayers with many individual nitrogen-rich and oxygen-rich (Al,Cr)(O,N) layers are superior (in thermal stability) to multilayers with individual distinct separated (Al,Cr)N and $(Al,Cr)_2O_3$ layers.

Based on these results, monolithically grown as well as multi-layered $(Al_xCr_{1-x})(O_{1-y}N_y)$

coatings (with alternating N and O contents) were developed by variations of the synthetic air flow rates during reactive arc evaporation of $Al_{0.7}Cr_{0.3}$ targets. Using synthetic air as reactive gas immediately results in at least two major positive points:

1) The same magnetic systems (behind the cathodes) can be used to prepare the individual nitrogen-rich as well as oxygen-rich layers, which immediately allows to use all cathodes for the preparation of the individual layers. If different magnetic systems are used (necessary when operating in N_2 or O_2 atmosphere), this also limits the number of cathodes for the individual layers.

2) The process control itself (e.g., arc behaviour and cathode poisoning effects) becomes easier. When operating in N_2 or O_2 atmosphere, the process window for stable deposition parameters is smaller.

Monolithically grown N-rich $(Al_xCr_{1-x})(O_{1-y}N_y)$ coatings as well as multilayers composed of O-rich and N-rich $(Al_xCr_{1-x})(O_{1-y}N_y)$ layers are single-phased face-centred cubic structured, while monolithically grown O-rich $(Al_xCr_{1-x})(O_{1-y}N_y)$ coatings contain hexagonal and cubic structured phases. Therefore, the hardness of the monolithically grown $(Al_xCr_{1-x})(O_{1-y}N_y)$ coatings decreases from ~33 to 15 GPa with increasing oxygen content (realized by an increasing synthetic air flow rate), and the multilayers exhibit a relatively high hardness of ~26 GPa.

Contrary to the mechanical properties, the thermal stability of the monolithically grown $(Al_xCr_{1-x})(O_{1-y}N_y)$ coatings significant increases with increasing oxygen content. The typically observed two-step decomposition process of N-rich $(Al_xCr_{1-x})(O_{1-y}N_y)$ coatings (due to the decomposition of Cr–N to Cr_2N, and further to Cr, via release of N_2) reduces to a retarded one-step process at elevated temperatures for $(Al_xCr_{1-x})(O_{1-y}N_y)$ coatings with at least ~90 at.% on the non-metallic sublattice. The multilayers composed of O-rich and N-rich $(Al_xCr_{1-x})(O_{1-y}N_y)$ layers, prepared by simply alternatingly varying the synthetic air flow rate nearly show no mass loss (hence, no N_2-release and associated Cr–N decomposition) upon annealing in He atmosphere to 1500 °C. Consequently, even after annealing in He up to 1500 °, these multilayers are mainly composed of face-centred cubic structured -(Al,Cr)N phases and corundum-type α-$(Al,Cr)_2O_3$.

The here presented results clearly demonstrate the impact and beneficial effects of reactive gases (e.g., N_2, O_2, and synthetic air) and their exchange variations during deposition (using powder metallurgical prepared $Al_{0.7}Cr_{0.3}$ targets) on architecturally-designed Al-Cr-based nitride/oxide and oxynitride coatings in terms of high temperature treatments and applications

CHAPTER **10**

10. Acknowledgment for financial and scientific support

CHAPTER **11**

11. References

[1] W.D. Callister, D.G. Rethwisch, Materialwissenschaften und Werkstofftechnik: Eine Einführung, 1. Auflage, Wiley-VCH Verlag & Co. KGaA, 2013.

[2] P.H. Mayrhofer, Materials Science of Metallic Materials 308.862 WS 2016, (2016).

[3] M. Stüber, S. Ulrich, H. Leiste, H. Holleck, Magnetron sputtered nanocrystalline metastable (V,Al)(C,N) hard coatings, Surf. Coatings Technol. 206 (2011) 610–616. doi:10.1016/j.surfcoat.2011.07.052.

[4] H. Holleck, Material selection for hard coatings, J. Vac. Sci. Technol. A Vacuum, Surfaces, Film. 4 (1986) 2661–2669.

[5] H. Holleck, Metastable coating - prediction of composition and structure, Surf. Coatings Technol. 36 (1988) 151–159.

[6] H. Holleck, Designing advanced coatings for wear protection, Surf. Eng. 7 (1991) 137–144.

[7] H. Holleck, Schier, V, Multilayer PVD coatings for wear protection, Surf. Coatings Technol. 76 (1995) 328–336.

[8] C.M. Koller, Triggering the Phase Evolution within TiAlN- and $(Al_{1-x}Cr_x)_2O_3$-based Hard Coatings by Alloying and Microstructural Concepts, (2015).

[9] C.M. Koller, The Influence of Fe-doping on Mechanical Properties and Thermal Stability of Arc Evaporated Al-Cr-O Coatings, (2016).

[10] D.A. Porter, K.E. Easterling, M. Sherif, Phase Transformations in Metals and Alloys, (Revised Reprint), CRC press, 2009.

[11] H. Mehrer, Diffusion in solids: fundamentals, methods, materials, diffusion-controlled processes, Springer Science & Business Media, 2007.

[12] M. A, J.S. Burnell-Gray, P.K. Datta, Surface Engineering Casebook: Solutions to Corrosion and Wear-related Failures, Elsevier, 1996.

[13] M.G. Hocking, V. Vasantasree, P.S. Sidky, Metallic and Ceramic Coatings: Production, High-Temperature Properties, and Applications, (1988).

[14] O. Knotek, F. Löffler, C. Barimani, G. Kraemer, Hard Coatings for Cutting and Forming Tools by PVD Arc Processes, Mater. Sci. Forum. 246 (1997) 29–60.

doi:10.4028/www.scientific.net/MSF.246.29.

[15] P.M. Martin, Handbook of deposition technologies for films and coatings: science, applications and technology, William Andrew, 2009.

[16] M. Ohring, Materials science of thin films, Academic press, 2001.

[17] L.B. Freund, S. Suresh, Thin Film Materials, Defect Form. Surf. Evol. (2003) 7–12.

[18] P.H. Mayrhofer, Surface Technology 308.875 SS 2015, (2015).

[19] A. Anders, Cathodic Arcs: From Fractal Spots to Energetic Condensation, New York: Springer, 2008. doi:10.1007/978-0-387-79108-1.

[20] J. Ramm, M. Ante, T. Bachmann, B. Widrig, H. Brändle, M. Döbeli, Pulse enhanced electron emission (P3e^{TM}) arc evaporation and the synthesis of wear resistant Al-Cr-O coatings in corundum structure, Surf. Coatings Technol. 202 (2007) 876–883. doi:10.1016/j.surfcoat.2007.05.044.

[21] J. Ramm, M. Ante, H. Brändle, A. Neels, A. Dommann, M. Döbeli, Thermal stability of thin film corundum-type solid solutions of $(Al_{1-x}Cr_x)_2O_3$ synthesized under low-temperature non-equilibrium conditions, Adv. Eng. Mater. 9 (2007) 604–608. doi:10.1002/adem.200700081.

[22] C.M. Koller, Thermal Stability and Oxidation Resistance of Ti-Al-N/Ta-Al-N Multilayers, (2012).

[23] J. R. Franz, F. Mendez Martin, G. Hawranek, P. Polcik, Erosion behaviour of composite Al-Cr cathodes in cathodic arc plasmas in inert and reactive atmospheres, Vac. Sci. Technol. A Vacuum, Surfaces, Film. 34, 021304 (2016).

[24] C.M. Koller, J. Ramm, S. Kolozsvári, J. Paulitsch, P.H. Mayrhofer, Role of droplets and iron on the phase formation of arc evaporated Al-Cr-oxide coatings, Surf. Coatings Technol. 276 (2015) 735–742. doi:10.1016/j.surfcoat.2015.05.012.

[25] J.A. Venables, Nucleation and growth of thin films: recent progress, Vacuum. 33 (1983) 701–705.

[26] D.M. Mattox, Particle bombardment effects on thin-film deposition: A review, J. Vac. Sci. Technol. A Vacuum, Surfaces, Film. 7 (1989) 1105–1114.

[27] W. Ensinger, The influence of ion irradiation during film growth on the chemical stability of film/substrate systems, Surf. Coatings Technol. 80 (1996) 35–48.

[28] W. Ensinger, Low energy ion assist during deposition - an effective tool for controlling thin film microstructure, Nucl. Instruments Methods Phys. Res. Sect. B Beam Interact. with Mater. Atoms. 127 (1997) 796–808.

[29] V. Edlmayr, M. Pohler, I. Letofsky-Papst, C. Mitterer, Microstructure and thermal stability of corundum-type $(Al_{0.5}Cr_{0.5})_2O_3$ solid solution coatings grown by cathodic arc evaporation, Thin Solid Films. 534 (2013) 373–379. doi:10.1016/j.tsf.2013.02.046.

[30] H. Willmann, P.H.M. Rhofer, P.O.Å. Persson, A.E. Reiter, L. Hultman, C. Mitterer, Thermal stability of Al–Cr–N hard coatings, Scr. Mater. 54 (2006) 1847–1851. doi:10.1016/j.scriptamat.2006.02.023.

[31] P.H. Mayrhofer, H. Willmann, L. Hultman, C. Mitterer, Influence of different atmospheres on the thermal decomposition of Al-Cr-N coatings, J. Phys. D. Appl. Phys. 41 (2008) 155316. doi:10.1088/0022-3727/41/15/155316.

[32] C.M. Koller, R. Hollerweger, C. Sabitzer, R. Rachbauer, S. Kolozsvári, J. Paulitsch, et al., Thermal stability and oxidation resistance of arc evaporated TiAlN, TaAlN, TiAlTaN, and TiAlN/TaAlN coatings, Surf. Coatings Technol. 259 (2014) 599–607. doi:10.1016/j.surfcoat.2014.10.024.

[33] C. Sabitzer, J. Paulitsch, S. Kolozsvári, R. Rachbauer, P.H. Mayrhofer, Impact of bias potential and layer arrangement on thermal stability of arc evaporated Al-Cr-N coatings, Thin Solid Films. 610 (2016) 26–34. doi:10.1016/j.tsf.2016.05.011.

[34] P.H. Mayrhofer, A. Hörling, L. Karlsson, J. Sjölén, T. Larsson, M. Christian, Self-organized nanostructures in the Ti-Al-N system Self-organized nanostructures in the Ti–Al–N system, 2049 (2011). doi:10.1063/1.1608464.

[35] R. Rachbauer, E. Stergar, S. Massl, M. Moser, P.H. Mayrhofer, Three-dimensional atom probe investigations of Ti-Al-N thin films, Scr. Mater. 61 (2009) 725–728.

[36] A. Kirnbauer, Diploma Thesis: Impact of Fe on the oxide phase formation and oxidation behaviour of cathodic arc evaporated Al-Cr films, (2017).

[37] J.W. Martin, Precipitation hardening: theory and applications, Butterworth-Heinemann, 2012.

[38] B.A. Movchan, A. V Demchishin, STRUCTURE AND PROPERTIES OF THICK CONDENSATES OF NICKEL, TITANIUM, TUNGSTEN, ALUMINUM OXIDES, AND ZIRCONIUM DIOXIDE IN VACUUM., Fiz. Met. Met. 28 653-60 (Oct 1969). (1969).

[39] J.A. Thornton, Influence of apparatus geometry and deposition conditions on the structure and topography of thick sputtered coatings, J. Vac. Sci. Technol. 11 (1974) 666–670.

[40] R. Messier, A.P. Giri, R.A. Roy, Revised structure zone model for thin film physical structure, J. Vac. Sci. Technol. A Vacuum, Surfaces, Film. 2 (1984) 500–503.

[41] A. Anders, A structure zone diagram including plasma-based deposition and ion etching, Thin Solid Films. 518 (2010) 4087–4090.

[42] A. Sugishima, H. Kajioka, Y. Makino, Phase transition of pseudobinary Cr–Al–N films deposited by magnetron sputtering method, Surf. Coat. Technol. 97 (1997) 590–594. doi:10.1016/S0257-8972(97)00402-7.

[43] Y. Makino, K. Nogi, Synthesis of pseudobinary Cr–Al–N films with B1 structure by rf-assisted magnetron sputtering method, Surf. Coat. Technol. 98 (1998) 1008–1012. doi:10.1016/S0257-8972(97)00391-5.

[44] P.H. Mayrhofer, D. Music, T. Reeswinkel, H.G. Fuß, J.M. Schneider, Structure, elastic properties and phase stability of $Cr_{1-x}Al_xN$, Acta Mater. 56 (2008) 2469–2475. doi:10.1016/j.actamat.2008.01.054.

[45] V. Moraes, H. Riedl, R. Rachbauer, S. Kolozsvári, M. Ikeda, L. Prochaska, et al., Thermal conductivity and mechanical properties of AlN-based thin films, 225304 (2016). doi:10.1063/1.4953358.

[46] A.E. Reiter, V.H. Derflinger, B. Hanselmann, T. Bachmann, B. Sartory, Investigation of the properties of $Al_{1-x}Cr_xN$ coatings prepared by cathodic arc evaporation, Surf. Coatings Technol. 200 (2005) 2114–2122. doi:10.1016/j.surfcoat.2005.01.043.

[47] F. Rovere, P.H. Mayrhofer, Thermal stability and thermo-mechanical properties of magnetron sputtered Cr-Al-Y-N coatings, J. Vac. Sci. Technol. A Vacuum, Surfaces, Film. 26 (2008) 29. doi:10.1116/1.2806943.

[48] C. Sabitzer, J. Paulitsch, S. Kolozsvári, R. Rachbauer, P.H. Mayrhofer, Influence of bias potential and layer arrangement on structure and mechanical properties of arc evaporated Al-Cr-N coatings, Vacuum. 106 (2014) 49–52. doi:10.1016/j.vacuum.2014.03.006.

[49] A. E. Reiter, C. Mitterer, B. Sartory, Oxidation of arc-evaporated $Al_{1-x}Cr_xN$ coatings, J. Vac. Sci. Technol. A Vacuum, Surfaces, Film. 25 (2007) 711. doi:10.1116/1.2738492.

[50] J. Lin, B. Mishra, J.J. Moore, W.D. Sproul, A study of the oxidation behavior of CrN and CrAlN thin films in air using DSC and TGA analyses, Surf. Coatings Technol. 202 (2008) 3272–3283. doi:10.1016/j.surfcoat.2007.11.037.

[51] H. Willmann, Al-Cr-N thin film design for high temperature applications, (2007).

[52] P.H. Mayrhofer, H. Willmann, A. E. Reiter, Structure and phase evolution of Cr-Al-N coatings during annealing, Surf. Coatings Technol. 202 (2008) 4935–4938. doi:10.1016/j.surfcoat.2008.04.075.

[53] M. Kathrein, W. Schintlmeister, W. Wallgram, U. Schleinkofer, Doped CVD Al_2O_3 coatings for high performance cutting tools, 164 (2003) 181–188.

[54] V. Edlmayr, M. Moser, C. Walter, C. Mitterer, Thermal stability of sputtered Al_2O_3 coatings, Surf. Coatings Technol. 204 (2010) 1576–1581. doi:10.1016/j.surfcoat.2009.10.002.

[55] C.M. Koller, J. Ramm, S. Kolozsvári, F. Munnik, J. Paulitsch, P.H. Mayrhofer, Corundum-type Fe-doped cathodic arc evaporated Al–Cr–O coatings, Scr. Mater. 97 (2015) 49–52. doi:10.1016/j.scriptamat.2014.10.037.

[56] G. Rollmann, A. Rohrbach, P. Entel, J. Hafner, First-principles calculation of the structure and magnetic phases of hematite, Phys. Rev. B. 69 (2004) 165107.

[57] H. Okamoto, Al-Cr (Aluminum-Chromium), J. Phase Equilibria Diffus. 29 (2008) 112–113. doi:10.1007/s11669-007-9225-4.

[58] S.S. Kim, T.H. Sanders, Thermodynamic Modeling of the Isomorphous Phase Diagrams in the, 84 (2001) 1881–1884.

[59] L. de Abreu Vieira, M. Döbeli, A. Dommann, E. Kalchbrenner, A. Neels, J. Ramm, et al., Approaches to influence the microstructure and the properties of Al-Cr-O layers synthesized by cathodic arc evaporation, Surf. Coatings Technol. 204 (2010) 1722–1728. doi:10.1016/j.surfcoat.2009.10.055.

[60] D. Diechle, M. Stueber, H. Leiste, S. Ulrich, Combinatorial approach to the growth of α-$(Al_{1-x},Cr_x)_{2+\delta}(O_{1-y},N_y)_3$ solid solution strengthened thin films by reactive r.f. magnetron sputtering, Surf. Coatings Technol. 206 (2011) 1545–

1551. doi:10.1016/j.surfcoat.2011.06.052.

[61]   M. Stueber, D. Diechle, H. Leiste, S. Ulrich, Synthesis of Al-Cr-O-N thin films in corundum and f.c.c. structure by reactive r.f. magnetron sputtering, Thin Solid Films. 519 (2011) 4025–4031. doi:10.1016/j.tsf.2011.01.144.

[62]   K. Pedersen, J. Bøttiger, M. Sridharan, M. Sillassen, P. Eklund, Texture and microstructure of Cr_2O_3 and $(Cr,Al)_2O_3$ thin films deposited by reactive inductively coupled plasma magnetron sputtering, Thin Solid Films. 518 (2010) 4294–4298. doi:10.1016/j.tsf.2010.01.008.

[63]   A. Khatibi, J. Palisaitis, C. Höglund, A. Eriksson, P.O.Å. Persson, J. Jensen, et al., Face-centered cubic $(Al_{1-x}Cr_x)_2O_3$, Thin Solid Films. 519 (2011) 2426–2429. doi:10.1016/j.tsf.2010.11.052.

[64]   P.Y. Hou, Thermally grown Al_2O_3 on a H_2-annealed Fe_3Al alloy : Stress evolution and film adhesion, 55 (2007) 5601–5613. doi:10.1016/j.actamat.2007.06.018.

[65]   A. Khatibi, J. Lu, J. Jensen, P. Eklund, L. Hultman, Phase transformations in face centered cubic $(Al_{0.32}Cr_{0.68})_2O_3$ thin films, Surf. Coatings Technol. 206 (2012) 3216–3222. doi:10.1016/j.surfcoat.2012.01.008.

[66]   A. Khatibi, Growth and Heat Treatment Studies of Al-Cr-O and Al-Cr-O-N Thin Films, 2013.

[67]   H. Najafi, A. Karimi, P. Dessarzin, M. Morstein, Correlation between anionic substitution and structural properties in $AlCr(O_xN_{1-x})$ coatings deposited by lateral rotating cathode arc PVD, Thin Solid Films. 520 (2011) 1597–1602. doi:10.1016/j.tsf.2011.08.075.

[68]   H. Najafi, a. Karimi, D. Alexander, P. Dessarzin, M. Morstein, Effects of Si and Y in structural development of $(Al,Cr,Si/Y)O_xN_{1-x}$ thin films deposited by magnetron sputtering, Thin Solid Films. 549 (2013) 224–231. doi:10.1016/j.tsf.2013.06.062.

[69]   C.M. Koller, N. Koutná, J. Ramm, S. Kolozsvári, J. Paulitsch, D. Holec, et al., First principles studies on the impact of point defects on the phase stability of $(Al_xCr_{1-x})_2O_3$ solid solutions First principles studies on the impact of point defects on the phase stability of $(Al_xCr_{1-x})_2O_3$ solid solutions, 25002 (2016) 1–9. doi:10.1063/1.4941573.

[70]   H. Najafi, a. Karimi, M. Morstein, Microstructure of $Al_{95.5}Cr_{2.5}Si_2(N_{1-x}O_x)$ thin films covering from nitrides to oxides, Surf. Coatings Technol. 205 (2011) 5199–5204. doi:10.1016/j.surfcoat.2011.05.031.

[71]   A. Khatibi, J. Sjölen, G. Greczynski, J. Jensen, P. Eklund, L. Hultman, Structural and mechanical properties of Cr–Al–O–N thin films grown by cathodic arc deposition, Acta Mater. 60 (2012) 6494–6507. doi:10.1016/j.actamat.2012.08.010.

[72]   H. Holleck, V. Schier, Multilayer PVD coatings for wear protection, Surf. Coat. Technol. 76–77 (1995) 328–336. doi:10.1016/0257-8972(95)02555-3.

[73]   S.J. Lloyd, J.M. Molina-Aldareguia, Multilayered materials : a palette for the materials artist, Phil. Trans. R. Soc. Lond. A 361. (2003) 2931–2949.

[74] M. Stueber, H. Holleck, H. Leiste, K. Seemann, S. Ulrich, C. Ziebert, Concepts for the design of advanced nanoscale PVD multilayer protective thin films, J. Alloys Compd. 483 (2009) 321–333. doi:10.1016/j.jallcom.2008.08.133.

[75] V. Chawla, D. Holec, P.H. Mayrhofer, Stabilization criteria for cubic AlN in TiN/AlN and CrN/AlN bi-layer systems, (2013). doi:10.1088/0022-3727/46/4/045305.

[76] C. Ducros, C. Cayron, F. Sanchette, Multilayered and nanolayered hard nitride thin films deposited by cathodic arc evaporation . Part 1 : Deposition , morphology and microstructure, 201 (2006) 136–142. doi:10.1016/j.surfcoat.2005.11.102.

[77] H. Högberg, J. Birch, M. Ode, Growth , structure , and mechanical properties of transition metal carbide superlattices, J. Mater. Res. (2001) 1301–1310.

[78] M. Setoyama, A. Nakayama, M. Tanaka, N. Kitagawa, T. Nomura, Formation of cubic-AIN in TiN/AIN superlattice, 87 (1996) 225–230.

[79] A. Madan, I.W. Kim, S.C. Cheng, P. Yashar, V.P. Dravid, S.A. Barnett, Stabilization of Cubic AlN in Epitaxial AlN/TiN Superlattices, (1997) 1743–1746.

[80] M. Schlögl, B. Mayer, J. Paulitsch, P.H. Mayrhofer, Influence of CrN and AlN layer thicknesses on structure and mechanical properties of CrN/AlN superlattices, Thin Solid Films. 545 (2013) 375–379. doi:10.1016/j.tsf.2013.07.026.

[81] M. Schlögl, C. Kirchlechner, J. Paulitsch, J. Keckes, P.H. Mayrhofer, Effects of structure and interfaces on fracture toughness of CrN/AlN multilayer coatings, Scr. Mater. 68 (2013) 917–920. doi:10.1016/j.scriptamat.2013.01.039.

[82] P. Li, L. Chen, S.Q. Wang, B. Yang, Y. Du, J. Li, et al., Int . Journal of Refractory Metals and Hard Materials Microstructure , mechanical and thermal properties of TiAlN / CrAlN multilayer coatings, RMHM. (2013) 1–7. doi:10.1016/j.ijrmhm.2013.01.020.

[83] L. Chen, Mechanical properties of (Ti,Al)N monolayer and TiN/(Ti,Al)N multilayer coatings, 25 (2007) 72–76. doi:10.1016/j.ijrmhm.2006.01.005.

[84] M. Schlögl, J. Paulitsch, J. Keckes, P.H. Mayrhofer, Influence of AlN layers on mechanical properties and thermal stability of Cr-based nitride coatings, Thin Solid Films. 531 (2013) 113–118. doi:10.1016/j.tsf.2012.12.057.

[85] Claudionico~commonswiki, Electron Interaction with Matter, (2013). https://commons.wikimedia.org/wiki/File:Electron_Interaction_with_Matter.svg (accessed April 19, 2017).

[86] W. Grogger, G. Kothleitner, 513.119 Experimentelles Praktikum - Transmissionselektronenmikroskopie, Graz, 2005.

[87] S.J. Pennycook, Transmission Electron Microscopy: A Textbook for Materials Science, David B. Williams and C. Barry Carter. Springer, New York, 2009, 932 pages. ISBN 978-0-387-76500-6 (Hardcover), ISBN 978-0-387-76502-0 (Softcover), Microsc. Microanal. 16 (2010) 111.

[88] W.C. Oliver, G.M. Pharr, An improved technique for determining hardness and elastic modulus using load and displacement sensing indentation experiments, J.

Mater. Res. 7, (1992) 1564-1580.

[89]   https://www.netzsch.com/de/,(2017).

[90]   V.S. Ramachandran, R.M. Paroli, J.J. Beaudoin, A.H. Delgado, Handbook of thermal analysis of construction materials, William Andrew, 2002.

[91]   M.E. Brown, P.K. Gallagher, Handbook of thermal analysis and calorimetry: recent advances, techniques and applications, Elsevier, 2011.

[92]   S. Coromant, Modern Metal Cutting. A practical handbook Tofters Tryckery AB, 1994, ISBN 91-972299-0-3, 1994.

[93]   J.C. Sánchez-López, Martínez-Martínez, C. D. López-Cartes, A. Fernández, M. Brizuela, A. García-Luis, et al., Mechanical behavior and oxidation resistance of Cr(Al)N coatings, J. Vac. Sci. Technol. A Vacuum, Surfaces, Film. 23 (2005) 681–686. doi:10.1116/1.1946711.

[94]   M. Kawate, A. Kimura, T. Suzuki, Microhardness and lattice parameter of $Cr_{1−x}Al_xN$ films, J. Vac. Sci. Technol. A Vacuum, Surfaces, Film. 20 (2002) 569. doi:10.1116/1.1448510.

[95]   E. Lugscheider, K. Bobzin, S. Bärwulf, T. Hornig, Oxidation characteristics and surface energy of chromium-based hardcoatings for use in semisolid forming tools, Surf. Coatings Technol. 133–134 (2000) 540–547. doi:10.1016/S0257-8972(00)00974-9.

[96]   J. Vetter, E. Lugscheider, S.S. Guerreiro, (Cr:Al)N coatings deposited by the cathodic vacuum are evaporation, Surf. Coatings Technol. 98 (1998) 1233–1239. doi:10.1016/S0257-8972(97)00238-7.

[97]   H. Willmann, Hardness evolution of Al–Cr–N coatings under thermal load, (2008). doi:10.1557/JMR.2008.0366.

[98]   H. Najafi, A. Karimi, P. Dessarzin, M. Morstein, Formation of cubic structured $(Al_{1−x}Cr_x)_{2+δ}O_3$ and its dynamic transition to corundum phase during cathodic arc evaporation, Surf. Coatings Technol. 214 (2013) 46–52. doi:10.1016/j.surfcoat.2012.10.062.

[99]   M. Pohler, R. Franz, J. Ramm, P. Polcik, C. Mitterer, Influence of pulsed bias duty cycle variations on structural and mechanical properties of arc evaporated $(Al,Cr)_2O_3$ coatings, Surf. Coatings Technol. 282 (2015) 43–51. doi:10.1016/j.surfcoat.2015.09.055.

[100] B. Rother, On the possibility of physical vapour deposition process design by coordinated substrate rotation modes, Surf. Coatings Technol. 64 (1994) 155–159. doi:10.1016/0257-8972(94)90102-3.

[101] C.M. Koller, S.A. Glatz, S. Kolozsvári, J. Ramm, P.H. Mayrhofer, Surface & Coatings Technology In fl uence of substrate bias on structure and mechanical properties of arc evaporated $(Al,Cr)_2O_3$ and $(Al,Cr,Fe)_2O_3$ coatings, Surf. Coat. Technol. 319 (2017) 386–393. doi:10.1016/j.surfcoat.2017.04.023.

[102] B. Navinšek, P. Panjan, I. Milošev, Industrial applications of CrN (PVD) coatings, deposited at high and low temperatures, Surf. Coatings Technol. 97 (1997) 182–191. doi:10.1016/S0257-8972(97)00393-9.

[103] W. Kalss, a. Reiter, V. Derflinger, C. Gey, J.L. Endrino, Modern coatings in high performance cutting applications, Int. J. Refract. Met. Hard Mater. 24 (2006) 399–404. doi:10.1016/j.ijrmhm.2005.11.005.

[104] L. He, L. Chen, Y. Xu, Y. Du, Thermal stability and oxidation resistance of $Cr_{1-x}Al_xN$ coatings with single phase cubic structure, J. Vac. Sci. Technol. A Vacuum, Surfaces, Film. 61513 (2015). doi:10.1116/1.4930424.

[105] J.M. Andersson, E.W.P.M. Helmersson, J.M. Andersson, E. Wallin, Energy distributions of positive and negative ions during magnetron sputtering of an Al target in mixtures Energy distributions of positive and negative ions during magnetron sputtering of an Al target in Ar / O 2 mixtures, 33305 (2006). doi:10.1063/1.2219163.

[106] P.H. Mayrhofer, F. Rovere, M. Moser, Thermally induced transitions of CrN thin films, 57 (2007) 249–252. doi:10.1016/j.scriptamat.2007.03.058.

[107] J. Sjölén, L. Karlsson, S. Braun, R. Murdey, A. Hörling, L. Hultman, Structure and mechanical properties of arc evaporated Ti–Al–O–N thin films, 201 (2007) 6392–6403. doi:10.1016/j.surfcoat.2006.12.006.

[108] W. Liu, X. Su, S. Zhang, H. Wang, J. Liu, L. Yan, Effect of the oxygen fraction on the structure and optical properties of HfO_xN_y thin films, 82 (2008) 1280–1284. doi:10.1016/j.vacuum.2008.01.053.

[109] M. Lumey, R. Dronskowski, Phase Prediction of the Oxynitrides of Vanadium , Niobium , and Tantalum, (2005) 887–893. doi:10.1002/zaac.200400535.

[110] J. Vetter, T. Krug, V. Von Der Heide, AlTiCrNO coatings for dry cutting deposited by reactive cathodic vacuum arc evaporation, 175 (2003) 615–619. doi:10.1016/S0257-8972.

[111] J. Ye, S. Ulrich, C. Ziebert, M. Stüber, Stress reduction of cubic boron nitride films by oxygen addition, Thin Solid Films. 517 (2008) 1145–1149. doi:10.1016/j.tsf.2008.07.019.

[112] J.-M. Chappé, N. Martin, J.F. Pierson, G. Terwagne, J. Lintymer, J. Gavoille, et al., Influence of substrate temperature on titanium oxynitride thin films prepared by reactive sputtering, 225 (2004) 29–38. doi:10.1016/j.apsusc.2003.09.028.

[113] P. Wilhartitz, S. Dreer, P. Ramminger, Can oxygen stabilize chromium nitride?— Characterization of high temperature cycled chromium oxynitride, 448 (2004) 289–295. doi:10.1016/S0040-6090(03)01066-6.

[114] M. Hirai, T. Suzuki, H. Suematsu, W. Jiang, K. Yatsui, M. Hirai, et al., Mechanism of hardening in Cr–Al–N–O thin films prepared by pulsed laser deposition Mechanism of hardening in Cr–Al–N–O thin films prepared by pulsed laser deposition, 947 (2003). doi:10.1116/1.1578656.

[115] J. Zhu, Z.G. Liu, L.Y. R, Pulsed laser deposited ZrAlON films for high-*k* gate dielectric applications, 1171 (2005) 1167–1171. doi:10.1007/s00339-004-3148-2.

[116] R. Cremer, M. Witthaut, K. Reichert, M. Schierling, D. Neuschutz, Thermal stability of Al–O–N PVD diffusion barriers, 109 (1998) 48–58.

[117] Y.C. Ee, Z. Chen, S.B. Law, S. Xu, Formation and characterization of Ti–Si–N–O barrier films, 504 (2006) 218–222. doi:10.1016/j.tsf.2005.09.127.

[118] F. Rene, Growth of thin , crystalline oxide , nitride and oxynitride ® lms on metal and metal alloy surfaces, (2000).

[119] L. Castaldi, D. Kurapov, a. Reiter, V. Shklover, P. Schwaller, J. Patscheider, Effect of the oxygen content on the structure, morphology and oxidation resistance of Cr-O-N coatings, Surf. Coatings Technol. 203 (2008) 545–549. doi:10.1016/j.surfcoat.2008.05.018.

[120] A. Khatibi, J. Lu, J. Jensen, P. Eklund, L. Hultman, Phase transformations in face centered cubic (Al0.32Cr0.68)2O3 thin films, Surf. Coatings Technol. 206 (2012) 3216–3222. doi:10.1016/j.surfcoat.2012.01.008.

[121] C.M. Koller, N. Koutná, J. Ramm, S. Kolozsvári, J. Paulitsch, First principles studies on the impact of point defects on the phase stability of First principles studies on the impact of point defects on the phase stability of $(Al_xCr_{1-x})_2O_3$ solid solutions, 25002 (2016). doi:10.1063/1.4941573.

[122] H. Riedl, C.M. Koller, A. Limbeck, J. Kala, P. Polcik, P.H. Mayrhofer, Oxidation behavior and tribological properties of multilayered Ti-Al-N/Mo-Si-B thin films, 129 (2015). doi:10.1116/1.4929536.

[123] R. Raab, SC, Surf. Coat. Technol. (2017). doi:10.1016/j.surfcoat.2017.05.039.

PUBLICATIONS

Publications included in the thesis

<u>R. Raab</u>, C.M. Koller, S. Kolozsvári, J. Ramm, P.H. Mayrhofer; *Influence of interface volume and geometry on structure and mechanical properties of arc evaporated Al-Cr-N/Al-Cr-O multilayer coatings*, manuscript accepted in Surface and Coatings Technology.

<u>R. Raab</u>, C.M. Koller, S. Kolozsvári, J. Ramm, P.H. Mayrhofer; *Thermal Stability of Arc Evaporated Oxide and Oxide/Nitride Coatings within the Systems Al-Cr-N and Al-Cr-O*, to be submitted for Surface and Coatings Technology.

<u>R. Raab</u>, C.M. Koller, S. Kolozsvári, J. Ramm, P.H. Mayrhofer; *Thermal Stability of Arc Evaporated Al-Cr-O-N Coatings*, to be submitted for Surface and Coatings Technology.

<u>R. Raab</u>, C.M. Koller, S. Kolozsvári, J. Ramm, P.H. Mayrhofer; *Influence of synthetic air as reactive gas on arc evaporated Al-Cr-O-N Coatings*, manuscript in final preparation.

.

Publications not included in the thesis

<u>C.M. Koller</u>, V. Dahlbauer, R. Raab, P. Polcikc, J. Ramm, P.H. Mayrhofer; *Thermal stability of arc evaporated $(Al_x,Cr_{1-x})_2O_3$ coatings*, manuscript in final preparation.

Resume

Robert Raab, MSc.

Institute of Materials Science and Technology, TU Wien,
E-Mail: robert.raab@tuwien.ac.at, Phone: +43 1 58801 30868

Personal details:

Date of Birth: ███████
Place of Birth: Vienna, Austria
Private Address: ████████████████
Citizenship: Austrian

Education:

Since 2014	**PhD-Student** at TU Wien (A), Institute of Materials Science and Technology, Chair of Materials Science
Oct. 2013	**Master of Science** at TU Wien (A), Thesis: "Weiterentwicklung eines Wanderwellen- Neutronenspinresonators für sehr kalte Neutronen"
Oct. 2010	**Bachelor of Science** at TU Wien (A), Thesis: "Guiding Of Slow Highly Charged Ions Through A Single Mesoscopic Glass Capillary"
Jun. 2005	**High school diploma**

Teaching Experience

2016-2017   **Materials testing Lab** (1.5 ECTS), lecturer

Supervised bachelor students

W. Zhou   Thermal Stability of Arc Evaporated AlCrON Coatings for High Performance Cutting Application
T. Scheu   Influence of manufacturing processes of $Al_{0.7}Cr_{0.3}$ targets on arc evaporated Al-Cr-N coatings

Supervised student co-workers

T. Glechner   metallographic
P. Kutrowatz   TEM sample preparation
A. Scheiber   chemical laboratory

Papers

1) **R. Raab**, C.M. Koller, S. Kolozsvári, J. Ramm, P.H. Mayrhofer; Influence of interface volume and geometry on structure and mechanical properties of arc evaporated Al-Cr-N/Al-Cr-O multilayer coatings, Manuscript accepted in SCT, May. 2017

2) R. Bereczky, G. Kowarik, C. Lemaignan, A. Macé, F. Ladinig, <u>R. Raab</u>, F. Aumayr, K. Tökési: "Guiding Of Slow Highly Charged Ions Through A Single Mesoscopic Glass Capillary"; American Institute of Physics conference proceedings, 1336 (2011), 119 - 122.

Oral presentations at international conferences:

1) **R. Raab**, S. Kolozsvári, J. Ramm, P.H. Mayrhofer; Thermal stability of cathodic arc evaporated oxide and oxide/nitride coatings within the system Al-Cr-N and Al-Cr-O, International Conference on Metallurgical Coatings and Thin Films, 24. - 28. April 2017, San Diego CA (USA)

2) **R. Raab**, S. Kolozsvári, R. Rachbauer, P.H. Mayrhofer; Influence of Multilayer Arrangement on Structure and Mechanical Properties of Arc Evaporated Oxide, Nitride, and Oxide/Nitride Coatings within the Systems Al-Cr-N and Al-Cr-O, International Conference on Metallurgical Coatings and Thin Films, 25. - 29. April 2016, San Diego CA (USA)

3) **R. Raab**, C. Sabitzer, S. Kolozsvári, R. Rachbauer, P.H. Mayrhofer; Multilayer Arrangement of Oxide and Nitride Coatings within the System Al-Cr-N and Al-Cr-O, Vienna young Scientists Symposium, 25. - 26. June 2015, Vienna (Austria)

Poster presentations at international conferences:

1) **R. Raab**, S. Kolozsvári, J. Ramm, P.H. Mayrhofer; Thermal stability of cathodic arc evaporated oxide and oxide/nitride coatings within the system Al-Cr-N and Al-Cr-O, International Conference on Metallurgical Coatings and Thin Films, 24. - 28. April 2017, San Diego CA (USA)

2) **R. Raab**, S. Kolozsvári, R. Rachbauer, P.H. Mayrhofer; Influence of Multilayer Arrangement on Structure and Mechanical Properties of Arc Evaporated Oxide, Nitride, and Oxide/Nitride Coatings within the Systems Al-Cr-N and Al-Cr-O, 12. – 16. Sept. 2016, Garmisch-Partenkirchen, Germany

3) **R. Raab**, C. Sabitzer, S. Kolozsvári, R. Rachbauer, P.H. Mayrhofer; Architectural design of oxide and nitride coatings within the system Al-Cr-N and Al-Cr-O, 08. – 10. April 2015, Leoben, Austria

Vienna, June 29th, 2017

Robert Raab